Probing the Hubbard Model With Single-Site Resolution

Probing the Hubbard model with single-site resolution

A DISSERTATION PRESENTED
BY
MAXWELL FREDRICK PARSONS
TO
THE DEPARTMENT OF PHYSICS

IN PARTIAL FULFILLMENT OF THE REQUIREMENTS
FOR THE DEGREE OF
DOCTOR OF PHILOSOPHY
IN THE SUBJECT OF
PHYSICS

HARVARD UNIVERSITY
CAMBRIDGE, MASSACHUSETTS
MAY 2016

Thesis advisor: Professor Markus Greiner Maxwell Fredrick Parsons

Probing the Hubbard model with single-site resolution

Abstract

Strongly-correlated electron systems generate some of the richest phenomena and most challenging theoretical problems studied in physics. One approach to understanding these systems is with ultracold fermionic atoms in optical lattices, which can provide a level of control and ways of observing strongly-correlated fermionic systems that are not accessible with conventional materials. This thesis describes the development of an experimental technique where a quantum gas of fermionic ^{6}Li atoms is prepared in a two-dimensional optical lattice and each atom can be frozen in place and imaged with single-site resolution. Combining a vacuum-compatible large numerical aperture microscope with Raman sideband cooling enables site-resolved fluorescence imaging with high fidelity. We observe several phases of the Hubbard model, including band and Mott insulators. The observed in-situ occupation distributions of atoms in the lattice are compared to theory with unprecedented detail and are used to determine the thermodynamic properties of the system. By combining site-resolved imaging with a spin-removal technique, we observe antiferromagnetic correlations in the Hubbard model with single-site resolution. We observe, for the first time in cold atom systems, beyond-nearest-neighbor magnetic correlations, which provide a direct measurement of the correlation length. We also present detailed measurements of the formation of correlations during lattice loading.

Contents

0 Introduction 4

1 The Fermi gas microscope 10
- 1.1 Imaging Systems . . . 12
- 1.2 Magnetic field control . . . 13
- 1.3 Optical traps . . . 18
- 1.4 Experimental sequence . . . 29
- 1.5 Lattice calibration . . . 32

2 Theoretical considerations for ^{6}Li in an optical lattice 38
- 2.1 Feshbach Resonances in ^{6}Li . . . 39
- 2.2 Fermions in an optical lattice interacting via contact interactions . . . 43
- 2.3 The Hubbard Model . . . 48

3 Site-resolved imaging of ^{6}Li atoms using Raman sideband cooling 56
- 3.1 Raman sideband cooling . . . 59
- 3.2 Experimental setup . . . 64
- 3.3 Broadening Effects . . . 66
- 3.4 Atom detection algorithm . . . 69
- 3.5 Imaging Fidelity . . . 74
- 3.6 Optimization of Raman imaging parameters . . . 75

4 Site-resolved imaging of a fermionic Mott insulator 81

5 Site-resolved observations of the spin-correlation function 96
- 5.1 Spin-removal technique for measuring correlations . . . 98
- 5.2 Observations of the spin-correlation function . . . 100
- 5.3 Mapping spin correlations onto charge correlations . . . 108
- 5.4 Sources of systematic error for the spin correlation measurement . . . 110
- 5.5 Comparison with numerical simulations . . . 113
- 5.6 System Calibrations . . . 117

6 Looking forward 119

Appendix A ^{6}Li Atomic Properties 125
A.1 Zeeman Shifts 125
A.2 Optical transitions 129

Appendix B Super-polished Substrate Coating Data 133

References 149

To my teachers.

Acknowledgments

First, and most importantly, I want to thank the lithium lab — Widagdo Setiawan, Kate Wooley-Brown, Florian Huber, Sebastian Blatt, Anton Mazurenko, Christie Chiu, Geoffrey Ji, and Daniel Greif — for all of their hard work and comradery. The work presented here was as much theirs as it was mine. Christie Chiu, Daniel Greif, Geoffrey Ji, and Anton Mazurenko thank you very much for your close reading of various portions of this thesis.

I thank the Doyle group circa 2006-2010 for getting me started in experimental physics. I can't imagine a better experience. In particular, I want to thank Dave Patterson, Wes Campbell, Amar Vutha and Nick Hutzler, who very patiently taught me the ropes. I also want to thank Andreas Osterwalder, Gerard Meijer and their groups for adding to that early research experience.

I thank my adviser, Markus Greiner, for providing us with the resources, technical expertise, and guidance to put this monster together. I also thank the rest of the Greiner group for being hiking buddies, people to laugh with, paper readers, technical advisers, and more, and for wholeheartedly sharing the miseries of failure and the joys of success for the last five years. You've all been a lot of fun to work with.

I thank members of the local physics community for consistently providing the atmosphere of levity and support that has made this place feel like home over the last decade and, in particular, members of the Harvard physics staff and faculty: Carol Davis, Vickie Greene, Sheila Ferguson, Jan Ragusa, Barbara Drauschke, Jean O'Connor, Joan Hamilton, Jim Macarthur, Lisa Cacciabaudo, Dave Morin, Joe Peidle, Cumrun Vafa, Howard Georgi, Vinny Manoharan, Misha Lukin, Sasha Zibrov, John Doyle, Ike Silvera, Ron Walsworth, Eugene Demler and Erel Levine. Along the same lines, I want to thank the entire CUA, with a particular shoutout to the members of the Doyle lab, everyone in the Fermi II experiment in the Zwierlein group, and everyone in the BEC V experiment in the Ketterle group.

Finally, I want to thank my friends for giving me lots of opportunities to get out of the lab. You have been invaluable for maintaining the shreds of sanity that I have left, and I'm sure you'll help grow the sanity back when all this is over.

Listing of figures

1.1 High resolution imaging system 11
1.2 Schematic of loworesolution imaging system with the objective 14
1.3 Coil setup around glass cell 14
1.4 Feshbach coil driver 15
1.5 Jump coil design 18
1.6 Layout of optical dipole traps in glass cell 19
1.7 "Red sheet" trap optical setup 21
1.8 Accordion lattice optical setup 22
1.9 Optical lattice generation and layout 23
1.10 Comparison of lattices in the z-direction 26
1.11 Sequence for evaporating in the crossed dipole trap 30
1.12 Sequence for evaporating in the accordion 33
1.13 Lattice modulation spectroscopy for calibrating the lattice depth 34
1.14 Calibration of the trap frequencies with breathing mode oscillations 36
1.15 Lattice modulation spectroscopy for calibrating the Hubbard U parameter 37

2.1 Magnetic field dependence of s-wave scattering lengths in lithium-6 41
2.2 Spectrum for a 1D lattice 46

3.1 Imaging of lithium atoms in an optical lattice with single-site resolution 57
3.2 Raman transition between two stable ground states through multiple excited states 60
3.3 Raman sideband cooling scheme for lithium-6 64
3.4 Diagram of Raman beam and trap geometries for Raman sideband cooling 68
3.5 Raman laser setup (laser table) 69
3.6 Raman laser setup (experiment table) 70
3.7 Frequency offset lock for Raman and optical pumping lasers 70
3.8 Atom detection algorithm for site-resolved images 71
3.9 Determine the Raman imaging fidelity 73

3.10 Optimization of Raman transition rate 77
3.11 Optimization of optical pumping rate 78
3.12 Optimization of Raman imaging parameters 79

4.1 Transition from metal to band insulator to Mott insulator 84
4.2 Schematic illustration of inhomogeneous Hubbard model phases 87
4.3 Fitting the Hubbard model equation of state for a single experimental shot 90
4.5 Controlling the size of a Mott insulator 93
4.6 Melting a Mott insulator 94

5.1 Experimental technique for measuring spin correlations 98
5.2 Measurement of on- and off-resonant removal of spin states. 99
5.3 Spatial maps of the spin-correlation function 101
5.4 Quantum Monte Carlo comparison and correlation legnths 103
5.5 Dynamics of spin correlations during lattice loading 105
5.6 Spin correlations for varying interaction strength 106
5.7 Measurement of spin correlation systematics due to the removal pulse 112
5.8 Measurement of spin correlation systematics due to imaging 113
5.9 Precision determination of the trap frequency and on-site interaction 118

A.1 Magnetic field dependence of energy levels in the $2S_{1/2}$ electronic manifold 127
A.2 Magnetic moments for the $2S_{1/2}$ electronic manifold 128
A.3 Nearly-closed optical transitions in the Paschen-Back regime 130
A.4 Leakage out of cycling transitions for varying magnetic field 131

B.1 Super-polished substrate reflectivity for s-polarized light 135
B.2 Super-polished substrate reflectivity for p-polarized light 136

Listing of tables

1.1 Lattice potential calibrations 25

3.1 Geometric coupling factors for Raman transitions through the D1-line 62
3.2 Geometric coupling factors for Raman transitions through the D2-line 62

5.1 List of observable two-point correlators with the blowout detection method . . . 111

A.1 Hyperfine constants for the $2S$ and $2P$ states if ^{6}Li 127
A.2 Reduced matrix elements for optical transitions in ^{6}Li 132

B.1 Coating design for the super-polished substrate 134

0

Introduction

Strongly correlated quantum many-body systems yield some of the richest and most complex phenomena in physics [1, 2]. Strong correlations readily arise when competing interactions occur at similar energy scales [3], such as in the vicinity of quantum phase transitions [4]. Systems exhibiting strong correlations cannot be described by the properties of a few weakly-interacting particles and the resulting macroscopic phenomena can often not be constructed from the fundamental interactions that govern the system [1]. As Dagotto writes [2],"...in such systems, which are not merely complicated, one expects emergence, namely the generation of properties that do not preexist in a system's constitutents." Emergent phenomena arising from strong correlations include effects, such as high-temperature superconductivity [5, 6] and colossal magneto-resistance [7], which could be profoundly important to future technology. Justifiably, a large fraction of physicists' activities are directed toward exploring

strongly-correlated quantum systems, with the bulk of this research focused on electron systems. An experimental platform that has gained traction over the last two decades as a complementary approach to conventional solid-state methods for understanding strongly-correlated quantum systems is ultracold atoms. Cold atoms provide an intermediate scale between very small systems where the effects of interactions can be well understood, and large-scale solid-state systems where interactions give rise to emergent phenomena.

The technology required to create quantum many body systems out of cold atoms has only recently been developed and continues to advance. Developments in laser cooling, magnetic and optical trapping, [8] and the invention of evaporative cooling [9, 10] in the 1980's and early 1990's led to the realization of Bose-Einstein condensation (BEC) in 1995 [11, 12]. This new ability to generate a well-isolated, controllable, bosonic many-body system led to a host of studies of phenomena including matter-wave interference, bosonic superfluidity, spinor condensates, vortices and solitons [13, 14, 15]. The need to avoid three-body collisions which lead to atom loss means that cold atom samples typically have densities of $10^{12} - 10^{15}$ cm^{-3}, are weakly interacting, and can be described in terms of mean-field theory, neglecting the effects of correlations. At these densities the average interatomic spacing is on the order of the wavelength of light. In 1998, Jaksch et al. [16] proposed the idea that the dynamics of a dilute Bose gas, loaded into an optical lattice, would be a realization of the Bose-Hubbard model. The optical lattice enhances the effect of interactions relative to the kinetic energy of the particles and this enhancement can give rise to strong correlations in the system. The ratio of the interaction energy to the kinetic energy can be tuned by varying the intensity of the light that generates the optical lattice. In this manner, a quantum phase transition from a superfluid, where kinetic energy dominates, to a Mott insulator, where strong interactions give rise to an insulating state, could be realized. This proposal, and the subsequent realization of the superfluid to Mott insulator transition by Greiner, et al. [17] in 2002 opened the door to studying strongly correlated quantum systems with ultracold atoms.

Developments with quantum gases of ultracold fermionic atoms paralleled the developments of bosonic quantum gases, but delayed by four to five years. The first degenerate Fermi gases were realized in 1999 in the Jin group at JILA [18]. Feshbach resonances, initially realized in bosonic systems [19, 20] and then in fermionic systems [21, 22], provide the ability to tune the s-wave scattering length and thus the strength and sign of interactions between atoms. In bosonic systems, the enhanced scattering length at these resonances is accompanied by enhanced three-body loss, and proved to be of limited utility. In fermionic systems, however, the Pauli exclusion principle suppresses three-body loss [23], and Feshbach resonances have provided a route to strongly-interacting systems[24]. On the repulsive side of a Feshbach resonance, fermions pair to form weakly-bound molecules [25, 26, 27], while on the attractive side they form a Bardeen-Cooper-Schrieffer (BCS) superfluid. The tunability of interactions allowed for study of the crossover between these two regimes [28, 29, 30]. Reviews of the physics explored with bulk Fermi gases can be found in [31, 32].

Just as for bosons, fermionic atoms can be loaded into optical lattices to create strong correlations. Fermionic atoms with short-range interactions loaded into the lowest band of a sufficiently deep optical lattice realize the Hubbard model [33]. The Hubbard model was developed to describe correlation effects for strongly-interacting electron systems [34] and captures the physics of interaction-driven Mott insulators and antiferromagnetism. There is strong evidence from numerics that the Hubbard model contains the ingredients necessary for high-temperature superconductivity. Numerical simulations of the two-dimensional Hubbard model using dynamical mean-field theory in the dynamical cluster approximation show the appearance of a pseudogap phase and d-wave superconductivity for repulsive interactions away from half-filling, independent of cluster size [35, 36]. Cold fermionic atoms in Hubbard-regime optical lattices could potentially be used to verify these results and explore a larger space of parameters than numerical simulations allow, but doing so will require lower temperatures than have been achieved. Previous studies exploring the Hubbard model with cold atoms have observed fermion anti-bunching in the non-interacting regime [37], Mott and band insulators [38,

39, 40], nearest-neighbor density correlations [41], inelastic doublon decay [42], and short-range antiferromagnetic correlations [43, 44, 45]. Fermionic Mott insulators in systems with more than two spin components have also been explored [46, 47] Recently, high resolution in-situ absorption imaging has also enabled a direct measurement of the equation of state of the two-dimensional Hubbard model at temperatures where spin ordering is suppressed [48].

The possibilities for exploring many-body physics with cold fermionic atoms go well beyond the Hubbard model in thermal equilibrium. The development of a system to produce a tunable geometry optical lattice [49] enabled the realization of Dirac points in the lattice band structure [50] as well as the creation of a band-structure that mimics that of graphene [51]. Using a bipartite honeycomb lattice geometry revealed a competition of states with different density order [52]. Additionally, by combining a honeycomb lattice with circular shaking, a Haldane model, where a complex tunneling parameter can give rise to topological band structure, was realized [53]. An advantage of the cold atom platform is that the low energy scales, with interaction and tunneling energies generally below 30 kHz, enable the direct observation of real-time dynamics opening the door to studies of non-equilibrium systems. At present, there have been few studies exploring out-of-equilibrium dynamics with fermions in optical lattice. Researchers have observed the real-space evolution of interacting atoms in the Hubbard regime after a quench [54, 55], and studied of the dynamics of nearest-neighbor spin correlations after a quench of the lattice geometry [45].

For optical lattice experiments, the minimum spacing between lattice sites is on the order of an optical wavelength. This affords the opportunity to image atoms in-situ with enough resolution to observe individual atoms in the lattice. This technique of quantum gas microscopy was first pioneered for large optical lattices, which relaxes imaging requirements, but also suppresses the effect of quantum tunneling within the lattice [56]. Gemelke et al. [57] used high-resolution absorption imaging to observe the formation of Mott-insulating domains for bosons trapped in an optical lattice. Site-resolved fluorescence imaging for bosonic ^{87}Rb in Hubbard-regime optical lattices

was first demonstrated in our group [58] and shortly thereafter in the Bloch group in Munich [59]. Recently, the technique was also demonstrated for bosonic Yb atoms [60]. The first studies with this technique observed the wedding-cake structure of bosonic Mott insulators with single-site resolution [61, 59]. One benefit of microscopy, which was shown clearly when the wedding-cake structure was observed for bosonic Mott insulators, is that it can take advantage of the inhomogeneity of trapped atom systems. With conventional time-of-flight imaging techniques, measurements are always averaged over an inhomogeneous sample. By performing high-resolution, in-situ imaging, one instead obtains the measured observable for a variety of chemical potentials (assuming a system in thermal equilibrium and the validity of a local density approximation). A further advantage of site-resolved imaging is that it provides direct access to density and spin correlations [62].

In the past six years, a wide variety of experiments in the bosonic quantum gas microscopes have been performed. Simon et al. [63] simulated the adiabatic preparation of an antiferromagnetic state, achieving spin-interactions with a site-occupation to pseudo-spin mapping. Bakr et al. [64] observed the orbital excitation blockade and used it to demonstrate algorithmic cooling. Cheneau et al. [65] observed the light-cone like spreading of correlated doublon-hole pairs after a lattice quench. The Higgs amplitude mode was observed in the superfluid to Mott insulator transition [66]. By employing site-resolved control over the hyperfine state of atoms, the Bloch group was able to explore the dynamics of spin impurities [67], observing magnon bound states [68] and other spin-transport phenomena [69, 70]. Using Rydberg atoms, a number of experiments were performed which studied crystallization effects due to long-range interactions [71, 72, 73]. Recently, by projecting a disordered potential and observing the expansion dynamics after removing part of the cloud Choi et al. [74] were able to observe many-body localization. In our group, the development of calibrated digital mirror devices for projecting precise arbitrary potentials [75] enabled the high-fidelity preparation of and precise dynamical control over unity-filled few-particle systems. This led first to studies of strongly-correlated quantum walks [76], and later to a direct measurement of entanglement

entropy using two identical bosonic systems [77] and to studies of the relationship between thermalization and entanglement [78].

As with other major developments in cold atoms, site-resolved imaging was demonstrated for fermionic atoms about five years after it was demonstrated for the bosons. The first reports of site-resolved imaging of fermions, for ^{40}K [79, 80] and ^{6}Li [81] came within weeks of one another. Two other demonstrations, for a thermal gas of ^{40}K[82] and a band insulator of ^{6}Li [83] came within a few months. This thesis reports the development of site-resolved imaging of fermionic ^{6}Li and the early fruits of that technique. It is organized as follows:

- Chapter 1 provides details of the experiment apparatus and the procedure used to create a gas of cold fermions trapped in an optical lattice. In this chapter detailed information is omitted when it has been provided in Florian Huber's thesis [84].

- Chapter 2 provides a brief summary of the theory required to describe our experiments with interacting fermions in a Hubbard-regime optical lattice.

- Chapter 3 provides a description of our site-resolved imaging scheme and optical setup. It starts with a general description of Raman sideband cooling, then describes our experimental implementation of site-resolved imaging, and finally describes optimization of the imaging parameters and how the imaging quality varies with different imaging parameters. Much of the information in this chapter has been reported in reference [81].

- Chapter 4 describes our observations of band insulators and Mott insulators using site-resolved imaging, following closely the material published in reference [85].

- Chapter 5 describes our observations of antiferromagnetic correlations in a compressible regime of the Hubbard model where the kinetic and interaction energies are comparable. The material in this chapter follows closely a manuscript which is currently in preparation.

1

The Fermi gas microscope

In this section I describe the experimental setup. Some of the setup has been covered already in the theses of Widagdo Setiawan [86] and Florian Huber [84]. The experimental sequence and components of the apparatus through the transport of the atoms into the glass cell have been covered extensively in those theses and have not changed. I first document components of the apparatus that have been added or modified since previous theses. I then describe the experimental sequence and calibration procedures.

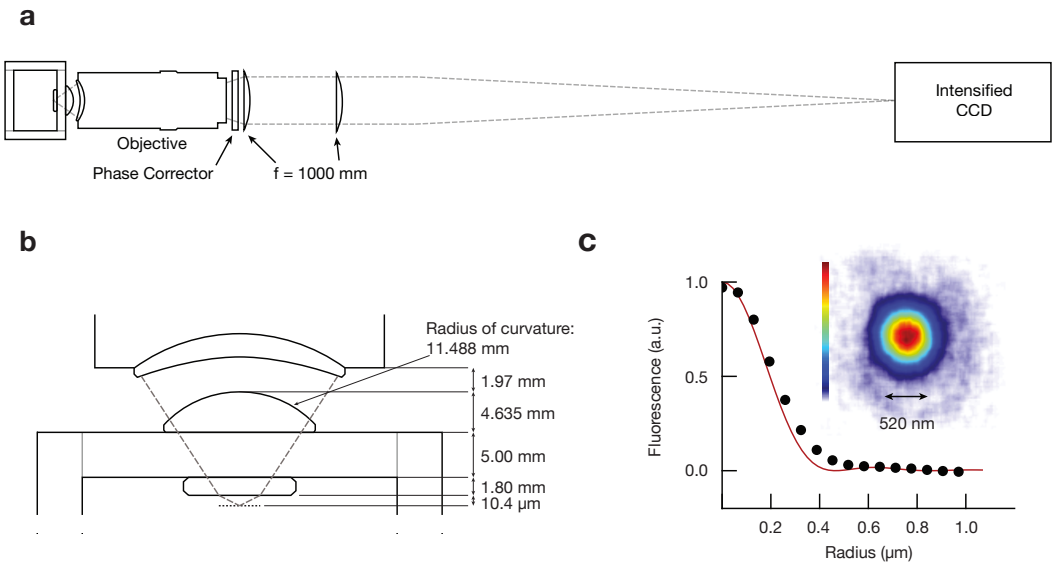

Figure 1.1: Panels a and b show schematic diagrams of our high-resolution imaging setup (not to scale). Panel c shows the point spread function (PSF) of the imaging system, obtained by superimposing and averaging super-sampled images of single atoms in a sparsely-loaded lattice. The red curve is the expected Airy-disk profile for our numerical-aperture, and agrees well with the measured profile. The airy-disk profile does not take into account effects of polarization which play a role at large numerical apertures and would broaden the expected PSF. A Gaussian fit to the PSF yields a full width at half maximum of $520\,\mathrm{nm}$, compared to our lattice spacing of $569\,\mathrm{nm}$.

1.1 Imaging Systems

1.1.1 High-resolution imaging system

To detect single atoms spaced by only 560 nm using fluorescence imaging, we require the high-resolution and large photon collection efficiency afforded by a high numerical aperture (NA) imaging system. By combining a long working distance microscope objective (Optem 20x, NA = 0.6) and a hemispherical lens we have constructed a diffraction-limited imaging system with an NA of 0.87 (figure 1.1). The atoms are trapped 10 μm below the flat surface of the hemisphere, which is comprised of a lens, the glass cell wall, and a superpolished substrate that is optically contacted to the interior of the glass cell. Each of these components is made from fused silica in order to ensure that the thermal expansion coefficients are matched for optical contacting. The substrate is anti-reflection coated for 670 nm - 790 nm to allow imaging light and projected dipole traps to pass through. The same coating is highly reflective ($> 99.96\%$) at 1064 nm, our lattice wavelength, as we use reflection off of the substrate to generate the optical lattices (section 1.3.3). See appendix B for the coating design and data.

The flat bottom surface of the hemisphere deflects rays emitted from the atoms toward the optical axis of the imaging system and therefore enhances the numerical aperture of the commercial objective by a factor of the index of refraction of the hemisphere (figure 1.1b). Rays emanating from the atoms are normal to the spherical top surface of the hemisphere, and so no refraction occurs at this surface. The cost of this NA enhancement is spherical aberration generated by a large mismatch between the wavefront curvature of the light generated by the atoms and the flat curvature of the bottom surface of the hemisphere. We have compensated for this spherical aberration in two ways. First, we found from ray tracing simulations that by operating the objective away from infinite conjugation we could use the spherical aberration generated by the objective to compensate for spherical aberration generated by the hemisphere. To restore infinite conjugation, for convenience,

we have attached a lens with focal length 1 m to the back of the objective. Additionally, we have fine-tuned the aberration compensation by attaching a phase plate to the back of the objective. The phase plate provides a phase shift with an R^4 profile and a 0.5-wave shift at the edge of the plate (Edmund Optics 66-751). The choice of phase plate was optimized on the point spread function of the imaging system, obtained by superimposing and averaging isolated atoms in a sparsely-loaded lattice (figure 1.1c). An overview of the imaging setup is shown in figure 1.1a. The magnification of the high-resolution imaging system is approximately 160.

To achieve diffraction-limited performance it is critical that the optical axes of the objective and hemisphere are well-aligned. The alignment was done with a white-light Fizeau interferometer. After alignment, the objective was glued to a ceramic mount that is attached to the glass cell and also holds the retro-reflectors for our lattice beams. Mechanically referencing the objective to the optical lattice makes the imaging system extremely stable. We observe that our site-resolved images typically drift by less than 10% of a lattice site over hundreds of experimental runs. The interferometric alignment and mounting of the objective are described in detail in Florian Huber's thesis [84].

1.1.2 Low-resolution imaging system

For alignment of optical traps, we can perform absorption imaging of the atoms with a low-resolution imaging system that has a magnification of 4.3, shown schematically in 1.2. We use this primarily to align the dimple trap, transport trap, and red sheet with respect to one another.

1.2 Magnetic field control

1.2.1 Feshbach coil

The Feshbach coils are used for providing a bias field to control the scattering length between spin-mixtures of ^{6}Li, as well as to provide a magnetic field gradient along the z-axis for forced evaporation. The

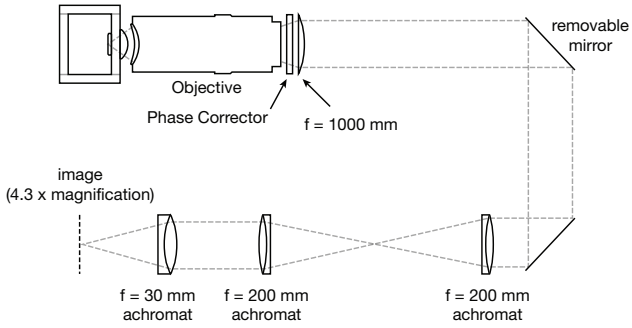

Figure 1.2: With the insertion of a mirror on a mechanically-referenced mount the atoms can be imaged in low-resolution through the objective, with a magnification of 4.3. This imaging system is schematically described above.

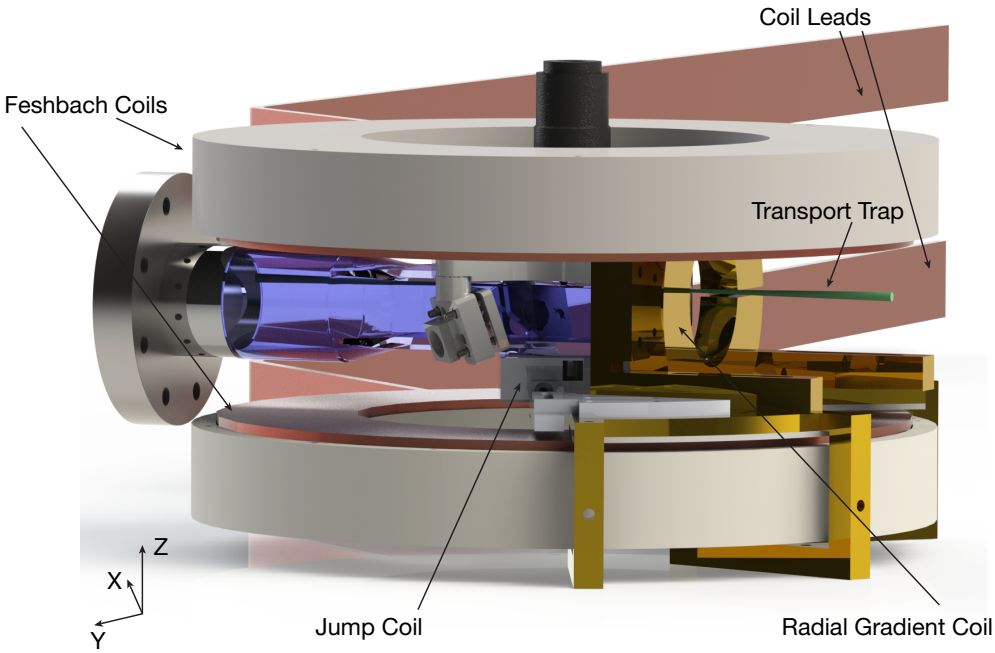

Figure 1.3: A 3D CAD rendering of the science chamber showing the layout of the magnetic field coils, as well as the transport trap for reference.

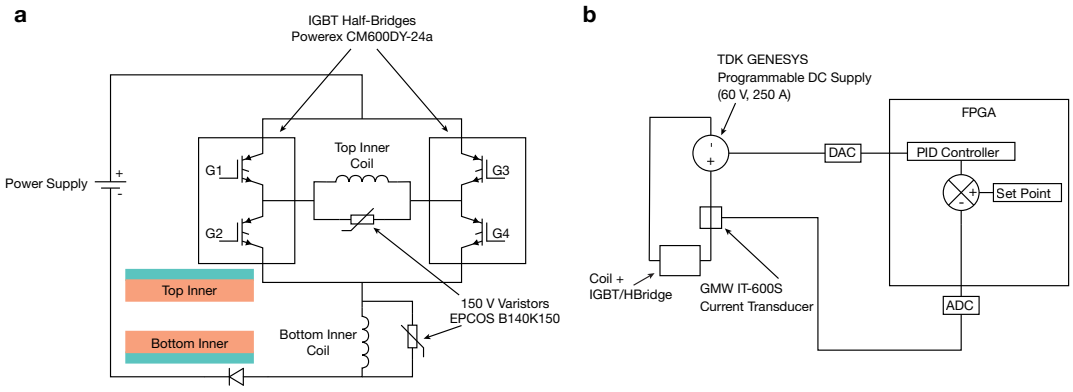

Figure 1.4: An H-bridge circuit using IGBTs allows us to switch the inner sections of the Feshbach coils between Helmholtz and anti-Helmholtz configurations (panel a). The colored inset shows schematically the coil construction as it relates to the driver schematic, with the turquoise outer sections corresponding to the outer sections of the Feshbach coils as described in the text. Details about the Feshbach coil construction are provided in [86]. The setup used to generate and stabilize the current used to drive the Feshbach coils and the radial gradient coil is shown in panel b.

construction of the coils has been described in detail in Widagdo Setiawan's thesis [86]. Here I provide up to date information about the coil driver and the fields generated at the atoms.

As depicted in the colored inset of figure 1.4a, the Feshbach coil has four sections, which I'll refer to as top-outer, top-inner, bottom-outer, and bottom-inner. The top-outer and bottom-outer sections are connected in series and driven by the power supply and current feedback setup shown in figure 1.4b, with an additional insulator-gate bipolar transistor (IGBT) to disconnect them from the power supply. The driver is designed to be able to handle currents up to 500 A, but we have not yet found the need to go beyond the 250 A available with the current power supply configuration. Together the coils create a bias field in the $-\hat{z}$ direction. The bottom-inner and top-inner sections are also connected in series and are controlled by another identical power supply and current feedback setup as the outer sections. An H-bridge circuit, shown in figure 1.4a, allows the direction of current through the bottom inner section to be flipped, switching the inner sections between near-Helmholtz and near-anti-Helmholtz configurations. With the inner sections in Helmholtz configuration the

uniform bias fields generated by the inner and outer sections together combine and provide access to the Feshbach resonance at 834 G (section 2.1). With the inner sections in anti-Helmholtz configuration they provide a gradient which can be used to aid in forced optical evaporation (section 1.4) while the outer coils provide a bias field to control the scattering cross section during evaporation.

The atoms sit 18.5 mm above the geometric center of the coils, and are displaced in the x-y plane by 2 mm. The outer coils produce a bias field of 1.2 G/A primarily in the $-\hat{z}$ direction, although there is a small component ($< 5\%$) in the x-y plane due to the displacement of the atoms from the radial center of the coils. Due to displacement of the atoms from the vertical center of the coils, the outer coils also produce a small gradient of 9 mG/cm/A in the $-\hat{z}$ direction. With the inner coils in anti-Helmholtz configuration they produce a magnetic field gradient primarily in the $-\hat{z}$ direction of 0.25 G/cm/A and a bias field in the same direction of 0.46 G/cm/A. In Helmholtz configuration the inner coils produce a bias field of 2.9 G/A, again in the same direction, with a gradient of 18 mG/cm/A in the $+\hat{z}$ direction due, again to the displacement of the atoms from the geometric center of the coil.

1.2.2 Radial gradient coil

The radial gradient coil is used to generate a gradient for forced evaporation from the accordion after compression, just before loading the lattice (section 1.4).

The coil is constructed from 2.2 mm x 4.1 mm kapton-coated rectangular copper wire. It is wound from the inside out in two pancakes with 16 windings each, in a similar manner as the Feshbach coils. The coil is housed in a water-cooled brass mount, with its axis of cylindrical symmetry along $\hat{x} + \hat{y}$. The coil is mounted such that the atoms are on this symmetry axis, approximately 62 mm from the nearest face of the coil. The coil is driven by an identical power supply and current stabilization system as the Feshbach coils, shown in figure 1.4b, with an additional IGBT for disconnecting the coil from the power supply. The power supply can deliver up to 250 A of current, but the coil

and water-cooling were not designed to operate at this current in steady state, as we only require the coil to be pulsed on for approximately 1 s every experimental cycle ($\sim$ 20 s). A thermistor, connected to the global experiment interlock, has been mounted to the coil and will open the IGBT, severing the connection to the power supply, in the event that the coil temperature exceeds 50° C.

This coil creates a gradient of approximately 0.32 G/cm/A in the $-(\hat{x}+\hat{y})$ direction, as well as a bias field of 1.1 G/A in the same direction. We use the coil in conjunction with the outer section of the Feshbach coils to generate a gradient which pulls atoms radially out of the compressed accordion at a bias field controlled by the Feshbach coils (section 1.4). The bias field from the Feshbach coils suppresses the gradient, and so for a certain gradient requirement there is a maximum achievable bias field. When evaporating from the accordion lattice and dimple with the smallest gradient necessary for completely spilling the accordion trap ($\sim$ 67 G/cm), the maximum achievable bias field is approximately 240 G.

1.2.3 Jump coil

The jump coil (figure 1.5) is used to quickly ramp up through the narrow s-wave Feshbach resonance at 543 G[87] to avoid heating (section 2.1). The jump coil consists of 14 windings of 1.7 mm diameter kapton-coated copper wire with an inner diameter of 40 mm, as shown in figure 1.5b. It has been potted with Stycast 2850 epoxy into an ULTEM™ mount, which has been mounted approximately 1 mm beneath the glass cell with the atoms 31 mm away along the coil's axis of symmetry.

Because the coil has a relatively small inductance (a few μH) it can be used to create a short magnetic field pulse of $\sim$ 10 G at the atoms with a rise time of approximately 3 μs. We accomplish this by discharging a 150 μF capacitor at 100 V into the coil. The capacitor is connected to ground via a bleed resistor which discharges it completely in 3 ms to ensure that the coil, which is not thermally designed for continuous operation, does not overheat while giving the slow-ramping Feshbach coils enough time to catch up so that the atoms remain at a bias field above the narrow Feshbach

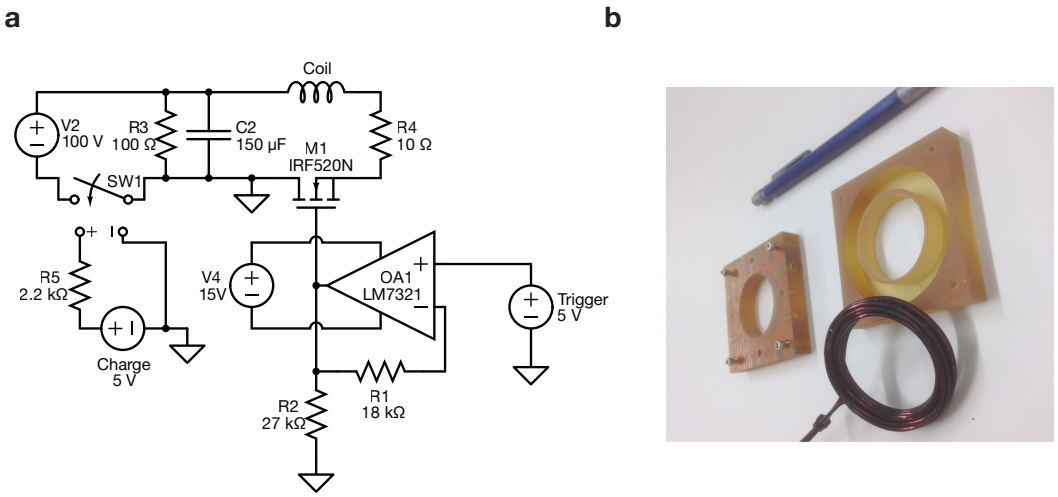

Figure 1.5: The jump coil can generate field pulses of $\sim$ 10 G with a rise time of 3 μs and a decay time of 3 ms. It is driven by discharging a 150 μF capacitor at 100 V with the circuit shown in panel a. The "Charge" and "Trigger" TTLs which charge and discharge the capacitor are generated by the experiment control system. A photograph of the coil and mount before assembly is shown in panel b.

resonance. The driver circuit for the jump coil is shown in 1.5a.

1.3 Optical traps

Our experiment relies heavily on optical dipole traps, which use light that is far-detuned from an atomic resonance to confine atoms [88]. With the exception of the MOT, and the use of magnetic field gradients to aid in forced evaporation, every trap in the experiment is an optical dipole trap. Optical dipole traps offer several advantages over magnetic traps. An optical dipole trap can be used to trap ground state atoms at rest, while a trap using any combination of static magnetic, electric or gravitational fields cannot [89]. Trapping atoms in their hyperfine ground state avoids spin-changing collisions which lead to atom loss and heating. Optical traps can be operated at arbitrary magnetic bias fields, providing the freedom to take advantage of magnetically-tunable Feshbach resonances [23]. Optical dipole traps offer micron-scale spatial resolution and therefore

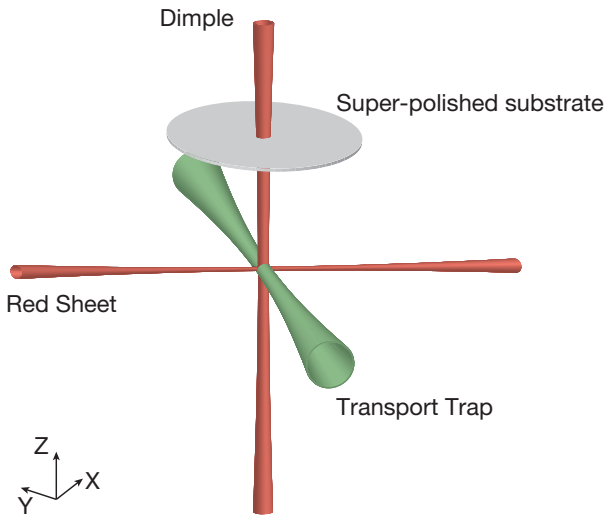

Figure 1.6: A schematic of the optical dipole traps used in the experiment.

larger trap frequencies than are typically available from magnetic traps, as well as the ability to tailor atomic potentials creating a wide variety of trap geometries including box traps [90], ring traps [91], mesoscopic channels [92], and quantum point contacts [93]. The large trap frequencies afforded by our optical dipole traps combined with an atomic sample that is stable against three-body loss allows us to tightly confine the atoms during forced evaporation, achieve high densities and elastic collision rates on the order of 10^3 s^{-1}, and create a quantum degenerate fermi gas in approximately 13 s with just 6 s of evaporation.

1.3.1 Optical Dipole Traps

The optical dipole traps used in the experiment are described in this section and shown schematically in figure 1.6.

Transport Trap

The transport trap collects atoms from the MOT and transports them to the science chamber. The light for the trap is generated from a 300 W, 1070 nm, temporally multimode but spatially single mode IPG Photonics YLR-300-LP-WC fiber laser focused to a waist of 54 μm. The maximum trap depth achievable is 3.9 mK. To perform forced optical evaporation we require stabilization of the laser power from 300 W down to 100 mW. We use a combination of current modulation and a variable waveplate attenuator to control the power over this large dynamic range. The intensity is servoed via an FPGA-based control loop with loop-gains that vary in real time depending on the set point. The setup is described in detail in the thesis of Florian Huber [84]. The beam propagates along $\hat{k}_{\mathrm{tr}} = (-0.71, -0.71, 0)$. The last mirror before the chamber is mounted to a mechanically amplified piezoelectric mount (Piezosystem Jena MICI 200) which allows us to control the z-position of the trap in the glass cell with a range of approximately 20 mm. This piezo allows us to initially transport the atoms into the vertical center of the glass cell, avoiding clipping, and then to move the atoms upward until they are approximately 100 μm beneath the super-polished substrate.

Dimple

The dimple trap is used to perform forced optical evaporation as well as to provide harmonic confinement in the x-y plane when atoms are compressed in the accordion and the physics lattice. The light for the trap is generated from an incoherent 780 nm source which uses a super-luminescent diode to seed a tapered amplifier [84], providing up to 400 mW of optical power at the atoms. The beam passes through the high-NA objective and is focused to a gaussian waist of appoximately 30 μm, propagating along $-\hat{z}$. The maximum trap depth is 40 μK, with a corresponding radial trap frequency of 2.5 kHz.

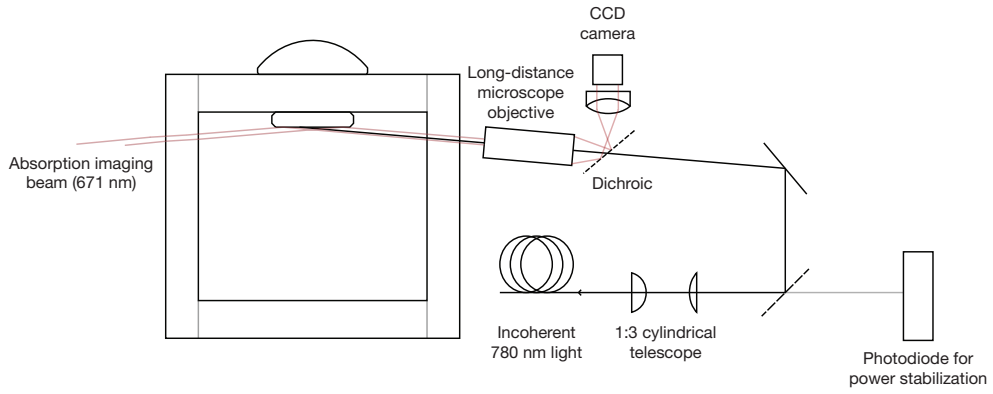

Figure 1.7: A schematic of the optical setup used to generate the red sheet trap. The objective used to focus the red sheet onto the atoms doubles as an imaging objective that allows us to resolve individual accordion pancakes.

Red Sheet

The red sheet is used to perform optical evaporation and to compress the atoms along the z-direction before loading the accordion, to facilitate loading a single plane. The light is derived from the same source as the dimple trap, providing up to 300 mW at the atoms. The optical setup for creating the red-sheet is shown in figure 1.7. The trap is designed to have a 1:3 aspect ratio, with tighter confinement in the z-direction. A cylindrical telescope blows the beam up by a factor of 3 in the z-direction before it is focused onto the atoms using a commercial K2 DistaMax CF3 long working distance microscope objective from Infinity Photo Optical. The waists of the beam at the atoms are approximately 10 μm in the z-direction and 30 μm in the x-y plane, yielding a maximum trap depth of 90 μK.

1.3.2 Accordion Lattice

We use an optical accordion lattice to transport the atoms into the image plane of the microscope before they are loaded into the optical lattice described in the next section. A 1064 nm laser beam, generated from the same source as the optical lattice (section 1.3.3), is focused to a 200 μm waist and

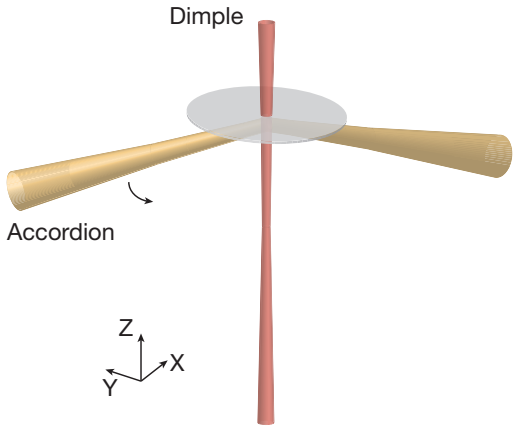

Figure 1.8: A schematic showing the propagation of the beam used to generate the accordion lattice. We can dynamically tune the angle of incidence of this beam on the substrate to control the accordion spacing. See [84] for details.)

reflected off of the super-polished substrate at an angle of incidence (AOI) that can be varied from 88.2° to 70°. This results in a lattice in the z-direction with a spacing that can be tuned from 17 μm to 1.6 μm. The propagation of the accordion beam is shown schematically in figure 1.8. As a result of the non-zero AOI, the accordion provides weaker harmonic confinement in the propagation direction than the orthogonal direction in the x-y plane. Over the full range of AOIs the aspect ratio of the trap varies from $835 : 26.2 : 1$ at 88.2° to $835 : 286 : 1$ at 70°. We dynamically tune the AOI by imaging the surface of a galvanometer-mounted mirror onto the atoms. We correct for small displacements of the beam by tilting an anti-reflection coated glass plate mounted to a second galvanometer. The details of this optical setup are described in Florian Huber's thesis [84].

1.3.3 Optical lattice

The design of our high-resolution imaging system (section 1.1.1) requires the atoms to be trapped approximately 10 μm from the surface of the super-polished substrate. With the atoms so close to the substrate surface, the lattice cannot simply be generated by retro-reflecting a laser beam in any

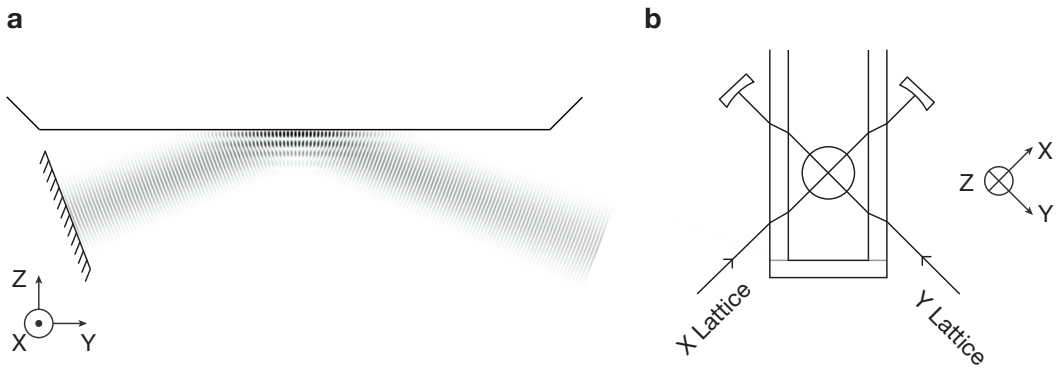

Figure 1.9: We generate our optical lattices by first reflecting a 1064 nm laser beam off of the super-polished substrate and then retro-reflecting the beam, resulting in a two-dimensional standing wave pattern as shown in panel a. For clarity of illustration, the wavelength of the lattice has been scaled up by a factor of 20 relative to the beam waist and the retro-reflector has been misplaced. We use two non-interfering, orthogonal, retro-reflected beams to generate a three-dimensional lattice as shown in panel b.

direction other than the one normal to the surface due to clipping. One possible solution, employed in the ^{87}Rb microscope in our lab is to project the lattice beams through the microscope, imaging a phase hologram onto the atoms [94]. The projection approach affords the flexibility of creating different lattice geometries by replacing the holographic mask. Another benefit is that the mask can be mechanically referenced to the microscope objective, making mechanical drifts between the lattice potential and high-resolution imaging system common mode. In practice, the beam incident on the holographic mask is quite large ($\sim$1 cm), and as a result the system is especially susceptible to disorder created by dust particles and imperfections in optical surfaces. This disorder can be mitigated by using temporally incoherent light and spatial filtering in the Fourier plane [95]. An additional constraint of the projection approach is the amount of optical power that can be sent through the objective. Anticipating the need to use up to 30 W of optical power per lattice in order to achieve the lattice depths necessary for Raman sideband imaging (Chapter 3), we opted for a different approach.

Radial lattices

The setup used to generate our optical lattice potential is shown schematically in figure 1.9. A single-mode gaussian laser beam at 1064 nm reflects off of the super-polished substrate with an angle-of-incidence (AOI) of $69.0(7)^\circ$. The substrate coating is highly-reflective at the lattice wavelength (appendix B) and so the reflection creates a standing wave in the z-direction with unity contrast. The beam is subsequently retro-reflected to provide an additional standing wave in the y-direction (x-direction). The lattice spacings along the x-direction (y-direction) and z-direction are 570 nm and $1.48\ \mu$m, respectively. Because the beam is recycled in the additional reflection off of the substrate, a single beam gives a factor of four larger lattice depth for a given beam waist and power compared to the situation when the beam is simply retro-reflected. This additional depth is critical for achieving the on-site trap frequencies that are necessary for Raman sideband cooling (Chapter 3). Atoms are trapped in the antinodes of the standing wave, as the light is red-detuned from all ground state transitions. With up to 15 W of laser power per lattice beam at the atoms and gaussian beam waists of approximately 90 μm, we measure on-site trap frequencies of up to 1.4 MHz, corresponding to lattice depths of 900 μK in each of the two radial lattice directions.

We model the potentials, $V_x(\boldsymbol{r})$ and $V_y(\boldsymbol{r})$, for the X and Y lattices respectively, as a $\cos^2$ potential with oscillations along the direction of propagation, with additional harmonic confinement along x, y, and z. Because the atoms only occupy a single layer of the lattice formed in the z-direction, we approximate the potential well from that lattice as a harmonic oscillator. We can also add additional harmonic confinement in the x-y plane with the addition of the dimple beam described in section 1.3.1, whose potential, $V_d(\boldsymbol{r})$, we model as a simple cylindrically symmetric harmonic trap in the x-y plane with trap frequency ω_d.

$$V_x(\boldsymbol{r}) = V_{0,x}\cos^2(\pi x/a_x) + \frac{1}{2}m(\omega_{/\!/,x}^2 x^2 + \omega_{\perp,x}^2 y^2 + \omega_{z,x}^2 z^2) \tag{1.1}$$

Parameter	Value
θ_x	$69.0(7)^\circ$
θ_y	$69.0(7)^\circ$
α_x	$1090(16)\ \mathrm{Hz}/\sqrt{\mathrm{W}}$
α_y	$810(22)\ \mathrm{Hz}/\sqrt{\mathrm{W}}$
α_d	$3920\ \mathrm{Hz}/\sqrt{\mathrm{W}}$
γ_x	$1.46(5)\ \mathrm{MHz}/\mathrm{W}$
γ_y	$1.14(2)\ \mathrm{MHz}/\mathrm{W}$

Table 1.1: Sample calibration values for the potential generated by our lattice beams, described by equation 1.4. The lattice angles are measured by photographically determining the positions of the beams on the in-coupling mirror and referencing these positions to center of the hemisphere using a CAD model. The α_i are determined by exciting observing breathing mode oscillations in 1D tubes of a non-interacting gas loaded into a single lattice beam as described in section 1.5.2. The γ_i are determined by comparing lattice modulation spectroscopy to a band structure calculation as described in section 1.5.1.

$$V_y(\boldsymbol{r}) = V_{0,y}\cos^2(\pi y/a_y) + \frac{1}{2}m(\omega_{/\!/,y}^2 y^2 + \omega_{\perp,y}^2 x^2 + \omega_{z,y}^2 z^2) \tag{1.2}$$

$$V_d(\boldsymbol{r}) = \frac{1}{2}m\omega_d^2(x^2+y^2) \tag{1.3}$$

Here $V_{0,i}$ is the lattice depth, $a_i = \lambda_{lat}/(2\sin(\theta_i))$ is the lattice spacing, where $\lambda_{lat} = 1064$ nm is the wavelength of light used to generate the lattice, θ_i is the AOI of the lattice beam on the substrate, and $\boldsymbol{r} = (x, y, z)$. The trap frequency in the z-direction is $\omega_{z,i}$. The trap frequencies, $\omega_{/\!/,i}$ and $\omega_{\perp,i}$, parallel and perpendicular to the direction of the lattice beam propagation, can be related to one another according to $\omega_{/\!/,i} = \omega_{\perp,i}\cos(\theta_i)$. We can measure $\omega_{z,i}$ directly using lattice modulation spectroscopy. $V_{0,i}$ can be determined by comparing the results of lattice modulation spectroscopy with a band structure calculation. The quantities $\omega_{\perp,i}$ and ω_d can be measured by exciting breathing mode oscillations in a non-interacting gas (section 1.5.2). The full lattice potential is then given by

$$V_{\text{lat}}(\boldsymbol{r}) = V_{0,x}\cos^2(\pi x/a_x) + V_{0,y}\cos^2(\pi y/a_y) + \frac{1}{2}m\omega_x^2 x^2 + \frac{1}{2}m\omega_y^2 y^2 + \frac{1}{2}m\omega_z^2 z^2. \tag{1.4}$$

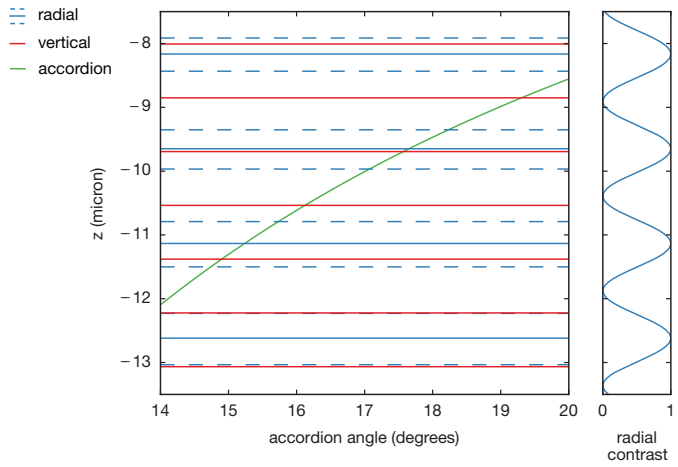

Figure 1.10: The positions of potential minima along the z-direction for the X-Y Lattice (blue), Z Lattice (red), and the position of the fifth minimum of the accordion lattice (green) as a function of angle. The dotted blue lines denote uncertainty in the X-Y lattice position due to uncertainty in the AOI of the beams used to generate those lattices.

The trap frequencies can be written solely in terms of parameters that can be directly measured:

$$\begin{aligned} \omega_x &= \sqrt{\omega_{\perp,x}^2 \cos^2(\theta_x) + \omega_{\perp,y}^2 + \omega_d^2} \\ \omega_y &= \sqrt{\omega_{\perp,y}^2 \cos^2(\theta_y) + \omega_{\perp,x}^2 + \omega_d^2} \\ \omega_z &= \sqrt{\omega_{z,x}^2 + \omega_{z,y}^2}. \end{aligned} \tag{1.5}$$

All of the trap frequencies scale as the square root of power, while the lattice depths scale linearly with power. We can therefore write, $\omega_i = \alpha_i \sqrt{P_i}$ and $V_{0,i} = \gamma_i h P_i$, where h is Planck's constant and α_i and γ_i are measured calibration parameters. All measured parameters needed to determine $V_{\text{lat}}(\boldsymbol{r})$ are listed in table 1.1.

Composite vertical lattice

For Raman sideband cooling we need to be able to generate a lattice with on-site trap frequencies of $\sim$1.2 MHz in every direction. With the X and Y lattices described in the previous section, the maximum on-site trap frequency, ω_z, in the z-direction that can be generated is approximately 700 kHz owing to the larger lattice spacing in the z-direction compared to the radial directions. To reach higher trap frequencies, we create an additional lattice in the z-direction by reflecting a 1064 nm beam with a 40 μm waist off of the substrate at an AOI of $5.86°$, resulting in a lattice along the z-direction with a spacing of 534 nm. This beam is generated in the same manner as the X and Y lattice beams. We do not use this lattice for Hubbard physics, but ramp it on only for performing single-site imaging, as described in section 3.2.1.

Because the spacing of the additional Z lattice is not commensurate with the spacing of the X and Y lattices the positions of the potential minima (intensity maxima) for the Z-lattice do not necessarily line up with the positions of the potential minima for the X-Y lattice. As the imaging lattice is ramped up, the position of the atoms will shift in the z-direction from wherever they were trapped in the X-Y lattice, as determined by the final angle of the accordion after compression, to the nearest potential minimum of the Z lattice (modulo small shifts due to gradients from the X-Y lattice). If this position is not near to the potential minimum of the X-Y lattice in the z-direction, the contrast of the lattices (and on-site trap frequencies) along x and y will be diminished. This is illustrated in figure 1.10. In that figure, the optimal accordion angle at the end of compression would be roughly $17.7°$. In practice, we have optimized the final accordion angle by loading atoms into different pancakes (varying the accordion angle) and finding the pancake where we can obtain sufficient on-site trap frequencies to perform Raman imaging. We have found the optimal accordion angle to differ from the prediction of figure 1.10, due partially to uncertainty in the angles of the X and Y lattice beams and partially to unknown angle-dependent phase shifts from the super-polished

substrate coating. The optimal angle can also shift if we realign the X or Y lattices (to replace a fiber amplifier, for example), as the AOI of the lattice beams change.

Lattice light source

The light used to generate each of the lattice beams, including the accordion and vertical lattices, is generated from a Nufern NuAmp 50 W single mode fiber amplifier seeded with 140 mW of 1064 nm light from an Innolight (now Coherent) Mephisto 1 W laser. The Nufern amplifiers have been modified by replacing an internal pump diode power supply to better preserve the low-noise performance of the Innolight Mephisto. The details of this modification can be found in Florian Huber's thesis [84]. We require stabilization of the lattice powers over a large dynamic range from $\sim$10 mW for loading a Hubbard-regime optical lattice to $\sim$20 W for performing Raman sideband cooling to image individual atoms. This dynamic range is covered using two different intensity servos which hand over at approximately 1 W. We use a galvanometer-mounted z-cut birefringent quartz plate (Berek compensator), which acts as a variable waveplate, in combination with a polarizer as a high dynamic range attenuator. For lattice powers below the servo hand over, the variable waveplate attenuates the beam to a power of approximately 1 W and the power is actuated with a Crystal Technology AOMO 3080-197 80 MHz acousto-optical modulator. We use analog feedback on the rf amplitude that drives the AOM injected with an rf mixer to servo the power. At powers above the handover, the AOM is railed and the power is actuated in closed loop with the variable waveplate. Further details about the lattice servo setup and low-noise performance can be found in [96].

1.4 Experimental sequence

The experimental sequence up through the transport of atoms to the glass cell is described in detail in Florian Huber's thesis [84]. Since the writing of that thesis, we have substantially modified the evaporation steps we take in the glass cell to produce a degenerate Fermi gas. The site-resolved imaging technique, described in detail in Chapter 3, has also been modified and improved. For completeness, I overview the entire sequence, but go into detail only for those portions which have been modified.

An atomic beam of ^{6}Li is produced from an oven, based on the design in [97], that is heated to 380°C. The beam travels through a Zeeman slower and is decelerated into the center of an octogonal stainless steel vacuum chamber where approximately 10^8 atoms, in a mixture of the two lowest hyperfine states ($|1\rangle$ and $|2\rangle$) are loaded into a magneto-optical trap, where they are cooled to approximately 500 μK. From there, atoms are loaded into an optical dipole trap that will be used for transport to the glass cell. This transport trap, with a maximum depth of approximately 3 mK, is described in section 1.3.1. As described in [84], the depth of the dipole trap is lowered to approximately 80 μK, evaporatively cooling the atoms. By moving the focus of the dipole trap, using a lens mounted to an air-bearing stage (AEROTECH ABL10100) and a piezo-actuated mirror, the atoms are then transported into the glass cell, approximately 100 μm beneath a superpolished substrate on the optical axis of the high-NA imaging system described in section 1.1.1. We have found that the atoms at this stage may be partially polarized. In order to ensure that there is an equal mixture of atoms in $|1\rangle$ and $|2\rangle$ a 300 ms long microwave pulse resonantly drives the transition between $|1\rangle$ and $|2\rangle$ in a magnetic bias field of 100 G. The duration of this microwave pulse was experimentally optimized to produce an incoherent mixture of $|1\rangle$ and $|2\rangle$, with the decoherence generated by the motion of the atoms through magnetic field inhomogeneities.

At this point the atoms are loaded into the crossed dipole trap described in section 1.3.1 and

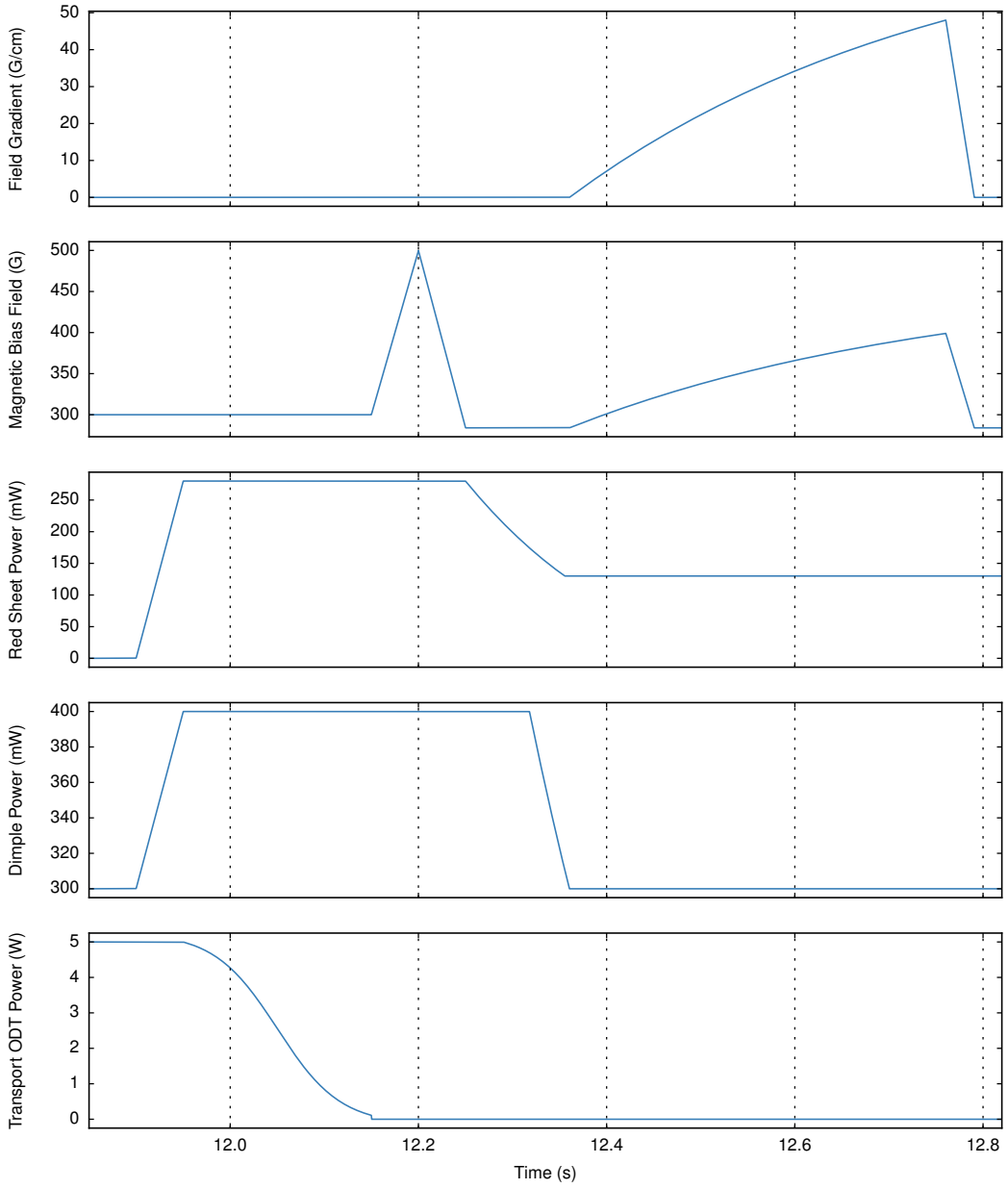

Figure 1.11: Before loading the accordion lattice, the atoms are evaporatively cooled by using a magnetic field gradient in the $\hat{z}$ direction to reduce the depth of the crossed dipole trap.

shown in figure 1.6. The experimental sequence for loading and evaporating in the crossed dipole trap is shown in figure 1.11. The crossed dipole trap, aligned with the transport trap, is ramped to a depth of approximately 130 μK. The transport trap is subsequently ramped off. The dimple and red sheet powers are then ramped exponentially over 100 ms until the trap reaches a depth of approximately 70 μK, evaporatively cooling the atoms. By using the inner Feshbach coils in anti-Helmholtz configuration, as described in section 1.2, a magnetic gradient in the z-direction can be generated to spill the atoms out of the trap. At the same time, a magnetic bias field of 300 to 400 G is maintained with the outer Feshbach coils to ensure that the scattering length between $|1\rangle$ and $|2\rangle$ is sufficient to allow efficient evaporation, as well as to ensure that the magnetic moments of these two states are similar (see figure A.2). The magnetic gradient is ramped up exponentially in approximately 400 ms. Further evaporation with a gradient ensures that hotter atoms leave the dipole trap, rather than collecting in the shallow wings away from the intersection of the two trapping beams. After evaporation, the magnetic gradient is ramped off and the bias field is reduced to 286 G. In the initial optimization of this evaporation sequence, we found that by evaporating to a trap depth of approximately 40 μK, we were able to obtain 10^5 atoms in each spin state at a temperature, $T/T_F \approx 0.05$, where T_F is the fermi temperature [32]. However, in the course of performing the experiments described in chapters 4 and 5, we found that in order to load only a single layer of the accordion lattice we had to evaporate until we had $\sim$ 2000 atoms in the trap. For so few atoms, the absorption imaging system described in section 1.1.2 is not sensitive enough to characterize the temperature and atom number of the cloud after evaporation and we rely on the site-resolved imaging after the lattice is loaded.

After evaporation, the atoms are loaded into the accordion and transported to the object plane of the high resolution imaging system, as described in [84]. In order to obtain low enough entropies for creating the Mott insulating states and antiferromagnetic correlations described in chapters four and five, we added a second evaporation step just before loading the lattice. The procedure for

evaporating is shown in figure 1.12. Atoms begin in a single layer of the accordion, after compression, with the confinement in the x-y plane set by the dimple trap (section 1.3.1). Just as in the previously described evaporation sequence, we use a magnetic gradient to spill atoms out of the trap. We apply a magnetic gradient in the $-(\hat{x}+\hat{y})$ direction using the radial gradient coil described in section 1.2.2, and control the strenght of the magnetic bias field with the outer Feshbach coils. The additional radial coil was required to produce a gradient in the x-y plane, ensuring that as atoms are pulled out of the optical potential they do not populate multiple layers of the accordion. The gradient is ramped up to 67 G/cm, with a bias of approximately 240 G, and the accordion power is ramped to 1.5 W, the minimum power which ensures that atoms cannot tunnel between planes of the accordion lattice. Forced evaporation is performed by lowering the dimple power exponentially with a time constant of approximately 100 ms to the desired trap depth. As described in Chapter 4, we can use the final trap depth to precisely control the atom number, with fluctuations in the atom number below 5%.

After the evaporation procedure, the gradient is ramped off, and the dimple power is lowered to provide the desired harmonic confinement for loading the lattice. The magnetic bias field is set to control the atomic scattering length. When ramping to repulsive interactions, we use the jump coil described in section 1.2.3 to ramp quickly over the narrow s-wave resonance described in section 2.1.2. At this point the optical lattice is ramped on for performing the experiments described in chapters three through five.

1.5 Lattice calibration

1.5.1 Lattice Depth Calibration

To calibrate the lattice depth we apply lattice modulation spectroscopy and measure the transition frequencies between different energy bands. Resonant transitions to higher bands heat the cloud,

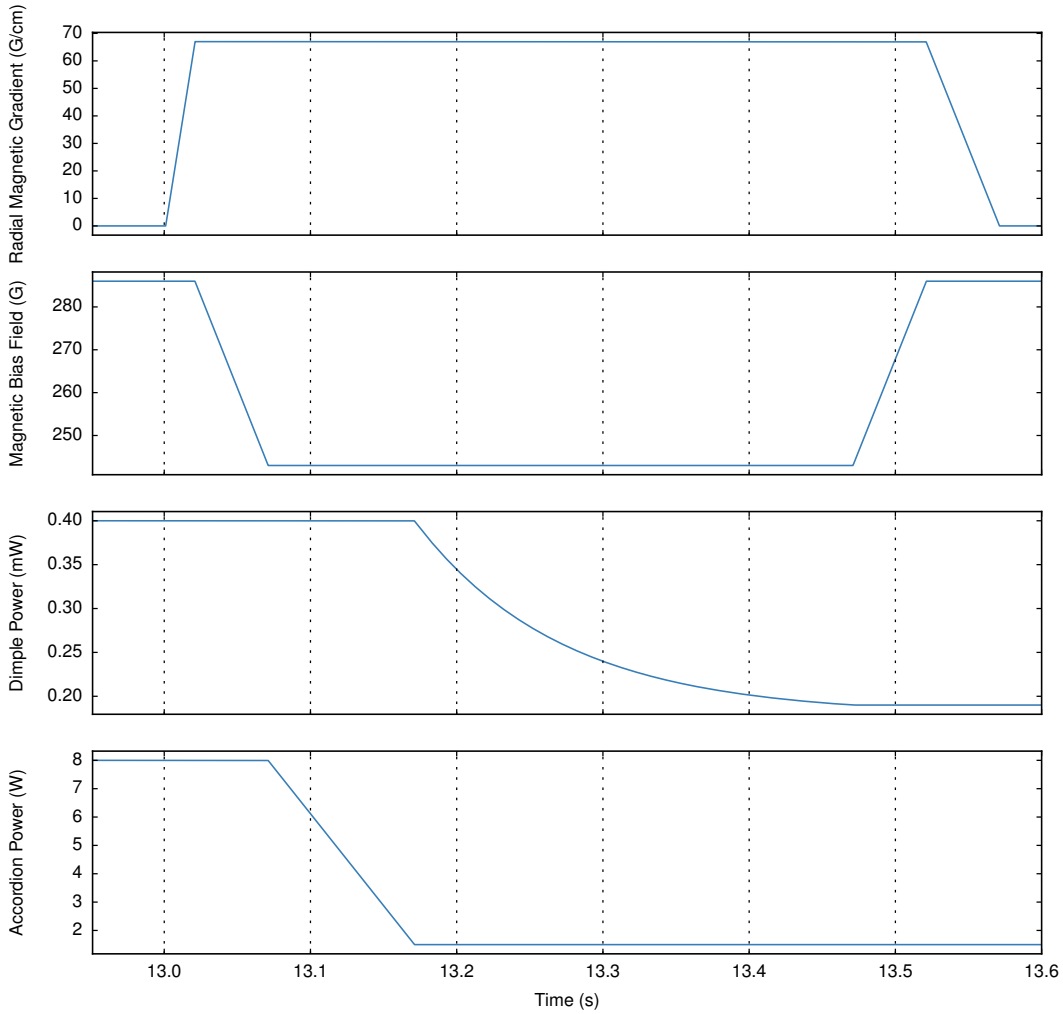

Figure 1.12: Just before loading the lattice, the atoms are evaporated by combining a magnetic field gradient in the $-(\hat{x}+\hat{y})$ direction with forced optical evaporation in the combined dimple and accordion trap.

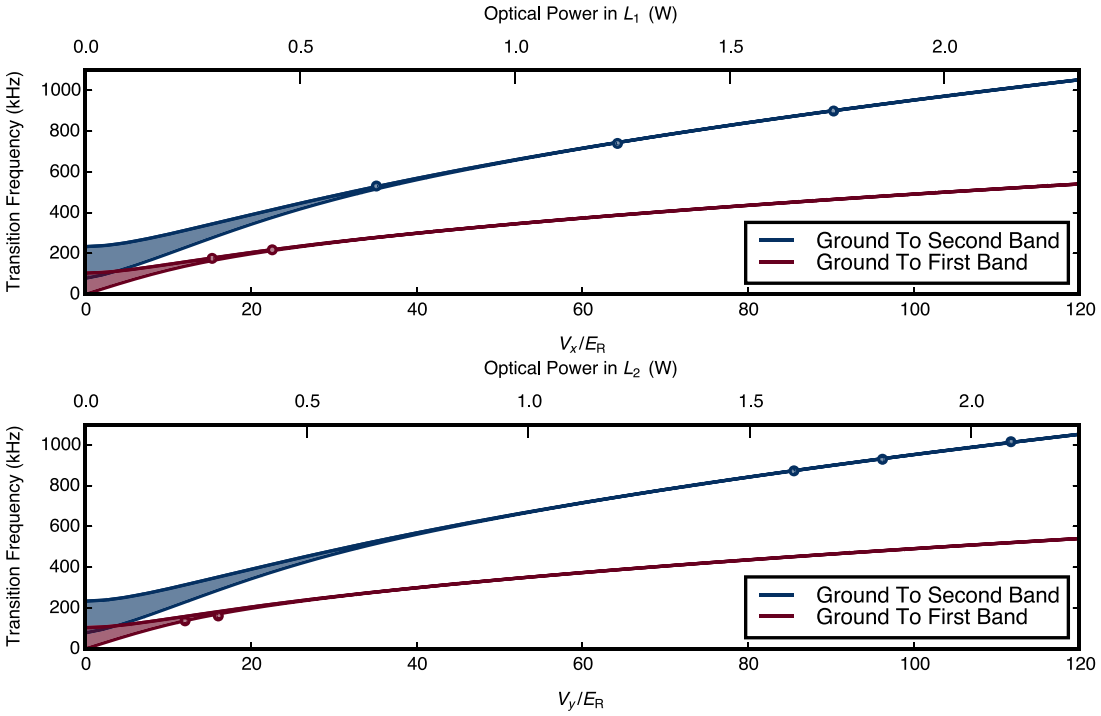

Figure 1.13: Modulating the lattice at twice the band spacing heats the cloud, and this heating manifests itself as an increase in the width of the trapped cloud. By varying the modulation power, and fitting the resulting feature in the cloud width to a Lorentzian, we can determine the inter-band resonance positions. For shallow lattices, the transition between the ground and first excited band can also be driven directly. Plotted above are measured inter-band transitions compared to a best-fit band structure obtained by solving the Mathieu equation (see section 2.2.1).

increasing its width in situ. The atoms are prepared in the lattice at a magnetic field of 528 G, where $|1\rangle + |2\rangle$ spin mixture does not interact. We increase the lattice to a variable power in 50 ms and then modulate at variable frequency ν with approximately 5% modulation depth for 2000 cycles. After the modulation, the lattice is ramped down to a constant depth and held for 10 ms before imaging. We measure the width of the in-situ atom distribution and find heating resonances corresponding to the transition from the ground to the second excited band. We use a Lorentzian fit to determine the resonant frequency. From a fit of the resonance positions to a band structure calculation (section 2.2.1) we calibrate the lattice depths. The results are shown in figure 1.13, where the measured resonant frequencies are in good agreement with the fitted model. For shallow lattices we can directly drive excitations between the ground band and the first excited band. To verify our calibration, we reduce the lattice depth to $V_i \approx 20 E_{\mathrm{R}}$ and drive transition to the first excited band, finding good agreement of the transition frequency with the calculated band structure.

1.5.2 Harmonic Confinement Calibration

The harmonic confinement due to the Gaussian profile of the lattice laser beams is calibrated by observing breathing mode oscillations. We load the atoms into a trap formed by the lattice of interest and the dimple beam. The dimple beam is suddenly switched, exciting breathing mode oscillations along the direction normal to the lattice beam propagation. After a variable oscillation time we pin the atomic distribution by ramping the lattice depths to $V_x = 50.2(7)\ E_{\mathrm{R}}$ and $V_y = 53.8(5)\ E_{\mathrm{R}}$ in 0.1 ms and subsequently image the atomic distribution. A sinusoidal fit to the spatial width of the atomic distribution then yields twice the harmonic trap frequency, as shown in figure 1.14.

1.5.3 Hubbard U Calibration

The on-site interaction U (section 2.2) is calibrated using lattice modulation spectroscopy. A Mott insulator is prepared in an optical lattice with depth $V_{0,x} = 12.5(2)\ E_{\mathrm{R}}, V_{0,y} = 15.9(2)\ E_{\mathrm{R}}$, at

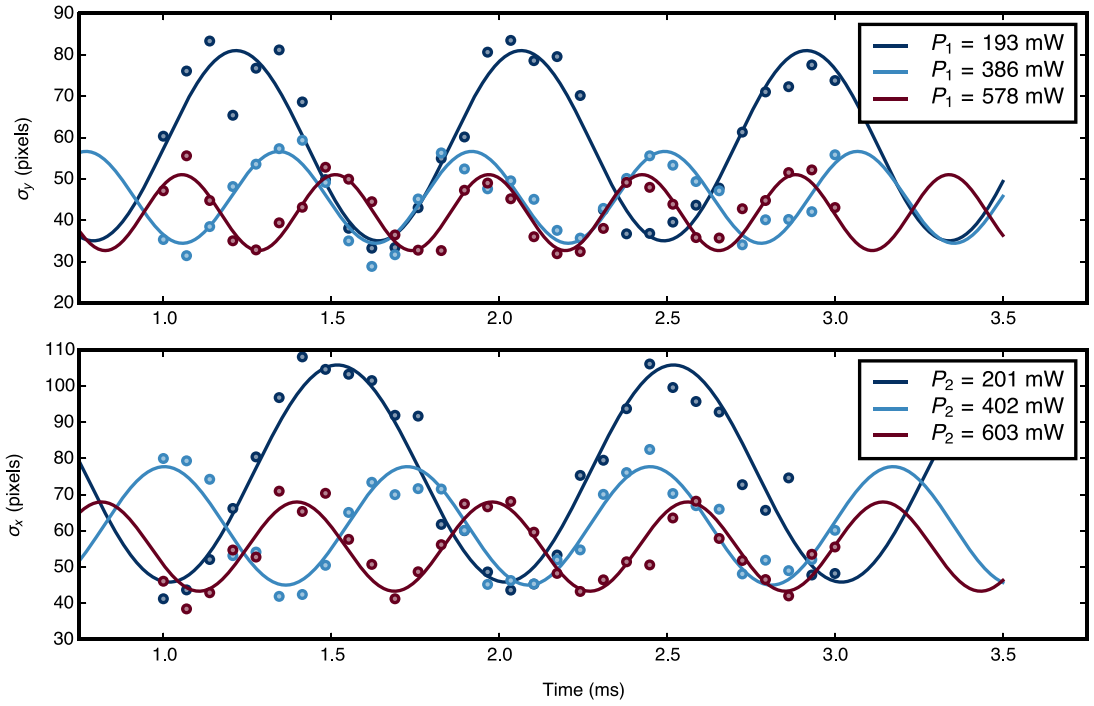

Figure 1.14: Breathing mode oscillations of atoms held in either the X Lattice or the Y Lattice. The standard deviation of the atomic fluorescence signal along the direction orthogonal to the lattice is shown as a function of time after a sudden relaxation of the harmonic confinement. We use fits to a decaying sinusoid to determine the oscillation frequency, which corresponds to twice the trap frequency. From the trap frequencies of individual beams, the underlying harmonic confinement of the lattice can be determined using equation 1.5.

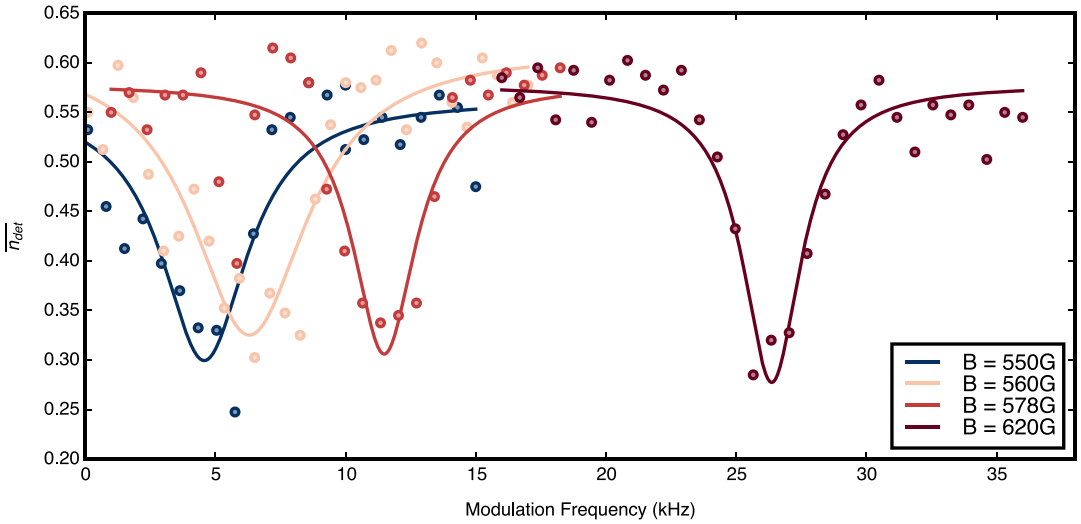

Figure 1.15: Amplitude modulation of one of the lattice beams at a frequency corresponding to the interaction energy, $\nu = U/h$, results in a decrease in the observed filling as doublons are created. The magnetic field is varied, which changes the scattering length and consequently the interaction energy.

$B = \{550, 560, 578, 620\}$ G, corresponding to scattering lengths of $a = \{85, 129, 221, 515\}\, a_0$. The amplitude of the lattice along the x-direction is modulated sinusoidally at variable frequency ν with 10% modulation depth for 20 ms. If the modulation frequency matches the interaction energy, $\nu = U/h$, excitations in the form of doubly-occupied sites are produced, which reduces the observed density $\overline{n_{det}}$. Figure 1.15 shows the averaged density as a function of modulation frequency for several interaction strengths. The positions of the resonances are identified from a Lorentzian fit.

2

Theoretical considerations for ^{6}Li in an optical lattice

In this chapter I provide a description of the theory necessary to describe the experiments with fermionic atoms in Hubbard-regime optical lattices covered in chapters four and five. The chapter begins with a discussion of Feshbach resonances in ^{6}Li, which we use to tune the interactions between atoms. I then discuss the motion of a single particle in a periodic optical lattice potential. Finally, I show that interacting fermions in an optical lattice can be described by the Hubbard model with nearest-neighbor tunneling and on-site interactions. I discuss the high-temperature series expansion for the Hubbard model, providing expressions for the density, double occupancy and single occupancy.

Finally, I describe several properties of the Hubbard model that I have found helpful for developing intuition.

2.1 Feshbach Resonances in ^{6}Li

Because in ultracold atom experiments the extent of the atomic wave-function is generally larger than the range of the inter-atomic potential, the detailed shape of the short-range potential does not matter. In this limit, only the partial wave scattering amplitude with no angular momentum, the s-wave scattering amplitude, plays a role and higher partial wave scattering can be neglected. In this limit the scattering cross section, $\sigma = 4\pi a^2$, is independent of the collision energy and characterized by the scattering length, a [98]. If the extent of the wavefunction (in our context, the Wannier function to be discussed in section 2.2.1) is larger than the scattering length, then the inter-atomic potential between two different spin states can be described by the pseudopotential [99]:

$$V_{int}(\boldsymbol{r} - \boldsymbol{r'}) = \frac{4\pi\hbar^2 a}{m}\delta(\boldsymbol{r} - \boldsymbol{r'}) \tag{2.1}$$

In collisions between ultracold atoms the scattering length can exhibit magnetic field dependent resonances called Feshbach resonances [23]. These resonances occur when a bound molecular state of some "closed channel" inter-atomic potential energetically approaches the scattering state of an "open channel" inter-atomic potential that asymptotically connects free atoms in the limit of large inter-atomic distance. The energy difference between the bound state and scattering state is magnetically tunable when these states have different magnetic moments. The scattering length in the vicinity of a magnetically tunable Feshbach resonance, excluding the effects of two-body inelastic collisions, can be described by [100]

$$a(B) = a_{bg}\left(1 - \frac{\Delta}{B - B_0}\right) \tag{2.2}$$

Here, a_{bg}, is the background scattering length, given by the open channel potential, Δ is the width of the resonance, and B_0 is the resonance location.

In bosonic species, the enhanced scattering cross-section associated with these resonances generally also leads to enhanced three-body loss. Feshbach resonances have found the greatest utility in cold atom experiments with fermions because Pauli blocking suppresses three-body collisional relaxation near a feshbach resonance even on the side of repulsive interactions, where fermions bind to form weakly bound bosonic molecules [101]. Feshbach resonances have enabled Bose-Einstein condensation of fermionic pairs [102, 26, 27, 25] as well as studies of the BEC-BCS crossover [29, 30, 28]. In the experiments described in this thesis, Feshbach resonances are primarily used to enhance the elastic collision cross section during evaporative cooling and to tune the interaction strength in Hubbard-regime lattice experiments. In the remainder of this section I will go over the details of the Feshbach resonances in ^{6}Li as they relate to the rest of the work presented here.

2.1.1 Wide s-wave resonances in ^{6}Li

An appealing feature of ^{6}Li is that there are wide Feshbach resonances at 834 G, 690 G, and 811 G for $|1\rangle + |2\rangle$, $|1\rangle + |3\rangle$, and $|2\rangle + |3\rangle$, respectively with widths of 300 G, 122 G, and 222 G [23]. The positions of these resonances were recently measured to high precision using RF-spectroscopy of weakly bound molecules [103] and the scattering lengths from coupled-channel calculations used in that publication are plotted in figure 2.1 [104]. In our experiment we work exclusively with of atoms in the $|1\rangle$ and $|2\rangle$ states and rely heavily on the associated resonance at 834 G. We use the zero-crossing at 528 G to prepare non-interacting samples for calibrating trap potentials. We use the negative scattering length minimum at $\sim$ 300 G for evaporation. Finally, we can use the wide tunability afforded by the resonance to vary the Hubbard U parameter in optical lattice experiments. While fermionic statistics inhibit inelastic loss directly on a Feshbach resonance [101], enhanced loss due to inelastic three-body collisions is generally observed on the positve-scattering side of

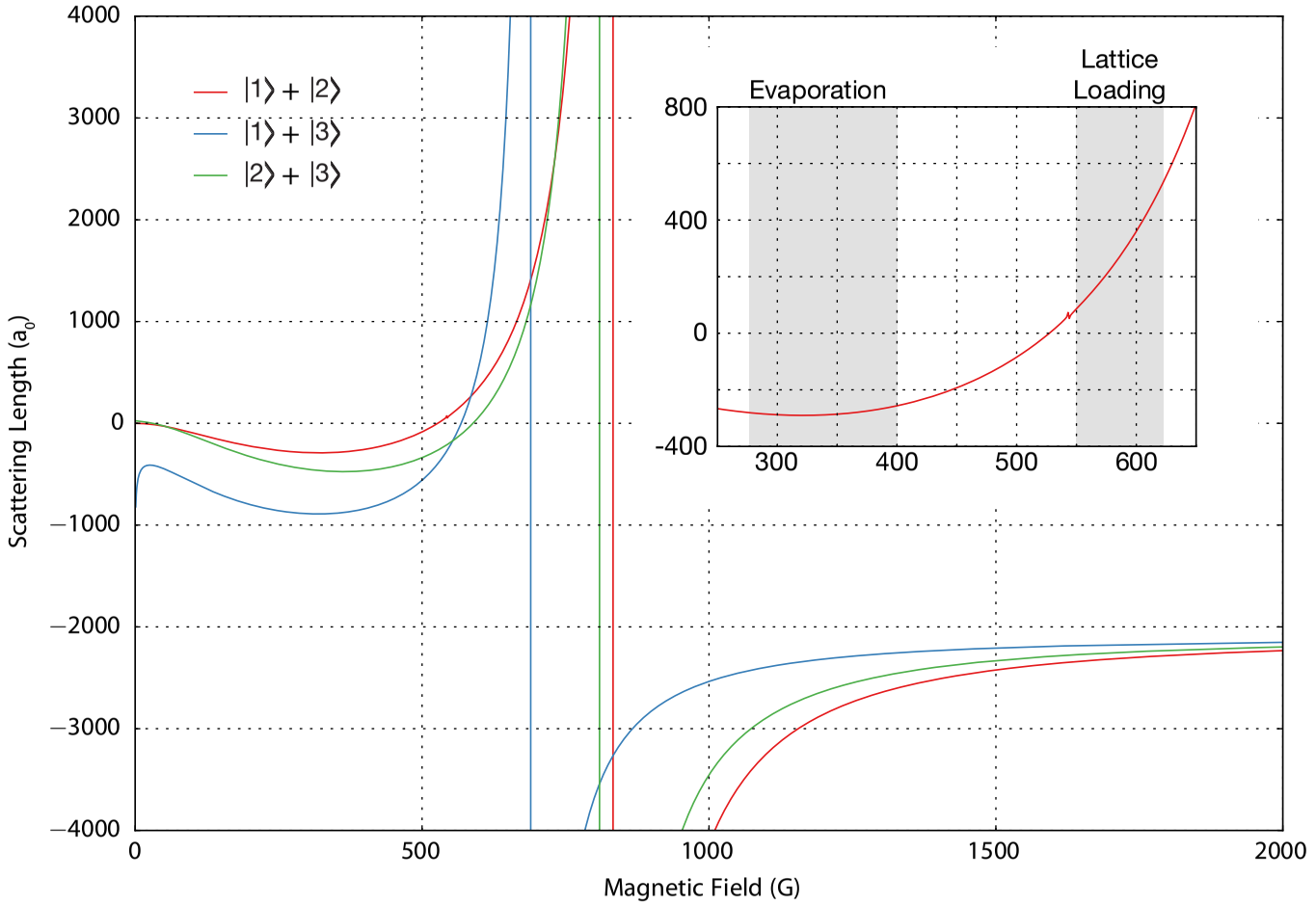

Figure 2.1: The scattering lengths for different hyperfine mixtures of ^{6}Li as determined from a coupled-channels calculation with parameters determined from radio-frequency spectroscopy of weakly bound molecules [103, 104].

the Feshbach resonance [23]. In reference [22] the loss rate was observed at 680 G on the positive scattering length side of the ^{6}Li Feshbach resonance centered at 834 G. To avoid inelastic loss in this region, we avoid loading the lattice at magnetic fields greater than 620 G.

2.1.2 Narrow resonances in ^{6}Li

In addition to the wide resonances discussed above, there are several narrow resonances which we must work around because at our high particle densities ($10^{13} - 10^{14}$ cm^{-3}) they cause heating and atom loss. These include p-wave resonances at 159 G, 185 G, and 215 G for $|1\rangle + |1\rangle$, $|1\rangle + |2\rangle$, and $|2\rangle + |2\rangle$ collisions, respectively [105, 106] and a narraow s-wave resonance at 543 G for $|1\rangle + |2\rangle$ collisions [87].

The narrow s-wave resonance for $|1\rangle + |2\rangle$ collisions at 543 G is closed-channel dominated, and is therefore expected to exhibit large collisional loss due to three-body recombination. This resonance was nonetheless successfully used by the Hulet group to generate a long-lived Bose gas of bound pairs of fermions [87]. Perhaps because we work with atomic densities that are at least an order of magnitude higher than those reported in the Hulet group work, we observe significant heating and atom loss when we cross this resonance. We must cross this narrow resonance between our final evaporation step at 300 G and loading the lattice with a repulsively interacting gas at 550 G$-$620 G, as shown in the inset of figure 2.1. To avoid heating when crossing the resonance we rapidly ramp the field using the jump coil described in section 1.2.3.

Crossing the p-wave resonances is unavoidable as we transport the atoms into the science chamber without a magnetic bias field and evaporate at 300 G. We cross the p-wave resonances just after transport with approximately 1.0×10^6 atoms at 10 μK in the transport trap which as the field is ramped has trap frequencies of approximately (2.25 kHz, 2.25 kHz, 10 Hz), and a central density of $\sim 5 \times 10^{11}$ cm^{-3}. We ramp the field at a rate of approximately 0.1 G/ms. The resonance widths of $\sim$ 150 mG as well as two- and three-body loss coefficients, G_2 and L_3, were measured in [105].

Atom loss due to two- and three-body inelastic collisions can be described are described by

$$\dot{n}(t) = -G_2 n^2(t) - L_3 n^3(t) \tag{2.3}$$

where $n(t)$ is the atomic density. From the values $G_2 \approx 1.0 \times 10^{11}$ cm^3/s and $L_3 \approx 5.0 \times 10^{-24}$ cm^6/s reported in [105] we expect to lose $< 1\%$ of the atoms when crossing this resonance after transport. The associated heating is completely negligible as the main evaporation procedure used to cool the atoms is performed after the crossing. However, if we were to cross this resonance at a density of 1×10^{14} cm^{-3}, which is typical in the accordion and dimple trap just before lattice loading, equation 2.3 predicts that we would lose $> 90\%$ of the atoms.

2.2 Fermions in an optical lattice interacting via contact interactions

The aim of this section is to describe the connection between fermionic atoms trapped in an optical lattice and interacting via contact interactions, and the Hubbard model. This connection has been covered in detail in early theses from the Esslinger and Bloch groups [107, 108, 109, 110]. For new students, I would especially recommend looking at the theses of Robert Jördens [107] and Sebastian Will [110]. I will, as briefly as possible, explain how to determine the Hubbard parameters, U and t, from the lattice depth and scattering length. In addition, I will provide the energy spectrum for our optical lattice in the anharmonic approximation, which I have found especially useful when thinking about Raman sideband cooling, discussed in chapter 3.

2.2.1 Single-Particle Eigenstates in an Optical Lattice

The potential experienced by the atoms in our optical lattice in the absence of interactions, $V_{\text{lat}}(\boldsymbol{r})$, is described by equation 1.4. The energies and eigenstates for this potential can be obtained by

solving the time-independent Schrödinger equation:

$$E\phi(\boldsymbol{r}) = -\frac{\hbar^2}{2m}\nabla^2\phi(\boldsymbol{r}) + V_{\text{lat}}(\boldsymbol{r})\phi(\boldsymbol{r}). \tag{2.4}$$

This equation is separable and so the problem reduces to solving the Schrödinger equation in a single spatial dimension. We can further simplify the problem by ignoring the underlying harmonic potential, which can be taken into account with a local density approximation to be discussed later. The problem is then reduced to solving the Schrödinger equation

$$E\phi(x) = -\frac{\hbar^2}{2m}\partial_x^2\phi_x(x) - V_0\cos^2(\pi x/a)\phi_x(x) \tag{2.5}$$

It is convenient to rewrite this equation in more natural units with $\tilde{x} = \pi x/a$, and $E_r = h^2/(8ma^2)$:

$$\epsilon\phi(\tilde{x}) = -\partial_{\tilde{x}}^2\phi(\tilde{x}) - s_0\cos^2(\tilde{x})\phi(\tilde{x}), \tag{2.6}$$

where $\epsilon = E/E_r$ and $s_0 = V_0/E_r$.

Band Structure

The stationary states of a particle in a period potential can described by band structure via Bloch's theorem [111], which states that the eigenstates, $\phi_{\boldsymbol{q}}^{(n)}$ of the single-particle Hamiltonian, $H = -\hbar^2\nabla^2/2m + U(\boldsymbol{r})$, where $U(\boldsymbol{r})$ is periodic in all Bravais lattice vectors, are of the form:

$$\phi_{\boldsymbol{q}}^{(n)}(\boldsymbol{r}) = e^{\boldsymbol{q}\cdot\boldsymbol{r}}u_{\boldsymbol{q}}^{(n)}(\boldsymbol{r}), \tag{2.7}$$

where the functions $u_{\boldsymbol{q}}^{(n)}$ have the same periodicity as the potential, $U(\boldsymbol{r})$. The band index is denoted by n, and $\boldsymbol{q}$ is called the quasi-momentum. By using the Bloch wavefunctions, $u_{\boldsymbol{q}}^{(n)}(\boldsymbol{r})$, in equation

2.7 as an ansatz for the Schrödinger equation, and then writing each term in the result as a discrete Fourier sum, one can construct a plane-wave representation of the Hamiltonian which can then be numerically diagonalized. This procedure is carried out explicitly for a sinusoidal lattice in reference [112].

From a linear combination of Bloch wavefunctions in a particular band, one can construct a Wannier function for a lattice site at $\boldsymbol{r}_i$ that is orthogonal to the Wannier function on a other lattice site [113]:

$$w^{(n)}(\boldsymbol{r}) = \frac{1}{\sqrt{N}} \sum_{\boldsymbol{q}} e^{-i\boldsymbol{q}\cdot\boldsymbol{r}_i} u_{\boldsymbol{q}}^{(n)}(\boldsymbol{r}), \tag{2.8}$$

which satisfies the orthonormality relation

$$\int d^3\boldsymbol{r} w^{(n)}(\boldsymbol{r} - \boldsymbol{r}_i) w^{(n')}(\boldsymbol{r} - \boldsymbol{r}_j) = \delta_{ij}\delta_{nn'}. \tag{2.9}$$

Here the sum is over a finite number, N, of quasi-momenta which is determined by some boundary condition. The orthonormality relation of equation 2.9 allows one to write the second-quantized field operator in the basis of Wannier functions, which I will use later when constructing the Hubbard model.

Mathieu Equation

With a simple trigonemtric identity, equation 2.5 can be written in the form of the Mathieu equation:

$$\begin{aligned} &\frac{\partial^2\phi(\tilde{x})}{\partial\tilde{x}^2} + [a - 2q\cos(2\tilde{x})]\phi(\tilde{x}) = 0 \\ &a = \epsilon - \frac{s_0}{2} \\ &q = \frac{s_0}{4} \end{aligned} \tag{2.10}$$

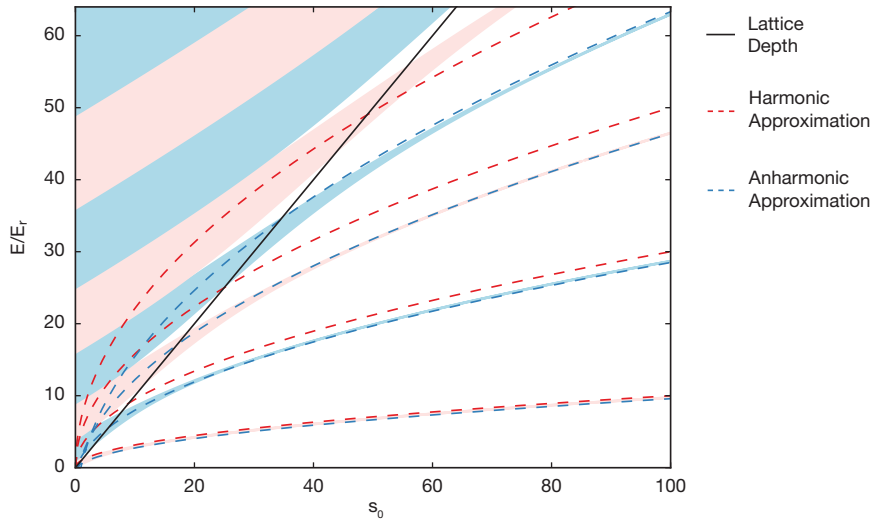

Figure 2.2: A comparison of lattice energy levels versus lattice depth, calculated from the stability diagram of the Mathieu equation (shaded regions), a harmonic oscillator approximation on each lattice site (red dashed line), and an anharmonic approximation on each lattice site (blue dashed line). The lack dashed line denotes the lattice depth.

The Mathieu equation only admits stable solutions for certain values of a and b. These regions of stability give rise to the energy bands expected from a periodic potential. A stability diagram for this equation which gives the energy ranges of each band of the lattice is given in figure 2.2. A thorough discussion of the application of the Mathieu equation to energy bands in physics can be found in reference [114].

Approximations for deep lattices

We can expand the potential energy term in equation 2.5 in a Taylor series around each potential minimum, $x_0 = {}^{na}/_2$, approximating the trap as an anharmonic oscillator:

$$V_0 \cos^2({}^{\pi x}/_a) \approx \frac{\pi^2 V_0}{a^2}(x - x_0)^2 - \frac{\pi^4 V_0}{3a^4}(x - x_0)^4. \tag{2.11}$$

By comparing the quadratic term to the potential energy of a harmonic oscillator, $\frac{1}{2}m\omega^2x^2$, we can read off the trap frequency, ω, giving $\hbar\omega/E_r = \sqrt{4s_0}$. The eigenenergies in the purely harmonic approximation are

$$\frac{E_n^{(\text{sho})}}{E_r} = (n + 1/2)\sqrt{4s_0}. \tag{2.12}$$

We can then apply time-independent first-order perturbation theory, making use of ladder operators, to determine the energy shift due to the quartic (anharmonic) term in equation 2.11:

$$\frac{\delta E_n^{(\text{ah})}}{E_r} = -\frac{6n^2 + 7n + 5}{12}. \tag{2.13}$$

A feature of this result that is perhaps counter-intuitive is that the anharmonic correction does not depend on the lattice depth. Figure 2.2 shows the energy levels in this deep lattice approximation with and without the quartic correction, compared to the band-structure results obtained by solving the Mathieu equation.

These results are particularly useful when considering Raman sideband cooling (Chapter 3), as we work in the limit of deep lattices and are particularly interested in the difference energy between neighboring levels, as this determines the two-photon detuning for the first motional sideband. This energy difference is

$$\frac{E_n^{(\text{aho})} - E_{n-1}^{(\text{aho})}}{E_r} = \sqrt{4s0} - \frac{13 + 12n}{12} \tag{2.14}$$

This provides a practical rule of thumb: as one goes up the ladder of motional eigenstates, the frequency of a transition to the next motional state is red-detuned by one recoil when compared to the same transition for the previous state. This potentially limits the capture range of Raman sideband cooling. Anharmonicity is an important effect when driving Raman transitions for lighter atoms like ^{6}Li for which the recoil energy is larger.

2.3 The Hubbard Model

2.3.1 Constructing the Hubbard Model

It was first shown by Jaksch et al. [16] that interacting bosonic atoms in an optical lattice can be described by the Bose-Hubbard model. Here, I follow the arguments presented in that paper to show that the dynamics of two-component fermionic atoms in an optical lattice are described by the Hubbard model. Atoms trapped in a lattice with potential, $V_{\text{lat}}(\boldsymbol{r})$, and interacting via s-wave scattering, parametrized by the scattering length, a, are described by the Hamiltonian

$$\begin{aligned}\hat{H} = &\int d^3\boldsymbol{r}\hat{\psi}^\dagger(\boldsymbol{r})[-\frac{\hbar^2}{2m}\nabla^2 + V_{\text{lat}}(\boldsymbol{r})]\hat{\psi}(\boldsymbol{r}) \\ &+ \frac{1}{2}\frac{4\pi a\hbar^2}{m}\sum_{\sigma,\sigma'}\int d^3\boldsymbol{r}\hat{\psi}^\dagger_{\sigma'}(\boldsymbol{r})\hat{\psi}^\dagger_{\sigma}(\boldsymbol{r})\hat{\psi}_{\sigma}(\boldsymbol{r})\hat{\psi}_{\sigma'}(\boldsymbol{r}).\end{aligned} \tag{2.15}$$

Here, $\hat{\psi}_\sigma(\boldsymbol{r})$, is the field operator for a fermion with spin σ. Following reference [16], and assuming that only the lowest band of the lattice is occupied, we can write the field operator in the basis of Wannier functions: $\hat{\psi}_\sigma(\boldsymbol{r}) = \sum_i w_i(\boldsymbol{r})\hat{c}_{i,\sigma}$. Here, $\hat{c}_{i,\sigma}$ is the annhilation operator for a fermion on site i with spin $\sigma \in \{\uparrow,\downarrow\}$. This representation restricts the field operator to a Hilbert space whose basis representations are functions that are periodic with the lattice. This is not generally valid — for example, it would not be valid if the interaction, or any additional term in the Hamiltonian did not have translational symmetry — but in this case the interaction is translationally symmetric. Plugging this representation of the field operator into equation 2.15 gives the Hubbard Hamiltonian,

$$H = -t\sum_{\langle i,j\rangle,\sigma}(\hat{c}^\dagger_{i,\sigma}\hat{c}_{j,\sigma} + h.c.) + U\sum_i \hat{n}^\dagger_{i,\uparrow}\hat{n}_{i,\downarrow}, \tag{2.16}$$

where $\hat{n}_{i,\sigma} = \hat{c}^{\dagger}_{i,\sigma}\hat{c}_{i,\sigma}$ The tunneling and interaction parameters, t and U, are given by

$$\begin{aligned} t &= \int d^3\boldsymbol{r} w_i^*(\boldsymbol{r})[-\frac{\hbar^2}{2m}\nabla^2 + V_{\text{lat}}(\boldsymbol{r})]w_{i+1}(\boldsymbol{r}) \\ U &= \frac{4\pi a\hbar^2}{m}\int d^3\boldsymbol{r}|w_0(\boldsymbol{r})|^4 \end{aligned} \tag{2.17}$$

The sum of $\langle i, j\rangle$ in equation 2.16 indicates a sum over nearest-neighbors. In the above equations, the tight-binding approximation has been made: we have assumed that the tunneling integral is only significant between neighboring sites, and in writing the interaction integral assumed that the wannier function density does not have significant overlap between nearest-neighbor sites and beyond. For shallow lattices these approximations break down. Next-nearest neighbor tunneling can easily be included by including another tunneling term in the model with a tunneling integral of the same form but taken for next-nearest neighbor Wannier functions. A plot of the strengths of next- and next-next-nearest neighbor tunneling relative to nearest-neighbor tunneling as a function of lattice depth can be found in reference [115]. At a lattice depth of $4\ \mathrm{E_r}$ the next-nearest neighbor tunneling is approximately 7% of the nearest-neighbor tunneling.

Often, we'd like to consider the Hubbard model in a grand canonical ensemble where the number of particles can vary and this is parametrized by a chemical potential, μ. It can be convenient to insert the chemical potential term into the Hamiltonian:

$$H = -t\sum_{\langle i,j\rangle,\sigma}(\hat{c}^{\dagger}_{i,\sigma}\hat{c}_{j,\sigma} + h.c.) + U\sum_i \hat{n}^{\dagger}_{i,\uparrow}\hat{n}_{i,\downarrow} - \mu\sum_{i,\sigma}\hat{n}_{i,\sigma} \tag{2.18}$$

2.3.2 High temperature series expansions for the 2D Hubbard model

Series expansions provide a relatively simple analytic approach to approximating thermodynamic observables for lattice systems involving spin and charge degrees of freedom [116]. The experiments

described in chapter 4 of this thesis probe a parameter regime of the Hubbard model that is well-suited to a high-temperature series description. The high-temperature series expansions for the Hubbard model have been worked out to eighth order for simple cubic and square lattices in references [117, 118]. A well-explained overview of the method is provided in [49], along with expressions for the grand potential for square, cubic and dimerized lattices.

The basic idea behind the high-temperature series expansion of the Hubbard model is to treat the tunnel coupling as a perturbation to the on-site interaction. One can then expand the partition function, $\mathcal{Z}$, in powers of βt, where $\beta = 1/k_B T$. The difficulty in the procedure is grouping and appropriately counting terms that are of the same order in βt, for which a graphical approach is typically used. The expansion is generally valid for $U \gg t$ and $k_B T \gg t$. The regimes of convergence for the Hubbard model expansion are looked at in [107] through comparison to a dynamical mean field theory calculation.

Results for a square lattice

The grand potential per site, Ω^s, to second order in the high-temperature expansion is given in [43]:

$$-\beta\Omega^s = \log(z_0) + (\beta t)^2 \frac{2}{z_0^2}[2\zeta(1+\zeta^2 w) - \frac{4\zeta^2}{\log(w)}(1-w)], \tag{2.19}$$

where,

$$\begin{aligned} \zeta &= e^{\beta\mu} \\ w &= e^{-\beta U} \\ z_0 &= 1 + 2\zeta + \zeta^2 w. \end{aligned} \tag{2.20}$$

The density, n, and double occupancy, d, can be obtained from derivatives of the grand potential

per site:

$$
\begin{aligned}
n &= -\frac{\partial \Omega^s}{\partial \mu} = -\beta\zeta \frac{\partial \Omega^s}{\partial \zeta} \\
&= \frac{2\zeta + 2w\zeta^2}{z_0} + 2(\beta t)^2 \Big(\frac{4w\zeta^3 + 2\zeta(1 + w\zeta^2) - \frac{8(1-w)\zeta^2}{\log w}}{z_0^2} \Big) \\
&\quad - 4(\beta t)^2 \Big(\frac{(2\zeta + 2w\zeta^2)\big(2\zeta(1 + w\zeta^2) - \frac{4(1-w)\zeta^2}{\log(w)}\big)}{z_0^3} \Big)
\end{aligned}
\tag{2.21}
$$

$$
\begin{aligned}
d &= \frac{\partial \Omega^s}{\partial U} = -\beta w \frac{\partial \Omega^s}{\partial w} \\
&= \frac{\zeta^2 w}{z_0} + 2(\beta t)^2 \Big(\frac{2\zeta^3 w + \big(\frac{4(1-w)\zeta^2}{\log(w)^2}\big) + \big(\frac{4w\zeta^2}{\log(w)}\big)}{z_0^2} \Big) \\
&\quad + 4\zeta^2 w(\beta t)^2 \Big(\frac{2\zeta(1 + w\zeta^2) - \frac{4(1-w)\zeta^2}{\log(w)}}{z_0^3} \Big)
\end{aligned}
$$

From the n and d one can easily compute the single occupancy which is simply $n_s = n - 2d$, which is the main observable in the experiments described in chapter 4.

2.3.3 Local Density Approximation

An important detail that we have ignored up to this point is the external confinement due to the finite waists of the lattice beams. The high-temperature series described above is computed assuming a homogeneous system, with a fixed, uniform density determined by the chemical potential. The numerical-linked cluster expansion and dynamical cluster approximation theories that we compare to our results in the compressible regime of the Hubbard model in chapter 5 also assume a homogeneous system. If the external trapping potential varies sufficiently slowly a local density approximation (LDA) can be used. Under the LDA, the system has a global temperature and the chemical potential becomes a local quantity that is shifted by the local trap potential:

$$
\mu_i = \mu - V_i \tag{2.22}
$$

The LDA breaks down when the length scale of correlations becomes large. This breakdown certainly occurs near a phase transition, where correlation lengths diverge, and this breakdown has been studied numerically in the context of the Mott insulator transition in the Bose-Hubbard model and in inhomogeneous Ising models [119, 120]. A naive rule for the breakdown of LDA might come from comparing the variation of the chemical potential over the correlation length to other energy scales in the system. In the experiments described in chapter 4, we look at different phases of the Hubbard model in a harmonic trap, and find good quantitative agreement between the atomic density and the predictions of a second-order high-temperature series expansion. The expansion describes clusters of sites with maximum size given by the order of the expansion, and so only nearest-neighbor correlations are described by the model. The maximum nearest-neighbor chemical potential difference occurs at the edge of the cloud and is approximately 1.3 kHz for the experiments in chapter 4. This is significantly larger than the tunneling energy of 200 Hz, and so we might worry that the LDA is not a good approximation. Nonetheless, comparison of dynamical mean-field theory calculations with and without an LDA for a three-dimensional Hubbard model show good agreement in the density even where the nearest-neighbor chemical potential offset is larger than the tunneling [121]. Testing the validity of the LDA experimentally would require a reliable, independent measurement of the chemical potential and temperature, as well as a model-independent way to verify that the system is in thermal equilibrium. As discussed in the next section, it may be possible to independently measure the chemical potential by exploiting the particle-hole symmetry of the Hubbard model at half-filling. It may also be possible independently measure the temperature by fitting the wings of the cloud to a non-interacting theory, or a weakly-interacting theory employing a low-density approximation.

2.3.4 Some properties of the Hubbard model

Particle-hole symmetry at half-filling

Let's consider the Hubbard model, including the chemical potential term, as described in equation 2.18. If we make a particle hole transformation:

$$\begin{aligned} \hat{c}^{\dagger}_{i,\sigma} &\longrightarrow \hat{c}_{i,\sigma}, \hat{c}_{i,\sigma} \longrightarrow \hat{c}^{\dagger}_{i,\sigma} \\ \hat{n}_{i,\sigma} &\longrightarrow \hat{1} - \hat{n}_{i,\sigma} \equiv \hat{h}_{i,\sigma}. \end{aligned} \tag{2.23}$$

The second line in this transformation follows directly from the first, taking into account the fermionic commutation relation for $\hat{c}$. If we perform this transformation on the Hubbard model the result is:

$$H \rightarrow -t \sum_{\langle i,j\rangle,\sigma} (\hat{c}^{\dagger}_{i,\sigma}\hat{c}_{j,\sigma} + h.c.) + U \sum_{i} \hat{h}_{i,\uparrow} h_{i,\downarrow} - (\mu - U) \sum_{i,\sigma} \hat{h}_{i\sigma} + N(U - 2\mu), \tag{2.24}$$

where N is the number of sites. When $\mu = U/2$ the right-hand side becomes exactly the Hubbard Hamiltonian in equation 2.18, but with $\hat{n}$ replaced by $\hat{h}$. This shows that at $\mu = U/2$ the energy cost of a doubly-occupied site is exactly the same as the energy cost of an unoccupied site. On average, there will be one particle per site, corresponding to a half-filled band. Furthermore, when this condition for half-filling is met, the probability of finding a single particle on any site will be larger than for any other value of μ. This is useful in our experiments. What we are able to see with site-resolved imaging are the singly-occupied sites, and we cannot distinguish between doubly-occupied and unoccupied sites. The trapping potential creates an inhomogeneous chemical potential across a sample. By finding the contour in an in-situ image where the number of singly-occupied sites is maximized, we can find the location of half-filling and if we know the value of U and the shape of the underlying trapping potential, we have an independent calibration of μ. This is used extensively in Chapter 5 in order to compare our experimental observations of antiferromagnetic correlations to

numerical studies, where data is only available at half-filling.

Exchange Energy

By doing a simple time-independent perturbation theory calculation on a two-site Hubbard model, we can see the energy scale of the exchange process which gives rise to antiferromagnetic ordering. Here, I consider the Hubbard model presented in equation 2.16 with the tunneling term as a perturbation. I will only consider the sector of the Hilbert space where there are two particles. In the limit where there is no tunneling it is clear that the Hubbard model is diagonal in the Fock basis where particles are localized to a single-site. I wish to compare the energies of the ferromagnetic and antiferromagnetic states, $|\text{FM}\rangle = |\uparrow,\uparrow\rangle$ and $|\text{AFM}\rangle = |\uparrow,\downarrow\rangle$ in the presence of the tunneling perturbation. Because the Hubbard Hamiltonian is symmetric under a spin-flip, these states will always be degenerate with their spin-flipped counterparts, $|\downarrow,\downarrow\rangle$ and $|\downarrow,\uparrow\rangle$. In the absence of the tunneling term $|\uparrow,\uparrow\rangle$ and $|\uparrow,\downarrow\rangle$ are degenerate with zero energy.

The tunneling term has no effect at first order in perturbation theory and so we must start with second order. Since there is no term in the Hubbard Hamiltonian that can flip a spin there is no intermediate state for $|\text{FM}\rangle$ to couple to and its energy will remain unchanged. The tunneling term, however, does couple $|\text{AFM}\rangle$ to the states $|\psi_{\text{int}}\rangle \in \{|\uparrow\downarrow,\quad\rangle, |\quad,\uparrow\downarrow\rangle\}$, both of which have energy U. To second order in perturbation theory, the energy shift of $|\text{AFM}\rangle$ is then

$$\delta E_{\text{AFM}} = t^2 \sum_{\psi_{\text{int}}} \frac{|\langle\psi_{\text{int}}| \sum_{\langle i,j\rangle,\sigma} (\hat{c}^\dagger_{i,\sigma}\hat{c}_{j,\sigma} + h.c.)|\text{AFM}\rangle|^2}{E_{\text{AFM}} - E_k} = -\frac{2t^2}{U}. \tag{2.25}$$

In this computation I have used hard wall boundary conditions. The result would differ by a factor of order unity in the case of periodic boundary conditions. The factor of two in the numerator should therefore be taken with a grain of salt. The main point is that the tunneling term in the atomic limit of large interactions lowers the energy scale of the antiferromagnetic state by roughly

the exchange energy, $J = t^2/U$. For larger Hubbard systems in thermal equilibrium, antiferromagnetic spin correlations begin to appear when the temperature becomes comparable to the exchange energy. Chapter 5 presents experimental investigations of antiferromagnetic correlations in the Hubbard model.

3

Site-resolved imaging of ^{6}Li atoms using Raman sideband cooling

The challenge of site-resolved imaging of atoms in optical lattices is collecting enough photons to be able to resolve atoms on neighboring sites before the atoms thermally hop between sites. The first demonstration of site-resolved imaging was with Cesium atoms in a lattice with $4.9\mu m$ spacing [56]. In that experiment the authors were able to image a single plane of an optical lattice with many planes occupied. This was possible because the lattice spacing was significantly larger than the 2.8-micron depth of field of the imaging system. Having a lattice spacing that is much larger than the point-spread-function of the imaging system also reduces the number of photons that must

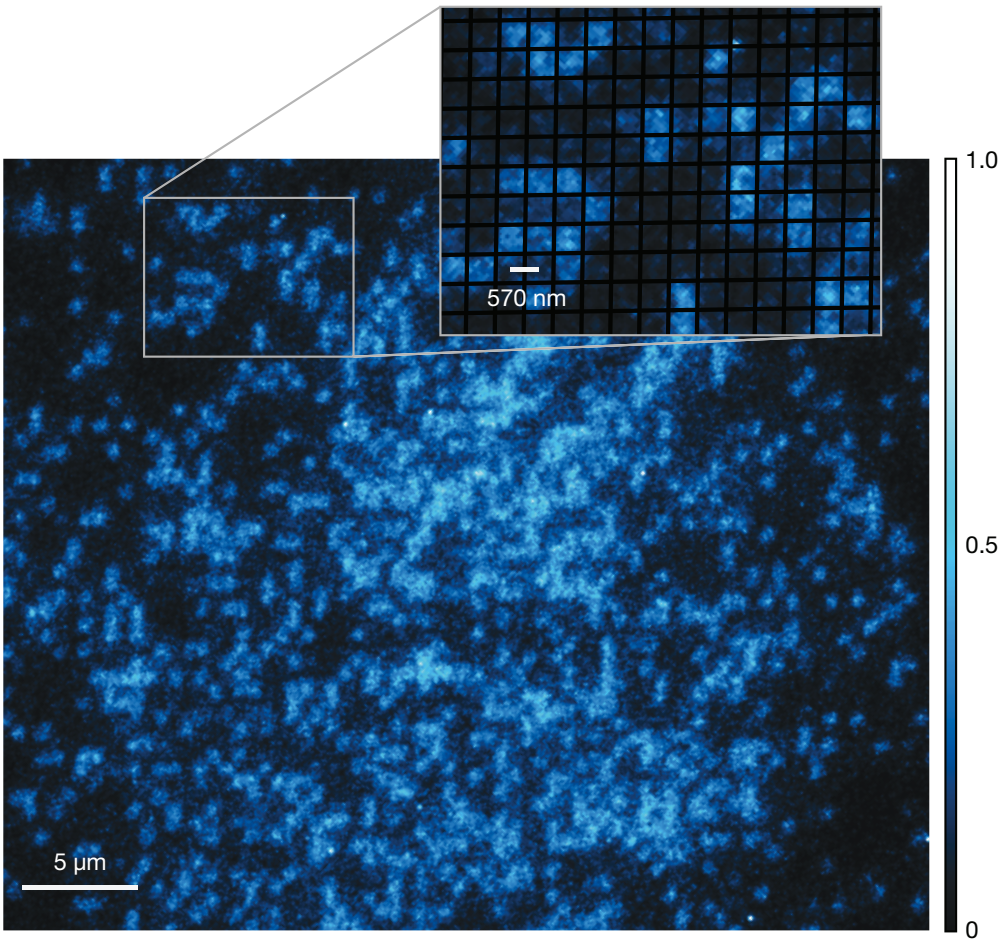

Figure 3.1: Site-resolved image of ^{6}Li atoms in an optical lattice.

be collected in order to identify whether a site is occupied. For experiments that wish to explore many-body physics in optical lattices, however, the lattice spacing must be sufficiently small to allow tunneling between neighboring sites. This typically requires lattice spacings to be on the order of the wavelength of visible light, close to the limit of optical resolution. The resulting large overlap between point spread functions on neighboring lattice sites requires hundreds of photons to be collected in order to determine with high fidelity whether a site is occupied. For even rather large numerical aperture imaging systems thousands of photons must be scattered off of the atoms, requiring a combination of deep optical lattices and sub-doppler cooling to prevent thermal hopping. To cool atoms in the lattice during fluorescence imaging, previous quantum gas microscopes have used a polarization gradient cooling (PGC) scheme for imaging ^{87}Rb [58, 59]. PGC is not suitable for sub-Doppler cooling of ^{6}Li due to the unresolved hyperfine splitting in the excited state [122]. Sisyphus cooling has been demonstrated for ^{6}Li in free space [123] and gray-molasses cooling has been demonstrated for ^{6}Li both in free space and in an optical dipole trap [124]. These cooling techniques, however, have not yet been extended to the tightly-confined regime of optical lattices with ^{6}Li. In the experiments presented in this thesis, we use Raman sideband cooling because it does not rely on resolved hyperfine structure and has been demonstrated to cool a variety of atomic species to the motional ground state in optical lattices [125, 126], optical tweezers [127, 128], and ion traps (where the technique was first developed) [129]. Raman sideband cooling has also recently been used to image ^{87}Rb atoms in optical tweezers [130] and optical lattices [131].

In this chapter I present the first demonstration of site-resolved imaging of ^{6}Li atoms in an optical lattice. To achieve this we perform Raman sideband cooling on atoms loaded into a single layer of a 3D optical lattice as described in [81]. The fluorescence emitted during the cooling process is imaged onto a camera using a high numerical aperture (NA) imaging system described in this chapter. Using this method we are able to determine the occupation of individual lattice sites with a fidelity $> 99\%$. An example image of ^{6}Li atoms generated with this method is shown in figure 3.1.

This technique creates the opportunity to study site-resolved occupation statistics and correlations for fermionic lattice systems.

3.1 Raman sideband cooling

Raman sideband cooling combines coherent two-photon transitions between the internal and motional states of an atom with optical pumping to cool atoms to temperatures below the Doppler limit. First, a coherent Raman transition drives an atom between two stable internal states, typically hyperfine states of an atom or ion in its electronic ground state, while at the same time removing a quantum of external motion. Subsequently, the atom is optical pumped back into the initial internal state. If the motional energy removed in the Raman transition is larger than the recoil energy gained in the optical pumping process, the atom is cooled. The atom can be cooled below the Doppler limit because the two-photon coupling provides enough spectral resolution to resolve motional transitions even when the energy splitting between different motional eigenstates is significantly smaller than the linewidth of a single-photon electronic transition.

3.1.1 Stimulated Raman transitions for tightly bound atoms

In this section the coupling of two hyperfine ground states of a tightly bound atom with a coherent Raman transition is discussed. We consider an atom in monochromatic pump and stokes light fields that are near-detuned to a resonance with an excited electronic state, as depicted in figure 3.2.

Coupling the internal degrees of freedom

Following the treatment in [132], we can write the two-photon Rabi frequency, Ω_c that characterizes the coupling strength between the internal degrees of freedom as a sum over couplings through each

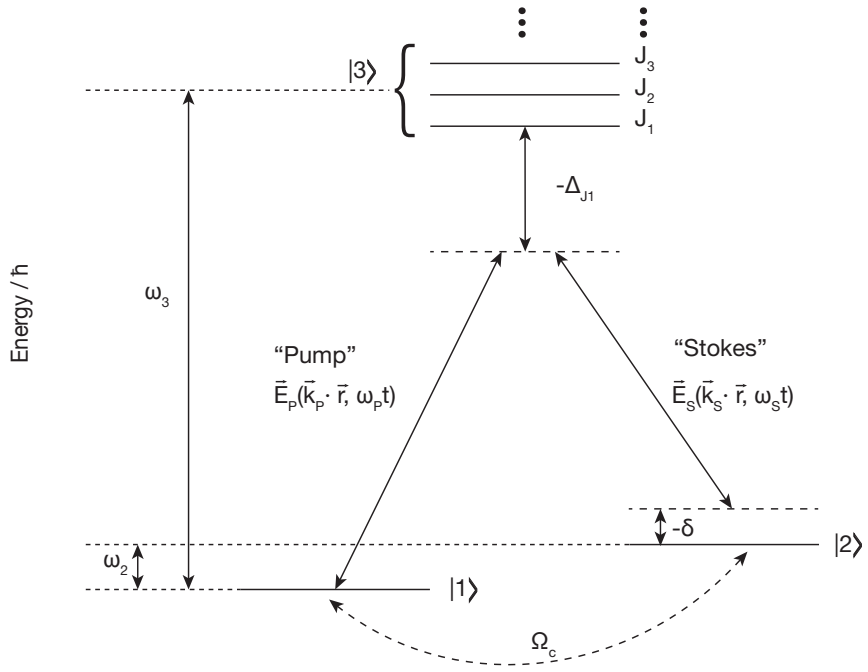

Figure 3.2: We consider a two-photon transition that couples two stable ground states, $|1\rangle$ and $|2\rangle$ via an intermediate electronic manifold, $|3\rangle$, with multiple fine structure components labeled J_1, J_2, ... The excited states can be adiabatically eliminated, as described in[132], and the system can be described by a two-level system where $|1\rangle$ and $|2\rangle$ are coupled with Rabi frequency Ω_c.

excited state.

$$\Omega_c = \sum_i \frac{\langle J_i||\hat{\mu}||J'\rangle}{2\Delta_{J_i}} |E_P E_S||\boldsymbol{G}_P^{(J_i)} \cdot \boldsymbol{G}_S^{(J_i)}|. \tag{3.1}$$

Here, we neglect the energy splitting between hyperfine states in each fine structure manifold with total electronic angular momentum J, but do take into account the fine structure splitting. The term $\langle J_i||\hat{\mu}||J'\rangle$ is the reduced matrix element of the electric dipole operator from the Wigner-Eckart theorem [133] connecting an excited electronic state with angular momentum, J, to a ground electronic state with angular momentum J'. The values of the reduced matrix elements for D1 and D2 lines of ^{6}Li can be found in appendix A. E_p and E_s are the electric field amplitudes of the pump and stokes beams, respectively, which have polarizations $\boldsymbol{\epsilon}_P$ and $\boldsymbol{\epsilon}_S$. The vectors $\boldsymbol{G}_P^{(J_i)}$ and $\boldsymbol{G}_S^{(J_i)}$ are vectors of geometric couplings for the pump and stokes beams, with each element of the vector corresponding to a different state in the excited electronic fine-structure manifold with angular momentum J_i. The elements of the geometric coupling vectors are given by

$$\begin{aligned} G = &\sum_{q\in\{-1,0,1\}} \epsilon_q (-1)^{2F'+J+I+m_F} \sqrt{(2F'+1)(2F+1)(2J+1)} \\ &\times \begin{pmatrix} F' & 1 & F \\ m'_F & q & -m_F \end{pmatrix} \begin{Bmatrix} J & J' & 1 \\ F' & F & I \end{Bmatrix}. \end{aligned} \tag{3.2}$$

The matrix-like symbol in parentheses (...) is a Wigner 3-j symbol and the matrix-like symbol in curly braces {...} is a Wigner 6-j symbol. The dependence of $\boldsymbol{G}$ on the light field (pump or stokes) in this expression comes about through the spherical components of the polarization unit vector, ϵ_q [134]. Values for the geometric couplings for the ground hyperfine states of ^{6}Li are given in tables 3.1 and 3.2.

	$\lvert m_F = -3/2\rangle$	$\lvert m_F = -1/2\rangle$	$\lvert m_F = 1/2\rangle$	$\lvert m_F = 3/2\rangle$
$\langle m_F = -1/2\rvert$	-0.27	0	0.16	0
$\langle m_F = 1/2\rvert$	0	-0.16	0	0.27

Table 3.1: The geometric coupling factors, $\boldsymbol{G}_P^{(1/2)} \cdot \boldsymbol{G}_S^{(1/2)}$ for a two-photon coupling between each magnetic sublevel of the $F = 1/2$ and $F = 3/2$ ground states of ^{6}Li, coupled through the $2P_{1/2}$ excited state manifold (the D1-line), for the polarization vectors, $\hat{\epsilon}_P = (\frac{1}{\sqrt{2}}, 0, \frac{1}{\sqrt{2}})$ and $\hat{\epsilon}_S = (0, 1, 0)$ used in the experiment. The quantization axis is along $(0, 0, 1)$.

	$\lvert m_F = -3/2\rangle$	$\lvert m_F = -1/2\rangle$	$\lvert m_F = 1/2\rangle$	$\lvert m_F = 3/2\rangle$
$\langle m_F = -1/2\rvert$	0.27	0	-0.16	0
$\langle m_F = 1/2\rvert$	0	0.16	0	-0.27

Table 3.2: The geometric coupling factors, $\boldsymbol{G}_P^{(3/2)} \cdot \boldsymbol{G}_S^{(3/2)}$ for a two-photon coupling between each magnetic sublevel of the $F = 1/2$ and $F = 3/2$ ground states of ^{6}Li, coupled through the $2P_{3/2}$ excited state manifold (the D2-line), for the polarization vectors, $\hat{\epsilon}_P = (\frac{1}{\sqrt{2}}, 0, \frac{1}{\sqrt{2}})$ and $\hat{\epsilon}_S = (0, 1, 0)$ used in the experiment. The quantization axis is along $(0, 0, 1)$.

Coupling the external degrees of freedom

A critical component of Raman sideband cooling is that the Raman transition can also couple different motional states of the atom. Following reference [135], the two-photon coupling between the internal states, $|S\rangle$, and the external states, $|\boldsymbol{N}\rangle$, is described by the matrix elements

$$\frac{1}{2}\hbar\Omega_c\langle S', \boldsymbol{N}'|\sigma_+ e^{i\boldsymbol{\eta}\cdot(\boldsymbol{a}+\boldsymbol{a}^\dagger)} + \sigma_- e^{-i\boldsymbol{\eta}\cdot(\boldsymbol{a}+\boldsymbol{a}^\dagger)}|S, \boldsymbol{N}\rangle \tag{3.3}$$

The two internal states are coupled with a Rabi frequency of Ω_c in the absence of the motional states, where Ω_c corresponds to that derived in equation 3.1 in the event that these are atomic hyperfine states. These two internal states are coupled by the raising and lowering operators σ_+ and σ_-. Here, we take the external states to be three-dimensional harmonic oscillator eigenstates, described by vectors of motional quantum numbers $\boldsymbol{N}$ and $\boldsymbol{N}'$, with each component corresponding to a

principal axis of the oscillator. The external states are coupled by the operator $e^{i\boldsymbol{\eta}\cdot(\boldsymbol{a}+\boldsymbol{a}^\dagger)} = e^{i\Delta\boldsymbol{k}\cdot\boldsymbol{x}}$. Here, $\Delta\boldsymbol{k}$ is the difference in wavevectors of the Raman beams, $\boldsymbol{a}^\dagger$ and $\boldsymbol{a}$ are vectors of raising and lowering operators for the harmonic oscillator principal axes, and $\boldsymbol{\eta}$ are the Lamb-Dicke parameters for each harmonic oscillator principal axis defined by $\eta_\nu = \Delta k_\nu \sqrt{\hbar/2m\omega_\nu}$, where ν indexes the harmonic oscillator axes and ω_ν are the trap frequencies.

In the limit where $\eta_\nu \ll 1$, the exponential operators in 3.3 can be Taylor expanded giving

$$\begin{aligned}&\frac{1}{2}\hbar\Omega_c\langle S', \boldsymbol{N}'|\sigma_+ e^{i\boldsymbol{\eta}\cdot(\boldsymbol{a}+\boldsymbol{a}^\dagger)} + \sigma_- e^{-i\boldsymbol{\eta}\cdot(\boldsymbol{a}+\boldsymbol{a}^\dagger)}|S, \boldsymbol{N}\rangle \\ &\approx \frac{1}{2}\hbar\Omega_c\langle S', \boldsymbol{N}'|\sigma_+(1 + i\boldsymbol{\eta}\cdot(\boldsymbol{a}+\boldsymbol{a}^\dagger) + \sigma_-(1 - i\boldsymbol{\eta}\cdot(\boldsymbol{a}+\boldsymbol{a}^\dagger))|S, \boldsymbol{N}\rangle.\end{aligned} \tag{3.4}$$

In this expansion to first order, we retain only terms which leave the motional quantum numbers unchanged (carrier), or can add (blue sideband) or remove (red sideband) a single motional quantum. From this expression for the coupling matrix elements we see that the Rabi frequency for driving the carrier transition is Ω_c, and the Rabi frequencies for driving blue sideband or red sideband along trap axis ν starting with N_ν motional quanta are

$$\begin{aligned}\Omega_{RSB} &= \sqrt{N_\nu}\eta_\nu\Omega_c \\ \Omega_{BSB} &= \sqrt{N_\nu + 1}\eta_\nu\Omega_c.\end{aligned} \tag{3.5}$$

Here we formally see that an atom which starts with no motional quanta cannot undergo a red-sideband transition. This provides the dark ground state in Raman sideband cooling. Because the optical pumping light couples to only one of the ground states, the atoms stop scattering photons when they reach the ground state of the trap.

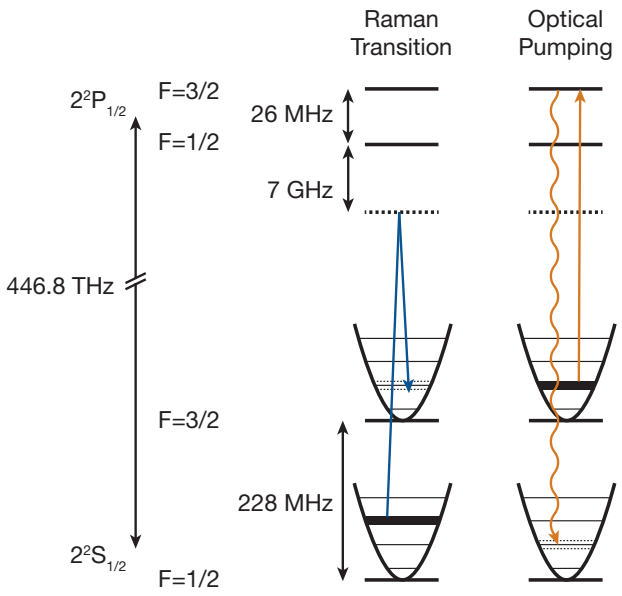

Figure 3.3: A Raman transition drives atoms into the $|2^2S_{1/2}(F = 3/2)\rangle$ hyperfine manifold, removing one vibrational excitation. Atoms are then optically pumped back into the $|2^2S_{1/2}(F = 1/2)\rangle$ manifold while simultaneously switching on the intensifier of an intensified CCD camera to collect the photons scattered during pumping.

3.2 Experimental setup

3.2.1 Sideband Cooling Scheme for ^{6}Li

The level scheme we use for cooling ^{6}Li is depicted in figure 3.3. The cooling is performed at a magnetic field smaller than 20 mG, such that the energy scale of the Zeeman shift is small compared to the Rabi frequencies of the motional transitions. Beginning with atoms in an equal mixture of the two magnetic sublevels of the $|2^2S_{1/2}(F = 1/2)\rangle$ state, a Raman transition drives the atoms into the $|2^2S_{1/2}(F = 3/2)\rangle$ state, coherently removing one vibrational excitation. Because this is a coherent process, no cooling has taken place yet — any atoms which start in the $|2^2S_{1/2}(F = 3/2)\rangle$

state are heated by a vibrational excitation. After the Raman transfer, an optical pumping pulse on the D1-line incoherently polarizes all of the atoms back into the $|2^2S_{1/2}(F = 1/2)\rangle$ state, and one cooling cycle is complete. We collect the photons scattered in the optical pumping process to form an image of the atoms.

To drive the Raman transition we use a single pair of Raman beams with propagation directions chosen such that the momentum transferred has components along all three lattice axes. Figure 3.4 shows the geometry of the optical pumping and Raman beams in the context of the microscope setup. The propagation directions of the Raman beams are $\hat{k}_{R1} = (0.66, 0.7, -0.29)$ and $\hat{k}_{R2} = (-0.69, -0.70, 0.18)$, with the optical pumping beam co-propagating with R2. Zeroing the magnetic bias field ensures that two-photon coupling to all magnetic sublevels is energetically allowed. The Raman beams are linearly polarized in order to avoid effective magnetic fields that could split the magnetic sublevels of the hyperfine manifolds and detune the two-photon transition out of resonance. We found that the cooling works best when the Raman beams have nearly perpendicular polarization, with R2 polarized such that the electric field is in the x-y plane.

While Raman cooling is usually performed with the Raman transition light and optical pumping light turned on continuously and simultaneously, we must use a pulsed scheme to reduce background in the image created by light scattered from R1 and R2. We use a gateable intensified CCD camera (Andor iStar 334T), which is gated off during the Raman transition step to avoid the Raman background light and on during the optical pumping step to collect the scattered photons. A general alternative to using a pulsed scheme would be to drive the Raman transition near a different atomic transition from the one used to do optical pumping and then to filter out the background from the Raman light with an interference filter. A natural choice for alkali atoms would be to drive the Raman transition near to the D1 line and to perform optical pumping on the D2 line. Continuous Raman cooling with D-line spectral filtering is used in the Zwierlein group's ^{40}K experiment [80]. Unfortunately, the technique does not work for ^{6}Li because the D1 and D2 lines are spaced by only 10 GHz and

cannot easily be separated with an interference filter. As discussed in section 3.1.1, the Rabi frequencies for a Raman cooling transition on the lowest motional sideband is given by $\eta_\nu \Omega_c$, where $\eta_\nu = \delta k_\nu x_\nu = (0.33, 0.33, 0.11)$. Here, η_ν is the Lamb-Dicke parameter for the Raman transition, δk_ν is the projection of the difference in the Raman beam wave vectors along the lattice axes, x_ν is the harmonic oscillator length). The two-photon Rabi frequency from the carrier is typically $\Omega_c = 2\pi \times 100\,\text{kHz}$. The optimized pulse duration for the Raman transfer is 10 μs. After the Raman transfer, the atoms are optically pumped back into the the $|2^2S_{1/2}(F = 1/2)\rangle$ dark state at a rate of $\sim 1.1 \times 10^5\ \text{s}^{-1}$ for 20 μs, completing one imaging pulse. This pulse sequence is typically repeated 3.2×10^4 times to form a single image.

The Raman and optical pumping beams are pulsed using TTL-driven RF switches on the signal that drive acousto-optic modulators in the laser table beam paths (figure 3.5), and the camera gate is controlled by TTL. The TTL pulse sequences are generated by a Quantum Composer 8534 pulse generator. We found that it is critical to have a switch AOM in the Raman beam path before the fiber that goes to the experiment table to reduce background light. The experiment table optical setup, laser table setup, and frequency offset lock for the Raman laser system are shown in figures 3.5, 3.6, 3.7.

3.3 Broadening Effects

One curious observation of our Raman cooling scheme is that we find optimal Raman pulse durations that are significantly shorter than the expected $\pi/2$-pulse duration for driving a cooling sideband transition — 12 μs and 36 μs for the radial and vertical lattice directions respectively. One possibility is that shorter pulse durations are optimal because the resulting Fourier-broadening of the Raman pulse covers inhomogeneous broadening of the Raman sideband transition due to a variation in the on-site trap frequency across the atomic sample, and possibly broadening due to finite-temperature

effects. These effects are discussed in the next several paragraphs. The expected Fourier width of $\sim$ 100 kHz agrees nicely with the expected broadening due to inhomogeneity of the on-site trap frequency. We briefly attempted to use Blackman-shaped Raman pulses in the time domain to achieve a flatter Fourier-broadened lineshape, but this did not improve the imaging fidelity.

One source of broadening of the two-photon transition is variation in the on-site trap frequency over the atomic sample. This effect is negligible for the X- and Y-lattices, but not for the Z-lattice which has a much smaller waist and is reflected off of the substrate at a steep angle of incidence. For a lattice formed by interfering, counter-propagating, cylindrically symmetric, Gaussian beams of waist, w_0, the on-site trap frequency, $\omega^{(os)}(r)$,as a function of radius, r, is given by

$$\omega^{(os)}(r) = \omega^{(os)}(0)e^{-r^2/w_0^2}. \tag{3.6}$$

With a typical on-site trap frequency of 1.25 MHz, atomic sample radius of 11 micron, and vertical lattice beam waist of 40 μm, this leads to a 100 kHz spread of on-site trap frequencies over the atomic sample.

An additional source of broadening during the cooling process is anharmonicity of the individual lattice wells. As shown in section 2.2.1, the anharmonic term for a $\cos^2(x)$ lattice potential decreases the energy of each harmonic oscillator level by $\delta E_{anh} = -(13/12 + n)E_r$, where n is the principal quantum number (indexed from zero), and E_r is the lattice recoil energy. The lattice recoil energies are $E_r^{(\mathrm{X})} = E_r^{(\mathrm{Y})} = 25.6$ kHz and $E_r^{(\mathrm{Z})} = 29.0$ kHz for the radial and vertical lattices, respectively. With two-photon Rabi frequencies of $\sim$40 kHz on the vibrational sidebands, we would expect to power broaden over only the first 2-3 vibrational transitions before the anharmonicity shifts the atoms out of the two-photon resonance. We experimented both with sweeping the two-photon detuning, increasing the two-photon Rabi frequencies, and shaping the Raman pulses in real time to broaden the two-photon resonance and did not find an improvement in the imaging fidelity. We

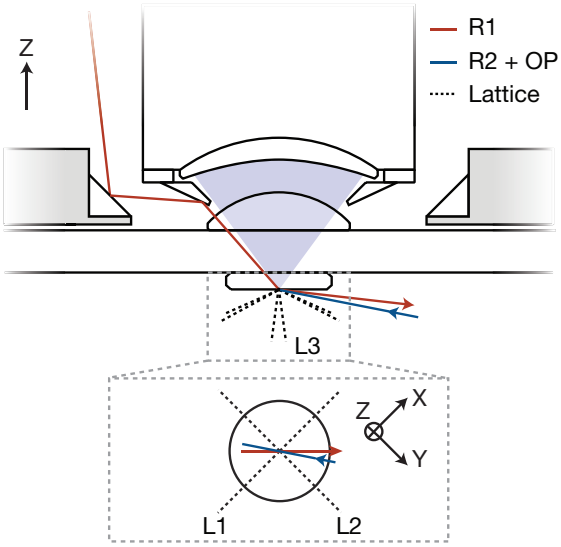

Figure 3.4: R1 and R2 denote our Raman beams, and OP the optical pumping light which co-propagates with R2. L1 and L2 are additionally retroreflected out of the schematic to create a 3D lattice as described in section 1.3.3. L3 forms a lattice along $\hat{z}$, providing additional confinement during imaging. L1, L2, and L3 have waists of approximately $80\ \mu$m, $80\ \mu$m, and $40\ \mu$m, respectively. The beam propagation directions have to be arranged such that the vector of momentum transfer from a Raman transition has components along each lattice direction.

do, however, find that the optimal two-photon detuning for Raman imaging is red-detuned from the expected frequency for the first blue sideband transition (see section 3.6).

The single-photon optical pumping resonance can be broadened by a differential AC stark shift from the optical lattice between the ground and excited electronic states. The vertical lattice dominates this effect because it has the smallest waist. Luckily, the AC polarizabilities for the $2S_{1/2}$ and the $2P_{1/2}$ states of ^{6}Li are similar — 271 a.u. and 202 a.u., respectively [136]. This results in a 2 MHz broadening of the pump resonance over a typical atomic sample, smaller than the natural linewidth of 6 MHz. Broadening of the optical pumping resonance due to a differential AC polarizability is a significant effect when performing Raman sideband cooling on ^{40}K [80].

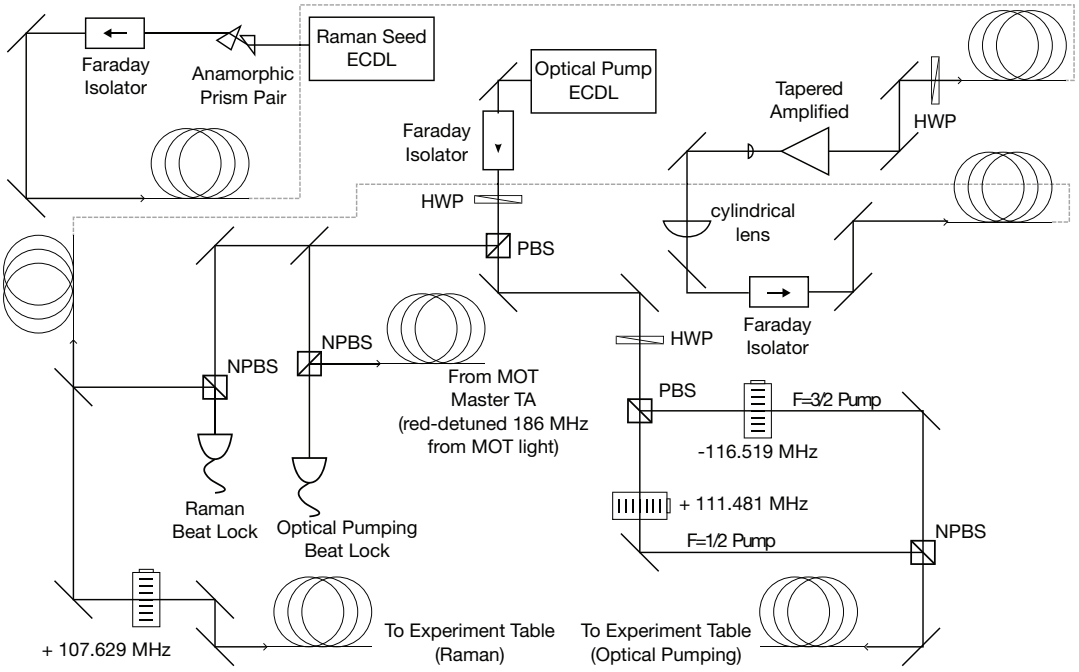

Figure 3.5: Schematic of laser table Raman cooling setup.

3.4 Atom detection algorithm

We are primarily interested in determining whether each lattice site is occupied from the site-resolved images. This determination is complicated by the fact that the extent of the PSF is comparable to the lattice spacing. The problem is considerably simplified because we can independently determine the PSF (figure 1.1c) and the geometry of the underlying lattice. In reference [81], we described a least-squares fitting method to determine the PSF amplitudes on each lattice site. Since then, we have found that the deconvolution-based approach described below gives the same results as directly fitting the amplitudes of PSFs on each site of the lattice, but requires much less computation time.

With our setup, the atoms are sufficiently resolved that the underlying grid structure from the lattice can be clearly seen even in regions where every site is occupied. As a result, taking the Fourier transform of an image allows us to completely determine the lattice geometry, and thus the location

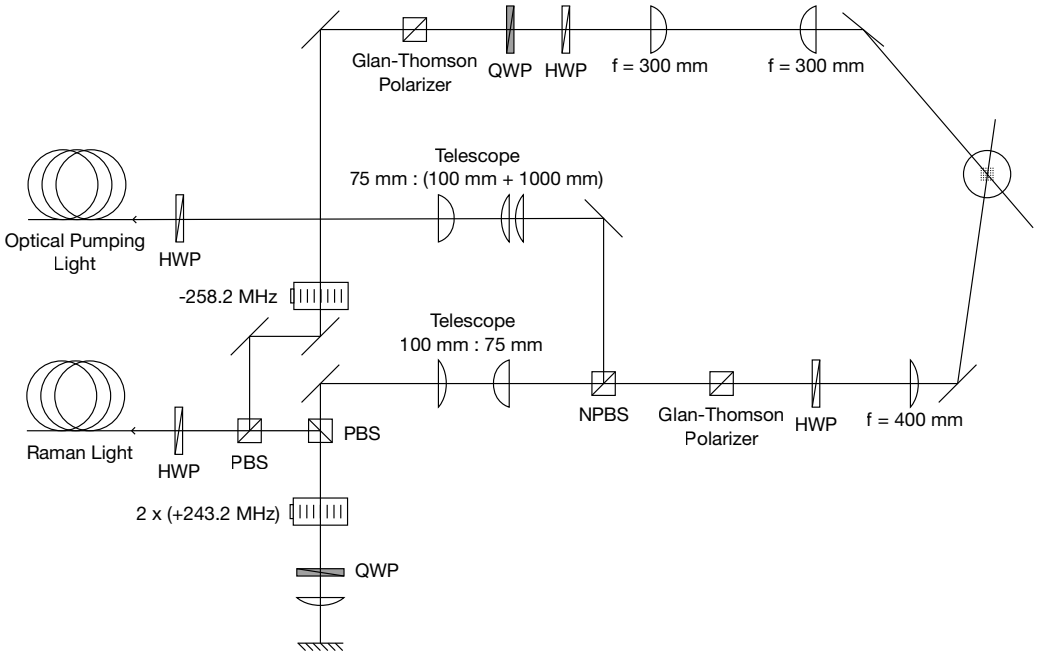

Figure 3.6: Schematic of experiment table Raman cooling setup.

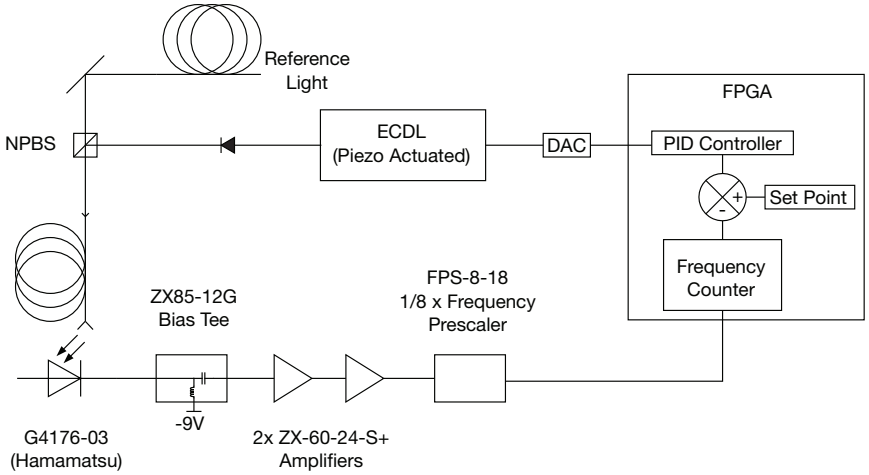

Figure 3.7: Schematic of beat (frequency-offset) lock used to lock the frequency of the Raman and optical pumping lasers relative to the laser used for our magneto-optical trap.

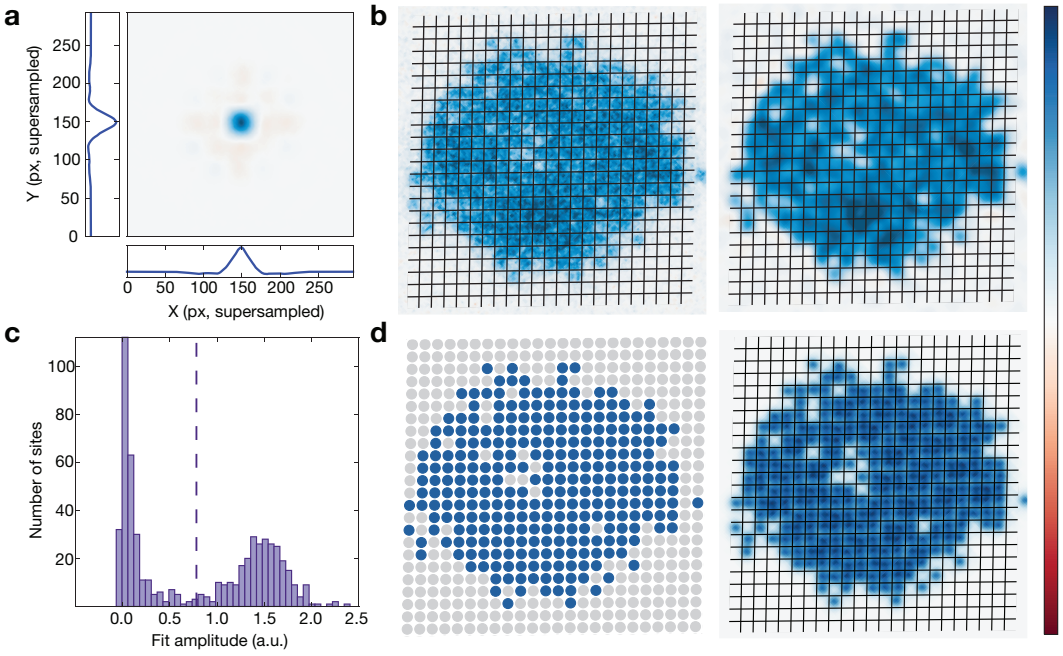

Figure 3.8: A kernel used for our atom-detection algorithm is shown in (a), with the plot margins showing cuts through the kernel. Panel b shows the raw image followed by an image after convolution with the kernel, with a histogram of the resulting amplitudes on each lattice site shown in (c). After binarizing the amplitudes according to the threshold shown by the dotted line in (c) we are able to reconstruct the lattice occupation (d). The right image in (d) is an ideal image constructed by placing PSFs with equal amplitudes on each occupied site.

of every site on the lattice. The amplitude of the Fourier transform reveals a grid of peaks corresponding to the reciprocal lattice vectors. The phase of the Fourier transform at each of these peaks gives the overall geometric offset of the lattice.

The algorithm that we use relies on a kernel, defined such that the overlap of the kernel $k_{ij}(\boldsymbol{r})$ on site (i, j) with a PSF $w_{l,m}$ on site (l, m) is given by

$$\int k_{i,j}(\boldsymbol{r}) w_{l,m}(\boldsymbol{r}) d\boldsymbol{r} = \delta_{i,l}\delta_{j,m}. \tag{3.7}$$

Due to negligible distortion across the field of view of our imaging system, the PSFs on each site are identical, and so $w_{i,j} = w(\boldsymbol{r} - \boldsymbol{r_{i,j}})$, where $w(\boldsymbol{r})$ is the measured PSF. We can write the kernel, $k_{i,j}(\boldsymbol{r})$, as a linear combination of point spread functions, $w_{l,m}(\boldsymbol{r})$, and so it also follows that $k_{i,j} = k(\boldsymbol{r} - \boldsymbol{r_{i,j}})$.

Because the PSF decays almost completely over just two lattice sites, we can approximate the kernel as a linear combination of point spread functions in a five-by-five site region:

$$k_{0,0}(\boldsymbol{r}) = \sum_{i,j \in [-2,2]} b_{ij} w_{ij}(\boldsymbol{r}) \tag{3.8}$$

We can then find the b_{ij} by numerically optimizing to satisfy the kernel definition, 3.7, for $k_{0,0}(\boldsymbol{r})$ including only PSFs within the truncated five-by-five region. The kernel obtained by this process is shown in figure 3.8a.

By definition, placing the kernel on any lattice site and computing its overlap integral with the image gives the amplitude of that site. To determine the amplitude of every site, we simply take the convolution of the kernel with the image (figure 3.8b). The site amplitudes are then simply the values of the convolution result at the center of each lattice site. A histogram of the amplitudes reveals a bimodal distribution with the two peaks corresponding to empty and filled lattice sites. By

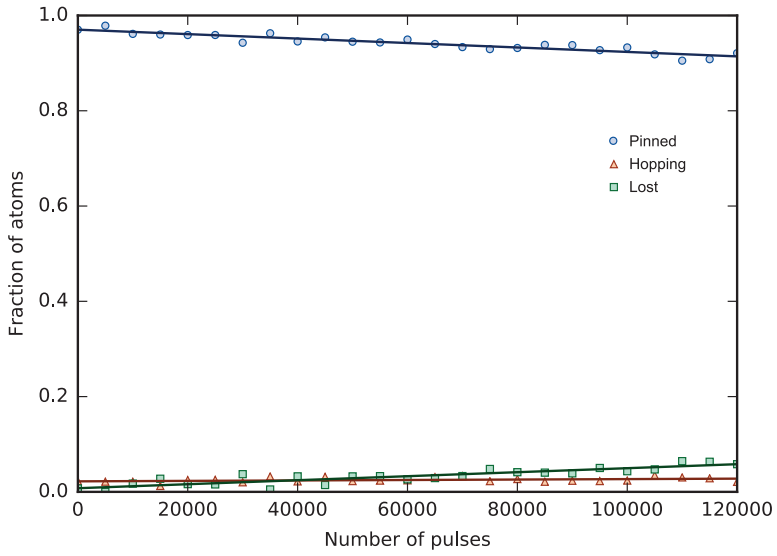

Figure 3.9: We determine the Raman imaging fidelity by taking two subsequent images of the same atomic cloud and looking at the fraction of atoms that are pinned, hop, and are lost from each lattice site between the first and second image. Additional imaging pulses are applied between the images, with the camera gated off. The number of additional pulses is varied and the fraction of atoms that are pinned, hop and are list are fit to a line to determine a slope and extract the expected fractions for a single imaging pulse.

applying a binarization threshold to the amplitudes we determine which sites are occupied (figure 3.8d).

3.4.1 Wiener Deconvolution

Between our observations of band and Mott insulators (chapter four) and our observations of spin correlations (chapter five) we discovered that a Wiener deconvolution gave better results than the kernel convolution procedure described above. The Wiener deconvolution is implemented using the scikit-image toolbox [137]. All other steps of the binarization procedure remain unchanged.

3.5 Imaging Fidelity

To study atom hopping and loss due to the imaging, we take two images with 3.2×10^4 Raman imaging pulses each and apply a varying number of Raman imaging pulses in between them. By comparing the reconstructed site occupations in each frame, we determine the fraction of atoms that stay pinned to their sites, hop between sites, and are lost from the image (f_p, f_h, and f_l). Loss can be caused by atoms leaving the region of analysis, hopping along $\hat{z}$, undergoing light-assisted collisions after an in-plane hopping event onto a previously occupied site, or leaving the trap. Figure 3.9 shows f_p, f_h, and f_l versus the number of pulses applied between frames for optimized imaging parameters. Each data point corresponds to a single shot. By applying a linear fit to these data, we can determine rates that we use to get the expected pinned, hopping, and lost fractions for a single image with 3.2×10^4 pulses. The fitted slopes imply $f_\mathrm{p} = 99.25(6)\%$, $f_\mathrm{h} = 0.08(4)\%$, and $f_\mathrm{l} = 0.67(7)\%$ for a single image with 3.2×10^4 imaging pulses. A negative lost fraction corresponds to atoms entering the region of analysis. In regions with unity filling, each hopping event will cause the loss of two atoms due to light-assisted collisions on doubly occupied sites.

As described in [56, 138], the thermal hopping during fluorescence imaging can be modeled by an Arrhenius process, where the probability of hopping during a scattering event is given by the ratio of the temperature of the atoms to an activation energy, in this case the depth of the lattice. The Arrhenius model assumes a Maxwell-Boltzmann distribution. In the images taken to produce figure 3.9 we collected approximately 270 photons per atom. At a collection efficiency of approximately 9.4%, incorporating the quantum efficiency of the camera, and the collection efficiency of the imaging system, this means that the atoms scatter approximately 2900 photons, or 0.09 photons per imaging pulse. Taking a hopping rate of 0.75% per image, the probability of a hopping event per scattered photon, P_s, is then 2.6×10^{-6}. According to the Arrhenius law, the temperature, for

our lattice depth of $V_0 = 16$ MHz is then the resulting temperature estimate

$$T = -\frac{V_0}{k_B \log P_s} \sim 140\ \mu\text{K}. \tag{3.9}$$

3.6 Optimization of Raman imaging parameters

Because Raman sideband cooling is a dark state cooling scheme, the optimal parameters for high-fidelity imaging are not necessarily the parameters which yield the coldest temperature. Furthermore, the effects of inhomogeneity, anharmonicity, differential AC stark shifts, and finite trap depth will also cause the optimal imaging parameters to deviate from what is expected for a three-level atom in a harmonic trap. These effects are not fully understood in our experiment, largely because the Raman imaging scheme provides sufficient imaging fidelity to enable many-body experiments that we have been more interested in than these details. In this section, I present data taken to optimize our Raman sideband imaging, without a full understanding of the trends (though with plenty of speculation). The primary audience in mind are future debuggers and builders of single-site imaging systems with ^{6}Li.

In optimizing the imaging, we care about collecting enough photons to accurately determine whether each site is occupied, while minimizing the fraction of atoms that hop or are lost (or maximizing the fraction of atoms that remain pinned to their initial sites). Varying one of the imaging parameters may lead to a lower pinned fraction but an increased scattering rate. Decreasing the number of pulses to collect only the required amount of light may then yield a larger pinned fraction. In the limit of small loss and hopping fractions, where the loss is linear in imaging time, and assuming that the number of photons scattered is also linear in imaging time, the parameter to optimize is the number of collected photons per atom multiplied by the pinned fraction. In the data presented in this chapter we take two subsequent images of the same atom cloud and compute the pinned

fraction, as in the data presented in figure 3.9. Each image is taken with 9.6×10^4 imaging pulses and between the two images there are an additional 3.2×10^5 pulses to enhance the loss signal. By dividing the total number of photons collected on the camera, including the intensifier amplification, by the number of atoms in each image, we can determine the number of photons collected from each atom. Due to the finite quantum efficiency of the photocathode and the collection efficiency of the imaging system, we collect approximately 9.5% of the photons scattered. The number of photons collected per atom is then multiplied by the pinned fraction to provide a figure of merit for optimization.

Figure 3.10 shows the optimization of the power and duration of the pulses used to make the Raman transition. The power of the pump and stokes beams are varied in the same proportion by varying the RF power into the switch AOM shown in figure 3.5. For each power used in the measurement, the Rabi frequency on the carrier transition was measured by fitting the Rabi oscillations of the population in the $F = 3/2$ state. The largest Rabi frequency corresponds to the largest power available in the setup at the time of the measurement. The imaging seems optimal for the largest available power, likely because the higher Rabi frequencies broaden the two-photon transition and counteract the aforementioned inhomogeneities.

Figure 3.11 shows the optimization of the pump power and duration. The power is actuated by varying the RF power into a switch AOM. For each power the rate of decay out of the $F = 3/2$ state is measured by preparing atoms in that state with a microwave pulse and then applying a pulse of pump light with varying duration and fitting an exponential. The results of this calibration are noted in the legend. Here we see that, although the maximum number of scattered photons per atom is roughly the same for each pumping rate, there is a clear optimum in the figure of merit at a pumping rate of $0.06\ \mu s^{-1}$, with a sharp decay at higher powers. The optimal rate is still far from the saturated value of $19\ \mu s^{-1}$ for the 6 MHz wide optical transition.

Figure 3.12 shows the optimization of the two-photon detuning, pump detuning, and the on-site

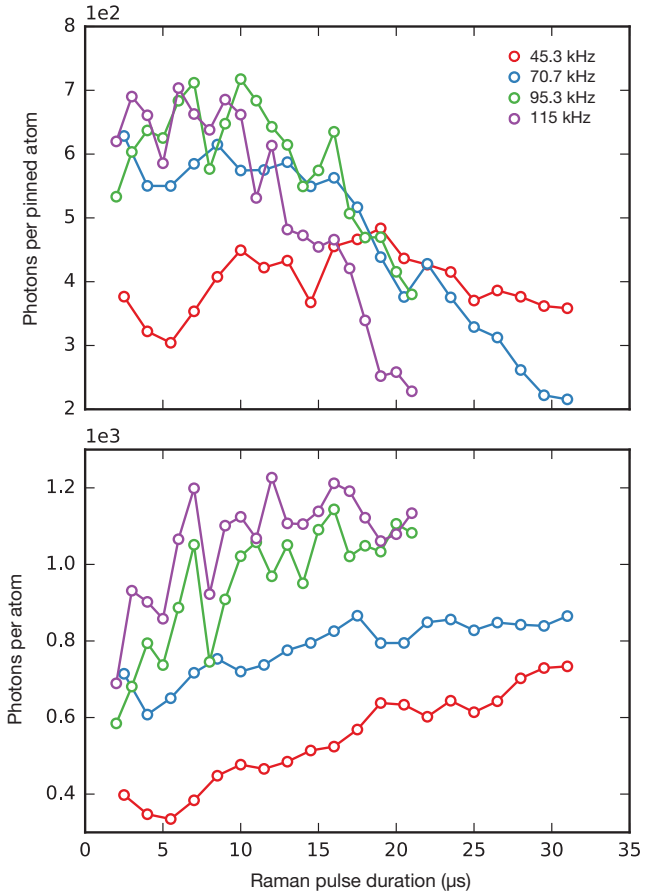

Figure 3.10: The duration of each Raman transition pulse is varied for different Raman carrier Rabi frequencies (Raman beam powers). The Rabi frequencies are calibrated by fitting the Rabi oscillations in the population of the $F = 3/2$ state in the presence of the Raman light. The figure of merit for optimization is plotted on top and, for comparison, the number of photons per atom is plotted on the bottom.

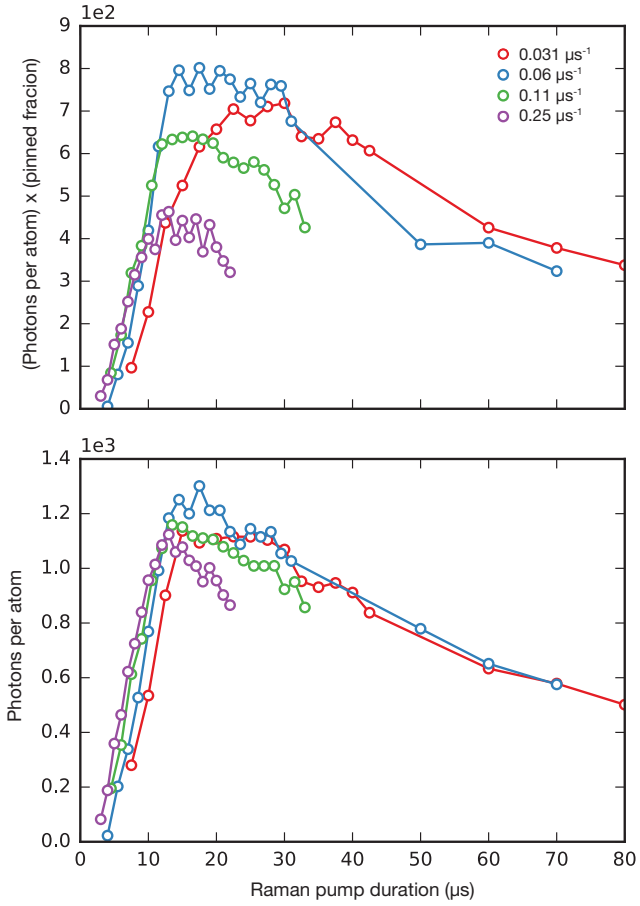

Figure 3.11: The duration of each optical pumping pulse is varied for different optical pumping rates (pump powers). The pumping rates are calibrated by fitting the exponential decay of atoms prepared in the $F = 3/2$ ground state in the presence of the pumping light.

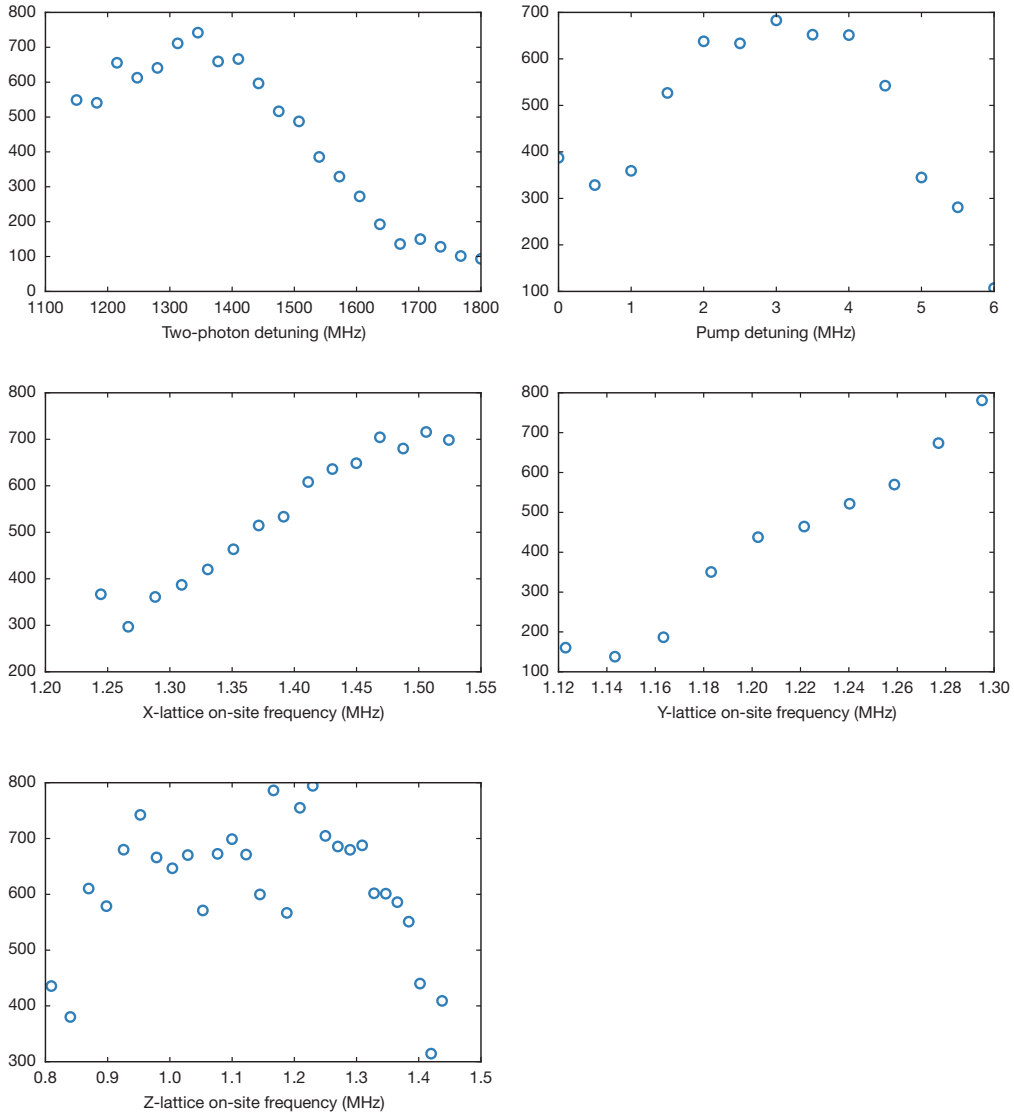

Figure 3.12: Optimization of Raman imaging parameters with respect to the number of collected photons from each atom which remains on its site, as described in the text.

trap frequencies for each optical lattice beam. The trap frequencies are varied with the power of the corresponding lattice beam and calibrated with lattice modulation spectroscopy. The main deviation from expectations in this set of data is that the optimal two-photon detuning (taken at optimized values for each of the on-site frequencies) looks to be smaller than the optimal trap frequency for the X-lattice. The same may be true of the Y-lattice, but we lack the available power to go to larger trap frequencies. There are several possible explanations for this. Larger lattice powers also create a larger barrier to thermal hopping and thus lower hopping rates for a fixed steady-state temperature. Consistent with this speculation, we have found that it is not advantageous to reduce the two-photon detuning and re-optimize the lattice powers, sacrificing depth. An additional possible cause of the red-shift of the optimal two-photon detuning may be anharmonicity of the on-site potential. The effect of anharmonicity is to red shift the sideband transitions for higher motional levels, and so a red-detuned two-photon transition may provide cooling for a larger range of motional eigenstates. The data in 3.12 also shows that we are limited by the available powers in the X- and Y-lattices.

4

Site-resolved imaging of a fermionic Mott insulator

As a first implementation of the imaging technique described in the previous chapter, we have performed site-resolved measurements of the single-particle occupation in a Hubbard regime optical lattice. By varying the interaction parameter, U, we were able to observe Mott insulators, band insulators, and metallic states. Because the overall harmonic confinement of the lattice leads to a variation in the local chemical potential, μ, across the atomic sample, we observe the coexistence of multiple states in the trap. By comparing our observations to a high-temperature series expansion of the Hubbard model, we are able to determine thermodynamic parameters such as global chemical

potential, entropy, and temperature of the cloud from a single shot. We found trap-averaged entropies as low as 1.0 k_B for a Mott-insulating (MI) state, and entropies as low as 0.5 k_B for a band-insulating (BI) state. The following chapter describes these observations in detail, repeating much of the material published in reference [85], with less compressed explanations wherever it seems they might be beneficial to the reader.

The superfluid to Mott insulator transition in bosonic systems has been studied extensively by experiments using ultracold atoms in optical lattices. The first observation of the superfluid to Mott insulator transition in a cold atom system by Greiner, et al. [17] was done rather indirectly, by observing the disappearance and revival of superfluid peaks as the interaction parameter was ramped to the Mott insulating regime and back. Later, the wedding cake structure created by Mott insulating regions with different site occupations was observed using clock shifts in an optical lattice [139], and also by using spatially-selective spin-changing collisions to induce spin-changing collisions [140]. With the development of site-resolved imaging [58], this wedding cake structure could be observed directly [58, 59]. In the intervening time a number of studies of the phase transition in one, two and three dimensions have been carried out, many of which can be found in the review paper by Bloch, et al. [141]. In the site-resolved imaging experiments Mott insulators have been used, in conjuction with atom-resolved manipulation techniques [75], to deterministically prepare small systems with uniform filling, enabling studies of strongly correlated quantum walks [76] and the measurement of entanglement entropy in an itinerant many-body system [77]. Single-site resolution also enables the extraction of non-local order parameters such as string order [142] and allows studies of strongly-correlated dynamics in optical lattices [76, 68, 65].

The extension of site-resolved imaging to fermionic atoms furthers the exploration of the rich phase diagram of the Hubbard model, thought to describe a variety of strongly correlated quantum-mechanical phenomena, including high-temperature superconductivity [6]. This exploration is already underway, with the first observations of fermionic Mott insulators and band insulators in 2008 using conventional

imaging techniques [38, 39]. Measurements of antiferromagnetic correlations in Hubbard systems have also been performed in a variety of lattice geometries [43, 44, 45]. This is the first work that reports site-resolved measurements of a strongly interacting Fermi-lattice system. The ability to measure the site occupation at the level of single lattice sites allows us to directly measure the variance in the site occupancy. In addition, it allows us to put an upper bound on the charge entropy of the gas. Finally, the ability to measure correlations at the single-site level allows us to move beyond trap-averaged measurements to local measurements of antiferromagnetic correlations as described in the next chapter.

A fermionic MI is a prime example of a strongly-interaction many-body state. In a fermionic MI repulsive interactions generate insulating behavior in a half-filled energy band, which in the absence of interactions would be metallic. This behavior is well described by the Hubbard model, which includes only an on-site interaction term, parametrized by U, and a kinetic energy (tunneling) term parametrized by t. In a finite-size system a density-order crossover from a metalic to an MI state occurs as the ratio U/t is increased. For an infinite system the metallic state has a gapless excitation spectrum, is compressible, and has a large variance in the site occupation, whereas a Mott insulator has an excitation spectrum gapped by U, is incompressible, and has vanishing variance in the site occupation. Observing a Mott insulator requires temperatures much lower than the energy gap. Because, for cold atoms in Hubbard-regime optical lattices, this energy scale is generally larger than the magnetic exchange energy scale, $\sim t^2/U$, MI behavior can occur at a temperature scale where spin-ordering is absent.

At higher fillings and for interaction energies comparable to the kinetic energy scale, an incompressible band insulator (BI) of doublons appears because the Pauli exclusion principle prevents more than one atom of the same spin from occupying the same lattice site if they are in the same band of the lattice. Similar BI behavior can also be observed in a non-interacting system made up of fermions in a single spin state, as has been done recently in the Munich fermionic single-site experiment

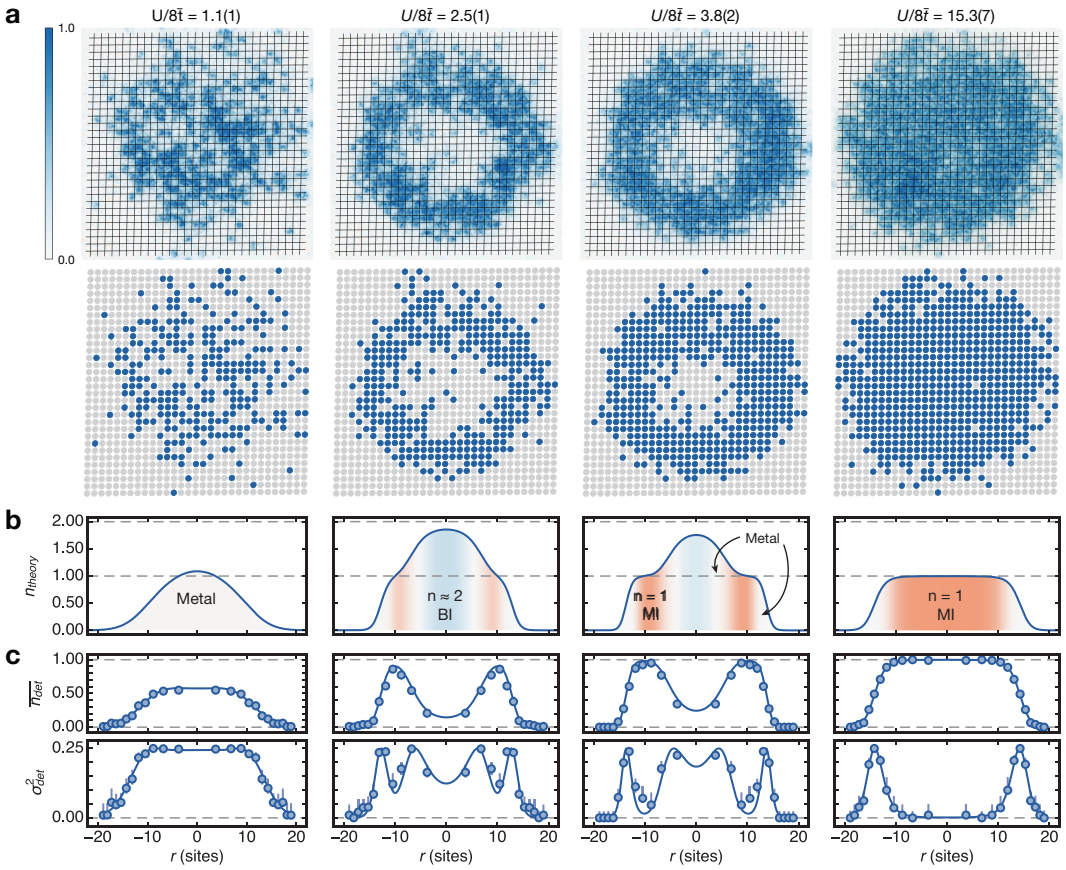

Figure 4.1: (**a**) Single experimental images of the atoms in the square lattice are shown for varying interaction, $U/8\bar{t}$, along with the extraced site occupation (second row). (**b**) Calculated full density profiles for the experimental parameters in panel a, obtained from the fits to the experimental data. Depending on the interaction, we observe MI, BI, and metallic phases. The MI appears for strong interactions as an extended region with filling $n_{\text{theory}} = 1$. In the BI, the filling approaches 2. Metallic regions connect the different insulating states, where the filling changes from one to two. (**c**) By applying azimuthal averages to the corresponding single images, we obtain radial profiles (mirrored at $r = 0$) for the detected occupation, $\overline{n_{\text{det}}}$, and variance, σ^2_{det}. The variance is strongly reduced in the insulating phases. The radial occupation profiles were fit using a high-temperature series expansion of the single-band Hubbard model, with temperature and global chemical potential as free parameters (solid lines). The fits give temperatures $k_B T/U = 1.6(3), 0.22(3), 0.12(2)$, and $0.050(7)$ from left to right. The large values of temperature and entropy as $U/8\bar{t} = 1.1$ may be caused by non-adiabatic loading of the lattice at small interactions. Error bars are computed from a sampled Bernoulli distribution as described in the text.

[83]. This behavior is is in contrast to the bosonic case where the absence of the Pauli exclusion principle allows any number of atoms to occupy a single site, and a lobe structure of MI states with different occupation numbers appears [139, 61, 59]. The starting point of the experiment is a low-temperature, two-dimensional gas of fermionic ^{6}Li atoms with repulsive interactions in an equal mixture of the two lowest hyperfine ground states. After the preparation and cooling of the cloud, described in section 1.4, we set the s-wave scattering length to values between $a = 37\,a_0 - 515\,a_0$ by adjusting a magnetic bias field in the vicinity of the Feshbach resonance located at 832 G, where a_0 denotes the Bohr radius [103]. We then load the atoms into a square optical lattice using a 30 ms linear ramp of the laser beam powers. The system is well described by a single-band two-dimensional hubbard model on a square lattice with nearest-neighbor tunneling $t_x/h = 0.279(10)$ kHz and $t_y/h = 0.133(4)$ kHz along the two lattice directions with a corresponding bandwidth, $8\bar{t}/h = 1.65(7)$ kHz, and interaction, $U/h = 1.81(3)$ to $25.2(5)$ kHz. We detect the many-body state of the system by measuring the occupation of each lattice site with single-site resolution, as described in chapter 3.

We directly observe the metal-to-MI transition on a site-resolved level. Single images show a drastic change in the occupation distribution when increasing the interaction at constant atom number (figure 4.1). The interaction is parametrized by the ratio $U/8\bar{t}$, where $8\bar{t}$ is the bandwidth of the lattice and therefore the kinetic energy of an atom that is localized to a single lattice site. For the weakest interactions [$U/8\bar{t} = 1.1(1)$], we observe a purely metallic state with a large occupation variance over the entire cloud. The maximum detected value for the variance was 0.25, which is consistent with equal occupation probabilities of all four possible states per lattice site. The occupation decreases gradually for larger distances from the center because of the underlying harmonic confinement. In contrast, for the strongest interactions [$U/8\bar{t} = 1.1(1)$], we observed a large half-filled MI region containing about 400 atoms. The variance in occupation in the center of the MI region is suppressed to values below 0.02, with thermal excitations appearing as an increased

variance in the occupation at the edge of the cloud.

The underlying harmonic trap causes a spatially varying chemical potential, which can lead to the appearance of different phases within the trap. The interplay of the band width, $8\bar{t}$, the interaction energy, U, and the global chemical potential, μ determines the appearance of the metallic, BI, and MI phases in the trap, as described in figure 4.2. In this schematic picture the single-particle band of the lattice is split by the interaction into two bands separated by an energy U. When a site is doubly occupied, the on-site energy is raised by an energy U, and this is schematically shown by the second atom occupying in the higher U-band. The lattice and harmonic potential are represented by the bent sinusoid with the troughs denoting lattice sites in real-space. The amplitude of sinusoid *does not* denote the potential depth of the lattice but the bandwidth, $8\bar{t}$, — a possible source of confusion. The global chemical potential, μ, determines the energy to which atoms fill the lattice. In this illustration the temperature is much smaller than the interaction energy, but comparable to the bandwidth, resulting in the formation of a metal whenever the chemical potential falls in the middle of the band. For intermediate interactions, where $\mu > U$, a wedding cake structure forms, with a band insulator in the center of the cloud, surrounded by a metallic ring with one or two atoms per site and a large variance in occupation number, then a Mott insulator with one atom per site and suppressed variance in the occupation number, and finally another metallic ring with zero to one atom per site. This situation describes the data at $U/8\bar{t} = 2.5(1)$ and $U/8\bar{t} = 3.8(2)$ in figure 4.1, and is depicted schematically in figure 4.2a. For increased interaction energy, such that the chemical potential is never larger than the top of the higher U-band but instead passes through it ($\mu \sim U$, figure 4.2b), the center of the cloud becomes metallic and is surrounded by a Mott insulator and then a metal where the chemical potential crosses through the lower U-band. Finally, when the chemical potential lies below the higher U-band but well above the lower one ($8\bar{t} < \mu < U$, figure 4.2c), the center of the cloud is a Mott insulator surrounded by a metallic ring. This describes the behavior of the data where $U/8\bar{t} = 15.3(7)$ in figure 4.1.

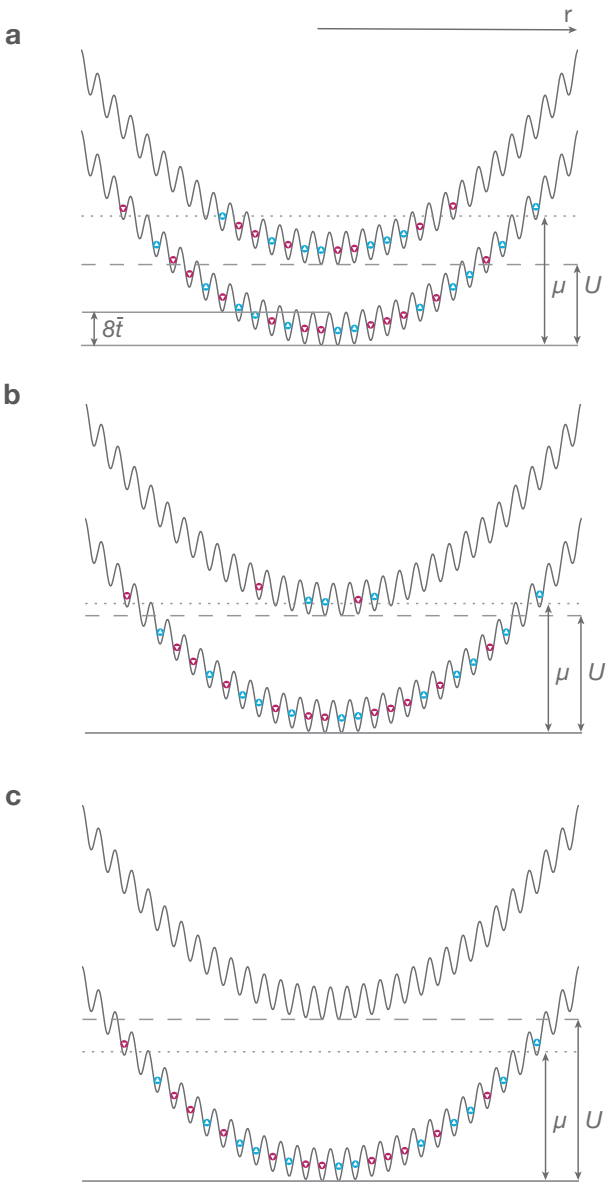

Figure 4.2: A schematic illustration of the cross over from a BI to a metal to an MI as the interaction parameter is increased, as well as the coexistence of multiple phases in the harmonic trap. This can be understood by considering the interaction to split the single-particle into two bands, with doubly occupied sites having one atom in the higher U-band. The amplitude of the sinusoid denoting the lattice indicates the bandwidth, not the lattice depth, and the bending of the sinusoid illustrates the underlying harmonic trap.

As previously mentioned, an essential requirement for a MI is a temperature well below the energy gap $k_B T \ll U$. We are able to measure the temperature of the atoms in the lattice by comparing the detected radial occupation, $\overline{n_{\text{det}}}(r)$, and variance, $\sigma^2(r)$, profiles obtained from single images to theoretical calculations based on a second-order high-temperature series expansion of the Fermi-Hubbard model (section 2.3.2). In all figures the error bars on the mean and variance profiles are 68% Clopper-pearson confidence intervals. The effect of the harmonic trap is described with a local density approximation, where the chemical potential varies locally [143]. The temperature and chemical potential are obtained from a fit to the detected density distribution $\overline{n_{\text{det}}}(r)$, and all other parameters are calibrated independently (section 1.5). We find excellent agreement with theory for all interactions and measure temperatures as low as $k_B T/U = 0.05$ for the largest interaction, corresponding to an average entropy per particle of $S/N = 1.15\ \text{k}_\text{B}$. For weaker interactions, we find entropies as low as $S/N = 1.15\ \text{k}_\text{B}$. For weaker interactions we find entropies as low as $S/N = 0.99\ \text{k}_\text{B}$. When repeating the experiment with the same parameters we find a shot-to-shot variance in entropy consistent with fit errors. The agreement with theory shows that the entire system is well described by a thermally equilibrated state, and the underlying trapping potential is well described by a harmonic trap.

We can use the fitted global chemical potential and our knowledge of the trap geometry to determine the local chemical potential at each radius in the trap. Using this information, we can obtain from each radial profile a scan along a single line in the $(\mu/U, k_B T/U)$ phase diagram of the Hubbard model, as shown in figure 4.3. The MI is identified by an extended region in μ/U, with constant occupation $\overline{n_{\text{det}}} = 1$ and a strongly reduced variance. Because in this regime, where nearly all lattice sites are occupied by a single atom, the total and detected fillings are approximately equal (see figure 4.1b, right panel), the compressibility, κ, in the range just below half-filling ($\mu < U/2$) can be obtained from $\kappa = \partial n_{\text{det}}/\partial\mu$, which is small in the MI region. The metallic regions are signaled by an enhanced compressibility, with a peak in the variance distribution. The width of the metallic

peak in variance is determined by the temperature and is smallest for the largest interactions, since $k_B T/U$ decreases for increasing interactions in the experiment.

Two effects contribute to reducing the filling from one particle per site in the MI region — the finite temperature of the gas and the non-unity imaging fidelity. We can determine a lower bound on the filling by averaging over 50 images, resulting in $\overline{n_{\text{det}}} = 96.5(2)\%$. Our imaging fidelity is $97.5(3)\%$, and so it contributes significantly to the reduced filling.

The measured average filling gives a direct upper bound in the charge entropy (i.e., the entropy involving density excitations of the atomic cloud). The charge entropy per site is given by the expression

$$s_i^{\text{charge}} = -k_B \sum_j p_j \ln(p_j). \tag{4.1}$$

Here p_j denotes the occupation probability in the grand-canonical ensemble of each possible charge state, j, on lattice site i. There are three possible charge states — a doubly occupied site (p_d), a hole or empty site (p_h), and a single atom (p_s). Because our imaging does not distinguish between a hole and a doublon, without resorting to the high temperature series fits, we can only provide an upper or lower bound on the charge entropy. The upper bound is obtained by assuming that the contributions of holes and doubly occupied sites to the probability of detecting an empty site ($1 - \overline{n_{det}}$) are equal, and the lower bound is obtained by assuming that either holes or doubly occupied sites contribute entirely to the probability of detecting an empty site. The measured average filling of 96.5% then gives an upper bound on the charge entropy of 0.175 k_B.

Because the particles are in a mixture of two different spin states, the total entropy also contains a contribution from the spin degree of freedom. Because our imaging is not spin-sensitive, we are unable to measure this entropy directly. We are, however, able to determine the spin-entropy from the fitted high-temperature series model. From the fitted temperatures we calculate the total entropy per site as a function of μ/U for the different interaction (figure 4.3b inset). In the MI

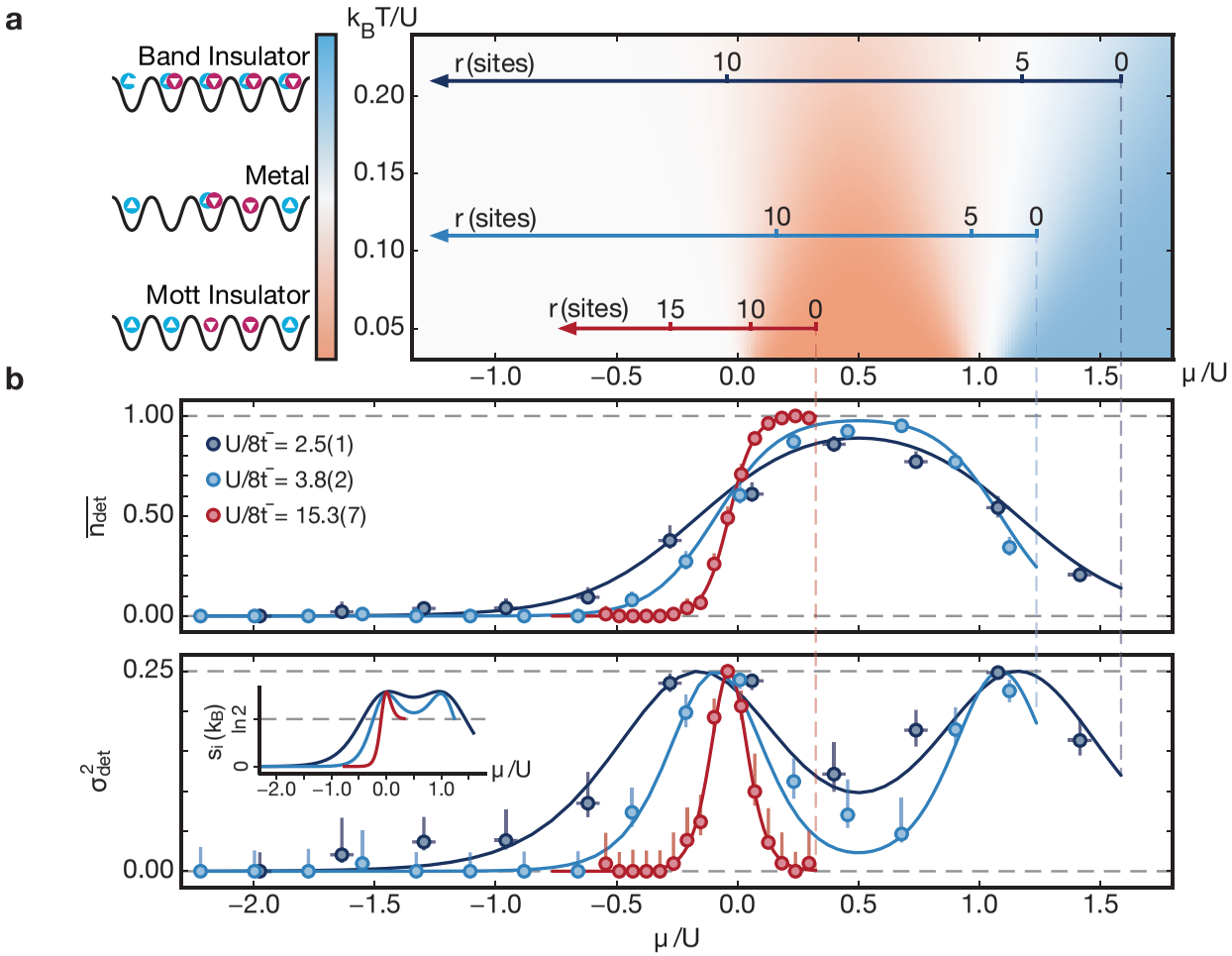

Figure 4.3: (**a**) A schematic of the $(\mu/U, k_B T/U)$ phase diagram of the Hubbard model at $U \gg \bar{t}$, which is the relevant regime for each of the three data sets shown. The intensity of the shading reflects the normalized variance of the site occupation, and the colors distinguish between the MI and BI regimes. The arrows denote radial cuts through the trap for different interactions corresponding to the profiles shown in panel b. (**b**) Detected site occupation and variance versus chemical potential, obtained from the radial profiles in figure 4.1, with fits to a high-temperature series expansion as solid lines. The distributions are symmetric around $\mu = U/2$ (half-filling) from particle-hole symmetry. Profiles of the calculated local entropy per site, s_i are shown in the inset in the bottom left.

region we find $s_i = 0.70(1)\ \mathrm{k_B}$, consistent with $s_i = k_B \ln 2$, which corresponds to the entropy of a paramagnetic MI. In the BI region the spin entropy is suppressed compared to the MI region because whenever there is a doubly occupied site the spin entropy contribution from that site is zero. In the BI, $78(1)\%$ of the lattice sites are doubly occupied. We can estimate the charge entropy from the measured density of singly occupied sites, assuming that in the band insulator every measured empty site is a doublon. This estimate gives an entropy of $0.53(2)\ \mathrm{k_B}$, in good agreement with the calculated value of $0.5(1)\ \mathrm{k_B}$ from the theory fit. By comparing the fitted entropy and density profiles of the clouds after loading the lattice to the calculated entropy profile for a cloud with the same total entropy in the trap before the lattice is loaded, we see that there must be significant mass and entropy transport as the cloud re-equilibrates during lattice loading. This potentially bodes well for generating phases of matter that require even lower local entropies using entropy redistribution schemes [144, 145, 146].

Accurate experimental studies of the low-temperature Hubbard model generally require large system sizes. By adjusting the evaporation we can control the size of the MI with detected total atom numbers (without doublons) ranging from $N = 145$ to $N = 718$ (figure 4.5), maintaining average occupation values in the center of the cloud greater than 0.92. Repeating the same experiment many times, we found that the atom number is highly reproducible, with the standard deviation always $< 5\%$ of the mean atom number.

While for temperatures $k_B T \ll U$ a large MI with a sharp falloff in occupation distribution (or a narrow peak in occupation variance) appears, the insulator is expected to gradually melt with increasing temperatures and eventually disappear. We heat the atoms by holding them for a variable amount of time in the dipole trap that precedes the lattice loading. The atom number remains approximately constant during this heating. We observe clear changes in the average and and variance of the occupation distribution from single images, which is also visible in the respective distributions as a function of μ/U (figure 4.6). For higher temperatures, the occupation distribution broadens

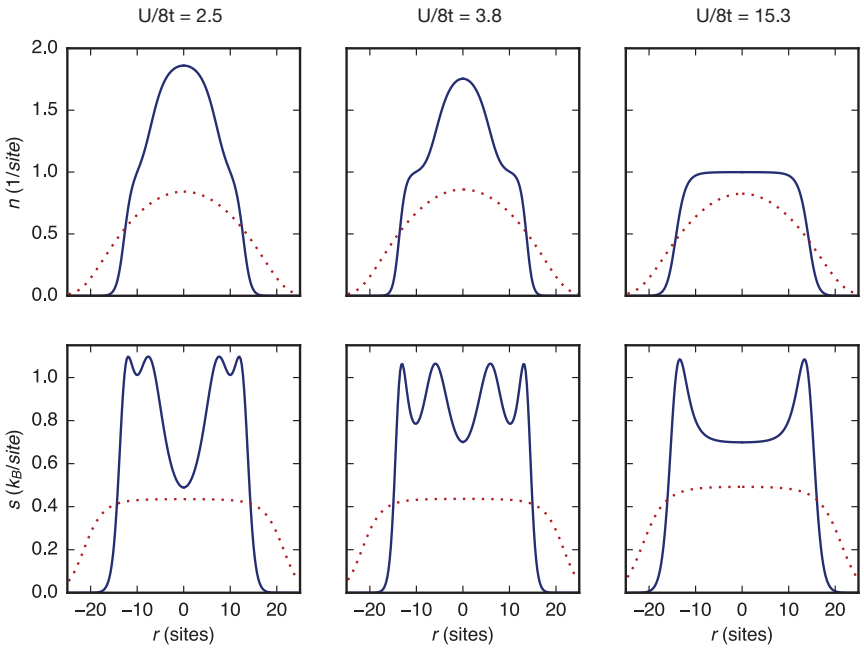

Figure 4.4: A comparison of the calculated density and entropy profiles before and after loading the lattice, assuming that the total entropy remains unchanged during the lattice loading process. The profile in the trap preceding the lattice is denoted by a dotted red line, and the profile after loading the lattice is denoted by a solid blue line. This indicates that for a variety of interaction strengths, the mass and entropy of the cloud must redistribute substantially during lattice loading.

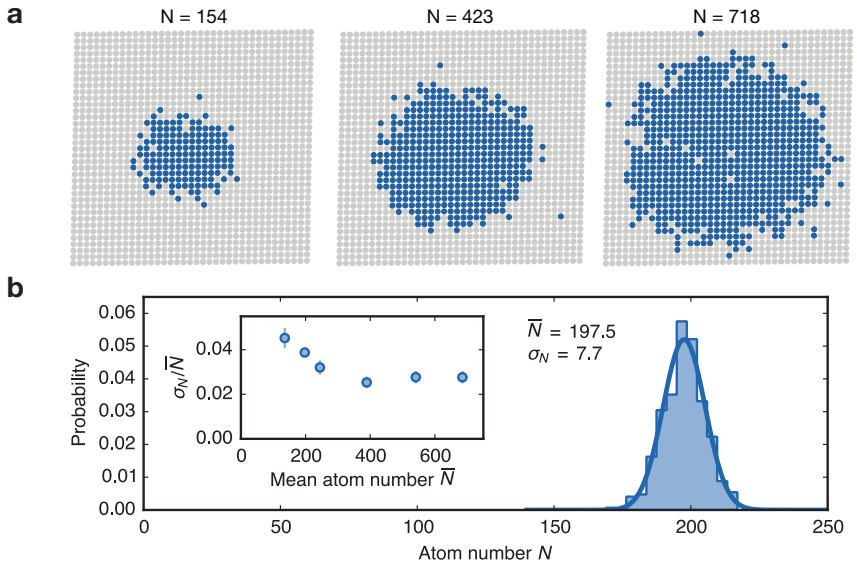

Figure 4.5: (**a**) Single images of MIs with varying detected atom numbers N (without doublons) for $U/8\bar{t} = 15.3(7)$. (**b**) Histogram of detected atom numbers after 400 experiment repetitions with the average atom number, $\bar{N}$, and standard deviation, σ_N. The solid line shows the Gaussian distribution for the obtained $\bar{N}$ and σ_N. The inset shows the experimental stability of preparing samples with fixed atom number, characterized by the relative standard deviation for different $\bar{N}$ obtained from ≥ 50 images. Error bars denote the respective standard errors.

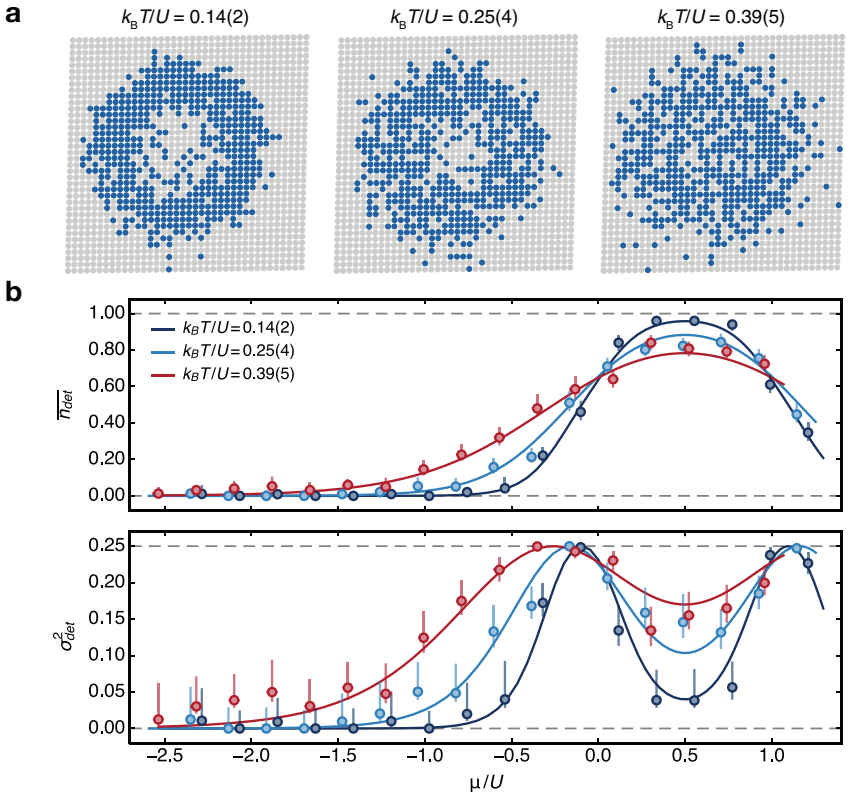

Figure 4.6: (**a**) Detected site occupations from single images at different temperatures for $U/8\bar{t} = 3.8(2)$. The clouds are heated by holding the atom cloud in a crossed dipole trap before the lattice ramps up. Hold times, from left to right, are 0 s, 1 s, and 3 s. (**b**) Corresponding occupation occupation mean and variance profiles versus chemical potential. The dark blue, light blue, and red curves are theory fits used to determine the temperature.

significantly, wheras the variance flattens and is only weakly suppressed at the highest detected occupations ($\mu = U/2$). The temperatures determined from the theory comparison are in the range $k_B T/U = 0.14$ to 0.55, which corresponds to entropies of $S/N = 0.97$ to $1.58\,\mathrm{k_B}$. This shows that temperatures $k_B T \lesssim 0.15U$ are required for MI states.

5

Site-resolved observations of the spin-correlation function

Quantum many-body systems exhibiting magnetic correlations underlie a wide variety of phenomena. High-temperature superconductivity, for example, can arise from the correlated motion of holes on an antiferromagnetic (AFM) Mott insulator [147, 6]. Strongly correlated many-body systems can be realized using ultracold fermionic atoms in optical lattices with a tunability that is unparalleled in conventional solid-state systems [33]. Recent experiments exploring the Hubbard model with cold atoms are accessing temperatures where AFM correlations form, but have only observed these correlations via measurements that were averages over inhomogeneous systems [43, 44]. With the

advance of quantum gas microscopy we can now take a snapshot of the real-space correlations in a single quantum many-body state at the atomic scale [76, 68]. In this chapter I describe site-resolved observations of AFM correlations in a two-dimensional, Hubbard-regime optical lattice and demonstrate the ability to measure the spin-correlation function over any distance. We measure the in-situ distributions of the particle density and magnetic correlations, extract thermodynamic quantities from comparisons to theory, observe statistically significant correlations over three lattice sites, and study how lattice loading dynamics affect our ability to prepare samples in thermal equilibrium. Our temperatures are the lowest reported in a Hubbard model system with cold atoms and approach the limits of available numerical techniques, particularly in the metallic regime away from half-filling. Our results demonstrate that quantum gas microscopy is a powerful tool for studying fermionic quantum magnetism. Direct access to many-body physics at the single-particle level and the microscopic study of quantum dynamics will further our understanding of how new states of matter emerge from the interplay of motion and magnetism in quantum many-body systems.

As described in chapter two, fermionic atoms in a two-dimensional optical lattice can be well described by the Hubbard Hamiltonian, a simple model in which there is a competition between the nearest-neighbor tunneling energy t and the on-site interaction energy U. AFM spin correlations begin to appear in the Hubbard model near half-filling when the temperature scale becomes comparable to the exchange energy, which in the strongly interacting regime is $J = 4t^2/U$. While in three dimensions in the thermodynamic limit there is a finite-temperature phase transition to a state with long-range AFM order, a finite-temperature phase transition is prohibited in two dimensions by the Mermin-Wagner-Hohenberg theorem [148]. Nonetheless, AFM correlations do arise, decaying exponentially with a correlation length ξ that diverges as the temperature goes to zero. We use quantum gas microscopy to reveal precisely these correlations, which lead to long-range order when ξ becomes comparable to the finite system size we investigate.

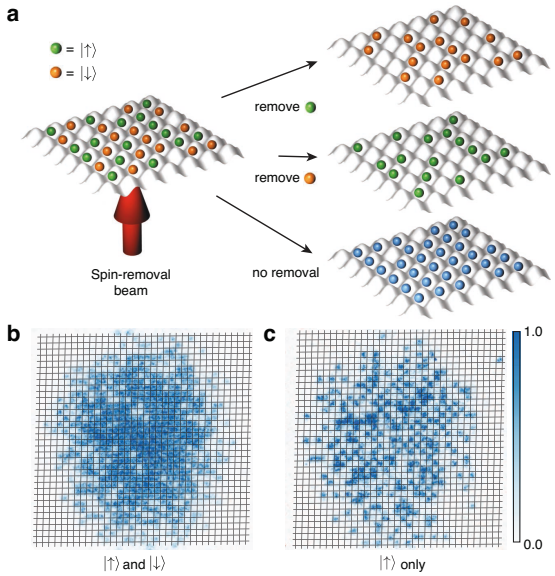

Figure 5.1: **a**, After loading the atoms into an optical lattice we use a spin-removal technique to map the spin correlations onto charge correlations, which can then be detected using site-resolved imaging. The two spin states are denoted by green and orange balls. By driving cycling optical transitions for either spin state with the spin-removal beam we can eject one spin state from the trap. We can then combine charge correlations measured in images where we remove each spin state and where no removal is performed to compute the local spin correlation. **b**, A typical image where no atoms are removed. **c**, A typical image with one of the spins removed.

5.1 Spin-removal technique for measuring correlations

Our experiments begin with a low-temperature, two-dimensional gas of fermionic ^{6}Li atoms in a mixture of the two lowest hyperfine states ($|\uparrow\rangle$ and $|\downarrow\rangle$), prepared as described in chapter one. By adjusting a magnetic bias field in the vicinity of the Feshbach resonance located at 832 G we set the s-wave scattering length to 210 a_0, where a_0 is the Bohr radius (see section 2.1). Using a 30 ms linear ramp, the atoms are adiabatically loaded into an isotropic, square optical lattice with a depth of $s_0 = 7.7(5)\ E_r$, where the recoil energy is $E_r/h = 25.6$ kHz with Planck constant h. We detect magnetic correlations by removing atoms in either spin state, and measuring the resulting charge correlations with site-resolved imaging (see Chapter 3), as shown in figure 5.1. Because our imaging technique removes doubly-occupied sites, both doubly-occupied and unoccupied sites show up as

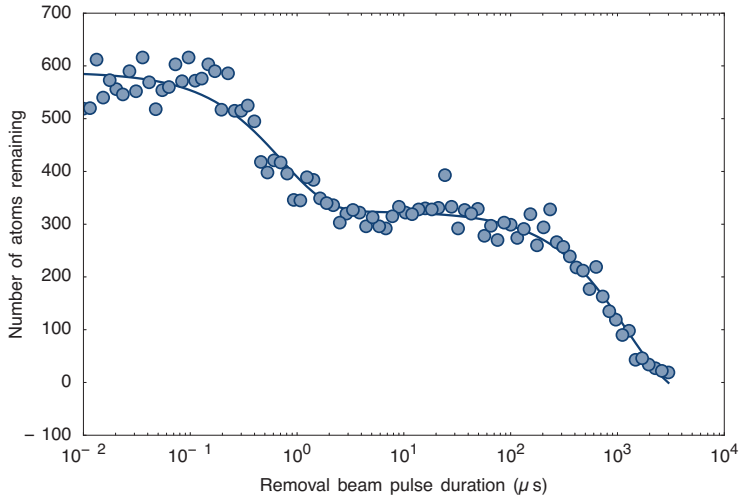

Figure 5.2: A pulse resonant with $|1\rangle$ is applied for variable time, followed by two 100 μs pulses resonant with $|4\rangle$ and $|5\rangle$. The remaining atom number as a function of pulse duration is plotted. The data fits well to a sum of two exponentials, yielding an resonant characteristic removal time of $0.71(8)$ μs and an off-resonant time of $1200(200)$ μs.

empty sites after imaging.

After loading the lattice, the lattice depth is ramped linearly to $s_0 = 50E_r$ in 1 ms, where tunneling is suppressed. The magnetic bias field is then ramped to 500 G. To remove the atoms in $|\uparrow\rangle$ ($|\downarrow\rangle$) a 10 μs resonant pulse drives a nearly closed transition to the $|m_J = -3/2, m_I = 1\rangle$ ($|m_J = -3/2, m_I = 0\rangle$) state of the $2P_{3/2}$ electronic manifold. During this pulse $< 5\%$ of the population leaks into the $|5\rangle$ ($|4\rangle$) state and remain in the lattice. A second 10 μs pulse drives a transition from $|5\rangle$ ($|4\rangle$) to $|m_J = 3/2, m_I = 0\rangle$ ($|m_J = -3/2, m_I = -1\rangle$), ejecting the remaining atoms that were originally in $|\uparrow\rangle$ ($|\downarrow\rangle$) from the trap. Here, we follow the usual convention of labeling the magnetic sublevels of the $2S_{1/2}$ ground electronic manifold $|1\rangle$ through $|6\rangle$ in order of increasing energy.

To determine the appropriate pulse durations for removing atoms in $|\uparrow\rangle$ ($|\downarrow\rangle$) without removing atoms in $|\downarrow\rangle$ ($|\uparrow\rangle$), we ramp to 500 G and apply a resonant pulse as described above for variable

time. The resulting loss in atom number follows the sum of two decaying exponentials, corresponding to the loss of the target and non-target spins (figure 5.2). The characteristic decay times of these exponentials differ by a factor of approximately 1700, reflecting the ratio between resonant and off-resonant scattering rates. We choose the duration of the spin-removal pulse to be equal to ten times the resonant decay time. For this pulse duration, we remove 99.995% of atoms with the target spin while eliminating only 0.6% of the other spin.

Denoting the observation of a particle (hole) on the site at $\boldsymbol{r}$ by $p_{\boldsymbol{r}}$ ($h_{\boldsymbol{r}}$), we determine the spin correlator (see section 5.3)

$$C_{\boldsymbol{a}}(\boldsymbol{r}) = 4\Big(\left\langle S^z_{\boldsymbol{r}} S^z_{\boldsymbol{r}+\boldsymbol{a}} \right\rangle - \left\langle S^z_{\boldsymbol{r}} \right\rangle \left\langle S^z_{\boldsymbol{r}+\boldsymbol{a}} \right\rangle \Big) \tag{5.1}$$

Here, $S^z_{\boldsymbol{r}} = \frac{1}{2}(n^{\uparrow}_{\boldsymbol{r}} - n^{\downarrow}_{\boldsymbol{r}})$, with $n^{\sigma}_{\boldsymbol{r}}$ denoting the number of particles of spin σ on the site at $\boldsymbol{r}$. We take an average of $C_{\boldsymbol{a}}(\boldsymbol{r})$ over all $\boldsymbol{a}$ where $|\boldsymbol{a}| = d$ to obtain $C_d(\boldsymbol{r})$. The nearest-neighbor, diagonal next-nearest-neighbor, straight next-nearest-neighbor, etc. correlators are given by $C_1(\boldsymbol{r})$, $C_{1.4}(\boldsymbol{r})$, and $C_2(\boldsymbol{r})$, etc. From images where neither spin was removed we directly obtain a spatial map of the single occupation probability $\overline{n}_{\text{det}}(\boldsymbol{r})$ which also corresponds to the local moment $C_0(\boldsymbol{r})$.

5.2 Observations of the spin-correlation function

After loading atoms into the lattice we observe AFM correlations for nearest-neighbors and diagonal next-nearest-neighbors. These correlations are strongest in the cloud center where the local chemical potential is set to approximately half-filling. The spatial maps $\overline{n}_{\text{det}}(\boldsymbol{r})$, $C_1(\boldsymbol{r})$, $C_{1.4}(\boldsymbol{r})$ for colder (top) and hotter (bottom) temperatures are shown in panels a, b, and c, respectively, of figure 5.3. For these data the interaction is tuned to $U = 6.82(10)$ kHz with $t = 850(100)$ Hz ($U/t = 8.0(1)$). The chemical potential is tuned to approximately $\mu = U/2$ in the center of the cloud for the colder data by adjusting the atom number to maximize $\overline{n}_{\text{det}}$ in the center. To heat the cloud,

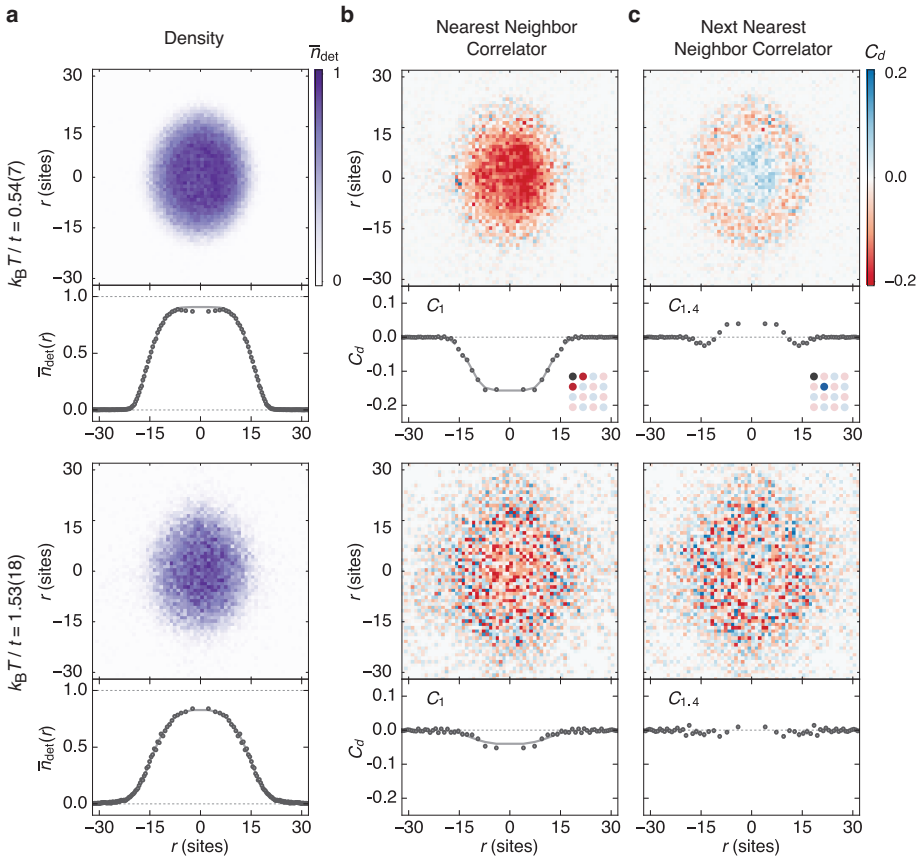

Figure 5.3: a-c, We show spatial maps and azimuthally averaged profiles (mirrored about $r = 0$ and corrected for ellipticity) of the detected density, nearest-neighbor correlator, and diagonal next-nearest neighbor correlator for a cold (top) and hot (bottom) cloud.

we hold the atoms in the optical dipole trap for 4 s before loading the lattice. After heating, the maximum detected occupation decreases from 0.89(1) to 0.84(1) with a slight broadening of the density profile, while the largest magnitude of the nearest-neighbor correlator decreases from 0.154(3) to 0.052(6). In this regime, where the exchange energy is much smaller than both U and the bandwidth, an increase in temperature quickly saturates the entropy available in the spin degree of freedom while creating little entropy in the charge degree of freedom, making the nearest-neighbor correlator much more sensitive than the density to temperature changes.

We take azimuthal averages along the equipotentials of the underlying harmonic trap to obtain $\overline{n}_{\text{det}}(r)$ and $C_d(r)$. The resulting profiles are simultaneously fit to the results of a numerical linked-cluster expansion (NCLE) of the 2D Hubbard model under a local density approximation (LDA) (see section 5.5.2) [149, 150]. From these fits we obtain a temperature $k_B T/t = 0.54(7)$ and chemical potential $\mu/U = 0.52(1)$ for the cooler data and $k_B T/t = 1.53(18)$ and $\mu/U = 0.33(1)$ for the hotter data. The excellent agreement with theory provides a strong indication that the local density approximation and the assumption of thermal equilibrium are valid.

By evaporatively cooling further prior to lattice loading, we are able to prepare samples with even larger nearest-neighbor correlations. However, for this data, the NLCE theory error is too large away from half-filling for the fit to converge, owing to the low temperature. Because the averaged correlator in the center may not be at exactly half-filling, by comparing this value for the coldest dataset to a quantum Monte Carlo (QMC) calculation at half-filling [151], we can determine an upper bound on the temperature. The correlator value of $0.190(8)$ gives $k_B T/t < 0.45(2)$, the lowest temperature reported for a Hubbard-regime cold atom system. The QMC calculation also predicts that the nearest-neighbor correlator settles as $T \to 0$ to a value of -0.36. Our largest measured nearest-neighbor correlation is therefore 53% of the largest predicted value. In figure 5.4a we plot our largest measured value of the correlator for samples prepared at different temperatures, the temperature derived from the NLCE fits where they converge (x-axis), and the QMC upper

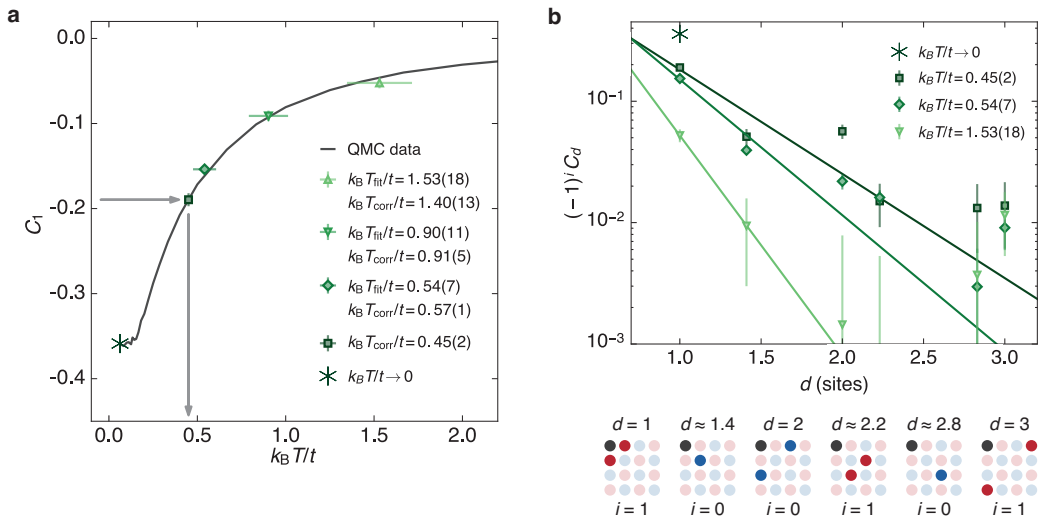

Figure 5.4: **a**, We plot the nearest-neighbor correlator in the center of the cloud for samples prepared at different temperatures. We determine $k_B T_{\text{fit}}/t$ from fits of a numerical linked-cluster expansion to the radial profile and $k_B T_{\text{corr}}/t$ by comparing the central correlator value to a quantum Monte Carlo calculation at half-filling (solid line) [151]. For the coldest data in panels **a** and **b** the NLCE theory error is too large for a fit and we report only the QMC result. **b**, An exponential fit to the correlator in the center of the cloud versus d allows us to extract the correlation length for datasets at three different temperatures, giving 0.24(9), 0.39(2), and 0.51(4) sites for decreasing temperature. The asterisk denotes the nearest-neighbor correlator value from the QMC calculation in **a** as $T \to 0$. Error bars on $\overline{n}_{\text{det}}(\boldsymbol{r})$ and $C_d(r)$ are standard errors after averaging at least 20 sets of combined correlation maps and averaging azimuthally (see section 5.5.1). Horizontal errors in **a** are fit errors.

bound. We find excellent agreement between our data and theoretical prediction, which is consistent with half-filling at the cloud center.

We see statistically significant antiferromagnetic correlations to distances of three sites and the sign of every measured correlator value is consistent with antiferromagnetic ordering. Our ability to measure correlations at all length scales allows us to directly extract the correlation length, as shown in figure 5.4b. Samples are prepared at three different temperatures with the atom number optimized to achieve half-filling in the center of the cloud. Values for the correlator are taken by averaging the spatial maps over a region in the center of the cloud with a 6-site radius. To determine the correlation length we perform an exponential fit of $(-1)^i C_d$ in the center of the cloud versus d, where $i = 0\,(1)$ if d is such that the two sites are on the same (a different) sublattice. The correlation lengths are $0.24(9)$, $0.39(2)$, and $0.51(4)$ sites for temperatures of $k_B T/t = 1.53(18), 0.54(7)$, and $0.45(2)$, respectively. The asterisk shows the QMC prediction of 0.36 for the nearest-neighbor correlator at half-filling as $T \to 0$.

Quantum gas microscopy also allows for a detailed study of the thermalization of the atomic cloud when loading into the lattice. We investigate the formation of spin correlations and the thermalization of the density distribution for different lattice loading times in figure 5.5. In these data the lattice is ramped on linearly with a varying duration t_L. We determine the radius r_{max} where $\overline{n}_{\text{det}}(r)$ is maximized. For a cloud in thermal equilibrium with r_{max} not in the center of the cloud, r_{max} corresponds to half-filling ($\mu = U/2$). Figure 5.5a shows $\overline{n}_{\text{det}}(r_{\text{max}})$ and $C_d(r_{\text{max}})$ as a function of loading time. The detected density grows from 0.6 at short loading times and settles at about 0.9 for $t_L = 10$ ms. The loading time required for the density to settle also corresponds to the maximum absolute values for both the nearest-neighbor and next-nearest-neighbor spin-correlators. The matching timescales suggest that the suppression of magnetic correlations at $t_L < 10$ ms is due to the low initial density and not to exchange dynamics. The density at short loading times is determined by the confinement of the optical dipole trap preceding the lattice loading (section 1.4).

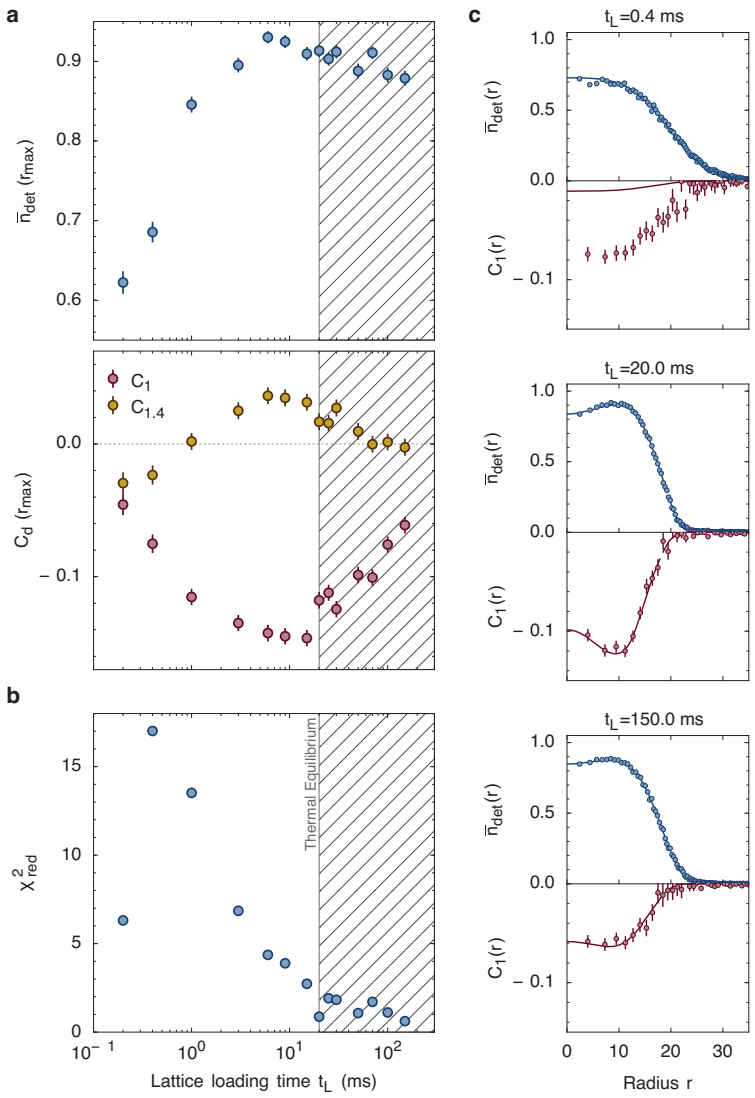

Figure 5.5: **a**, We measure the detected density (upper) as well as the nearest- and next-nearest-neighbor spin correlator at $r_{\max}$ as a function of lattice loading time t_L, where $r_{\max}$ is the radius where $\overline{n}_{\text{det}}$ is maximized (lower). **b**, We compute the reduced chi-squared (χ^2_{red}) of simultaneous fits of the density and nearest-neighbor correlator profiles to NLCE data. A value $\chi^2_{\text{red}} \approx 1$ indicates a good fit, consistent with our model which assumes thermal equilibrium. χ^2_{red} settles to approximately one at a lattice loading time of 20 ms, indicated by the shaded region. **c**, Sample profile fits for three different loading times.

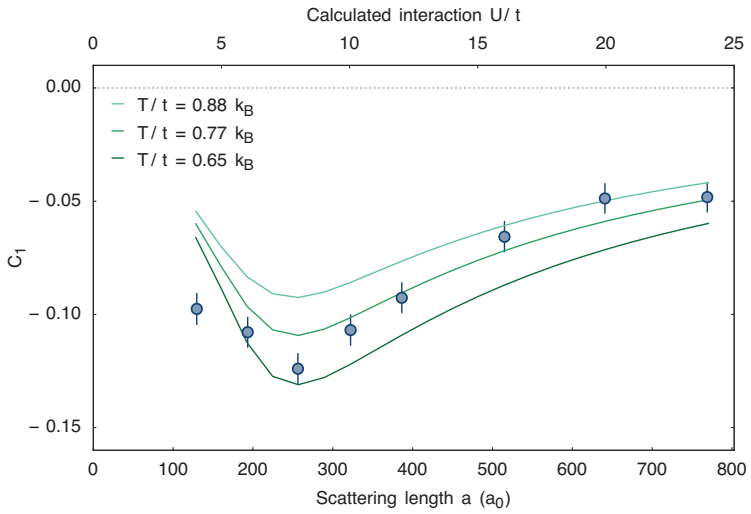

Figure 5.6: We plot the nearest-neighbor correlator at half-filling for varying scattering length. The top y-axis gives computed values of U/t for each scattering length. The solid lines are isothermal theory curves from the NLCE theory.

For loading times larger than 10 ms both $(-1)^i C_d(r_{\max})$ and $\overline{n}_{\text{det}}(r_{\max})$ decay, consistent with heating. The faster decay of $(-1)^i C_d(r_{\max})$ is further indication that the spin correlators are much more sensitive than the density to temperature in this regime of parameters.

We also study thermalization by fitting the data for different loading times to the NLCE theory and performing a reduced chi-squared (χ^2_{red}) analysis. Figure 5.5b shows χ^2_{red} versus loading time, and figure 5.5c shows individual NLCE fits at t_L of 0.4 ms, 20 ms, and 150 ms from top to bottom. The value of χ^2_{red} settles to approximately one on a 20 ms timescale, which is slightly longer than the settling times for the density and spin correlator. The value of χ^2_{red} remains near unity up to our largest loading times, showing that the density and spin correlator distributions remain consistent with thermal equilibrium.

While in Bose-Hubbard systems AFM correlations only appear in the Heisenberg limit $U \gg t$, Fermi-Hubbard systems exhibit AFM correlations at all U/t, with a maximum in the correlations occurring near $U/t = 8$. For large U/t, AFM correlations are suppressed because the exchange

energy becomes small compared to the temperature. For $U/t < 8$, where the interaction energy is smaller than the bandwidth, charge fluctuations destroy the magnetic correlations. We study these effects by varying the scattering length for fixed $t = 970(110)$ Hz. In figure 5.6 we plot $C_1(r_{\max})$ versus the scattering length, along with the predictions of the NLCE theory for three different temperatures. We show the calculated U/t from Wannier functions in the lowest band, while for our parameters corrections to this single-band approximation could play a role [152]. The data shows the expected dependence on U/t from the simple picture mentioned above. We also compare our data with theoretical isothermal curves at half-filling. In this comparison additional factors should be considered. First, the atom number number is fixed, and so the chemical potential in the center of the cloud varies with U/t. Second, we anticipate the loading entropy to be approximately fixed, as opposed to the temperature, and so the data are not expected to strictly follow a single isotherm. The comparison of data with the theory reflects differences between the thermodynamic preparation of atomic and conventional solid-state systems.

Our ability to observe the in-situ, site-resolved distribution of spin correlations at all distances has enabled unprecedented comparison with numerical studies and detailed verification that the atomic sample behaves in a manner consistent with thermal equilibrium. These experimental benchmarks on thermal equilibrium affirm our understanding of the entropy distribution, paving the way for the implementation of entropy redistribution techniques to achieve finite-system-size long-range order [144, 145]. Implementation of such techniques would require precise trap-shaping protocols, which have been fruitfully demonstrated in bosonic quantum gas microscopes [153]. Beyond equilibrium physics, we could also exploit our ability to take temporally resolved snapshots of the correlations in a many-body wavefunction, allowing for in-depth studies of non-equilibrium physics beyond the capability of existing theoretical tools [154].

5.3 Mapping spin correlations onto charge correlations

We wish to extract the polarization-corrected two-point spin correlator, $4(\langle S_z S_z \rangle - \langle S_z \rangle^2)$, where $S_z = \frac{1}{2}(n_\uparrow - n_\downarrow)$ and lattice site labels for the two-point correlator expectation value entries have been dropped. Table 5.1 lists all of our observable two-point correlators using the spin-removal detection scheme, with d denoting a doubly occupied site, p a singly occupied site, and h an unoccupied site. The expectation value, $\langle\rangle_{\text{NR}}$, is over multiple images where neither spin was removed, and the expectation value, $\langle\rangle_{R\uparrow}$ ($\langle\rangle_{R\downarrow}$), is over multiple images where the atoms in $|\uparrow\rangle$($|\downarrow\rangle$) were removed. In our observed charge correlations we cannot distinguish between unoccupied and doubly occupied sites, so both cases are denoted with h in the formulas below. By combining correlators in the table, we are able to calculate the polarization-corrected spin correlator in two independent ways:

$$
\begin{aligned}
C'(\mathrm{r}) &= \frac{1}{2} \sum_{\sigma \in \{\uparrow,\downarrow\}} (\langle pp \rangle_{R\sigma} + \langle hh \rangle_{R\sigma} - \langle ph \rangle_{R\sigma} - \langle hp \rangle_{R\sigma}) - \langle hh \rangle_{NR} - \left(\langle p \rangle_{R\uparrow} - \langle p \rangle_{R\downarrow} \right)^2 \\
C'_{alt}(\mathrm{r}) &= 2 \sum_{\sigma \in \{\uparrow,\downarrow\}} \langle pp \rangle_{R\sigma} - \langle pp \rangle_{NR} - \left(\langle p \rangle_{R\uparrow} - \langle p \rangle_{R\downarrow} \right)^2
\end{aligned}
\tag{5.2}
$$

These formulas are incorrect when $\langle p \rangle_{R\uparrow} + \langle p \rangle_{R\downarrow} \neq \langle p \rangle_{NR}$, as in the case of insufficently long or off-resonant removal pulses. The removal of spins is performed in a deep lattice and so is an uncorrelated process. As a result, we can correct for this systematic by removing the uncorrelated contribution to each two-point correlator. For example, the correlator $\langle pp \rangle$ is equal to $\langle p \rangle^2$ in a sample with no particle correlations. In addition, we remove the polarization correction term $\left(\langle p \rangle_{R\uparrow} - \langle p \rangle_{R\downarrow} \right)^2$ to avoid double-counting it as it is part of the uncorrelated contribution to

the correlators.

$$\begin{aligned} C(\mathrm{r}) = \; & \frac{1}{2} \sum_{\sigma \in \{\uparrow,\downarrow\}} \Big[\langle pp \rangle_{R\sigma} + \langle hh \rangle_{R\sigma} - \langle ph \rangle_{R\sigma} - \langle hp \rangle_{R\sigma} \\ & - \left(\langle p \rangle_{R\sigma}^2 + (1 - \langle p \rangle_{R\sigma})^2 - 2 \langle p \rangle_{R\sigma} (1 - \langle p \rangle_{R\sigma}) \right) \Big] \\ & - \left(\langle hh \rangle_{NR} - (1 - \langle p \rangle_{NR})^2 \right) \\ C_{alt}(\mathrm{r}) = \; & 2 \sum_{\sigma \in \{\uparrow,\downarrow\}} \left(\langle pp \rangle_{R\sigma} - \langle p \rangle_{R\sigma}^2 \right) - \left(\langle pp \rangle_{NR} - \langle p \rangle_{NR}^2 \right) \end{aligned} \tag{5.3}$$

The following relation between the original and revised correlators holds:

$$\begin{aligned} C(\mathrm{r}) &= C' + \langle h \rangle_{NR}^2 - (1 - \langle p \rangle_{R\uparrow} - \langle p \rangle_{R\downarrow})^2 \\ C_{alt}(\mathrm{r}) &= C'_{alt} + \langle p \rangle_{NR}^2 - (\langle p \rangle_{R\uparrow} + \langle p \rangle_{R\downarrow})^2 \end{aligned} \tag{5.4}$$

As expected, these additional terms cancel when there is no spin-removal systematic. The effectiveness of these correction factors in removing spin-removal systematics is discussed in a later section.

Calculating the spin-removal and polarization corrections requires estimating the square of expectation values. Unfortunately, directly squaring the mean estimators yields biased estimators for these terms. We can treat measurements of the various densities as independent and identically distributed Bernoulli random variables $X_i, ..., X_n$ with success probability p and $Y_i, ..., Y_n$ with success probability q. We calculate the expectation value of the estimators:

$$\begin{aligned} \mathrm{E}\left[\widehat{p^2}\right] &= \mathrm{E}\left[\left(\frac{1}{n} \sum_{i=1}^{n} X_i \right)^2 \right] \\ &= \frac{1}{n^2} \left(\sum_{i \neq j} \mathrm{E}[X_i X_j] + \sum_i \mathrm{E}[X_i^2] \right) \\ &= \left(1 - \frac{1}{n} \right) p^2 + \left(\frac{1}{n} \right) p \end{aligned} \tag{5.5}$$

$$
\begin{aligned}
\mathrm{E}\left[\widehat{(p \pm q)^2}\right] &= \mathrm{E}\left[\left(\frac{1}{n}\sum_{i=1}^{n} X_i \pm \frac{1}{n}\sum_{i=1}^{n} Y_i\right)^2\right] \\
&= \mathrm{E}\left[\left(\frac{1}{n}\sum_{i=1}^{n} X_i\right)^2\right] + \mathrm{E}\left[\left(\frac{1}{n}\sum_{i=1}^{n} Y_i\right)^2\right] \pm \mathrm{E}\left[\frac{2}{n^2}\sum_{i,j} X_i Y_j\right] \\
&= \left(1 - \frac{1}{n}\right)(p^2 + q^2) + \left(\frac{1}{n}\right)(p + q) \pm 2pq \\
&= (p \pm q)^2 - \frac{1}{n}\left(p^2 + q^2 - p - q\right)
\end{aligned}
\tag{5.6}
$$

We can then construct bias-free estimators:

$$
\begin{aligned}
\widehat{p^2}' &= \frac{n}{n-1}\widehat{p^2} - \frac{1}{n-1}\hat{p} \\
\widehat{(p \pm q)^2}' &= \widehat{(p \pm q)^2} + \frac{1}{n}\left(\widehat{p^2}' + \widehat{q^2}' - \hat{p} - \hat{q}\right)
\end{aligned}
\tag{5.7}
$$

For our correlator maps, the bias correction for $\widehat{p^2}$ is maximally 0.0125 and for $\widehat{(p \pm q)^2}$ is 0.025, which can be significant. When performing azimuthal averages the correction factor is at most 0.0005.

5.4 Sources of systematic error for the spin correlation measurement

We study systematic errors in the spin correlator caused by excessive or insufficient durations of the spin-removal pulse and also by an imperfect imaging fidelity. To obtain a systematic error on our spin correlator measurements due to fluctuations in the spin-removal efficiency, we measure how the spin correlator varies with spin-removal pulse duration. For fixed interactions and lattice depths, we vary the spin-removal pulse duration between 1.5τ and 185τ, where τ is the fast exponential decay time of the spin removal. We examine the resultant effect on C, C', C_{alt}, and C'_{alt} for nearest-neighbor correlations in the center of the atomic sample (see figure 5.7). We find that the corrected correlators C and C_{alt} agree for all spin-removal durations and exhibit a relatively small dependence on the

Measured Correlator	Corresponding Spin Correlator
$\langle pp \rangle_{NR}$	$\langle\uparrow\uparrow\rangle + \langle\downarrow\downarrow\rangle + \langle\uparrow\downarrow\rangle + \langle\downarrow\uparrow\rangle$
$\langle ph \rangle_{NR}$	$\langle\uparrow h\rangle + \langle\downarrow h\rangle + \langle\uparrow d\rangle + \langle\downarrow d\rangle$
$\langle hp \rangle_{NR}$	$\langle h\uparrow\rangle + \langle h\downarrow\rangle + \langle d\uparrow\rangle + \langle d\downarrow\rangle$
$\langle hh \rangle_{NR}$	$\langle hh\rangle + \langle dd\rangle + \langle hd\rangle + \langle dh\rangle$
$\langle pp \rangle_{R\uparrow}$	$\langle\downarrow\downarrow\rangle$
$\langle ph \rangle_{R\uparrow}$	$\langle\downarrow h\rangle + \langle\downarrow d\rangle + \langle\downarrow\uparrow\rangle$
$\langle hp \rangle_{R\uparrow}$	$\langle h\downarrow\rangle + \langle d\downarrow\rangle + \langle\uparrow\downarrow\rangle$
$\langle hh \rangle_{R\uparrow}$	$\langle\uparrow\uparrow\rangle + \langle h\uparrow\rangle + \langle d\uparrow\rangle + \langle\uparrow h\rangle + \langle\uparrow d\rangle + \langle hh\rangle + \langle dd\rangle + \langle dh\rangle + \langle hd\rangle$
$\langle pp \rangle_{R\downarrow}$	$\langle\uparrow\uparrow\rangle$
$\langle ph \rangle_{R\downarrow}$	$\langle\uparrow h\rangle + \langle\uparrow d\rangle + \langle\uparrow\downarrow\rangle$
$\langle hp \rangle_{R\downarrow}$	$\langle h\uparrow\rangle + \langle d\uparrow\rangle + \langle\downarrow\uparrow\rangle$
$\langle hh \rangle_{R\downarrow}$	$\langle\downarrow\downarrow\rangle + \langle h\downarrow\rangle + \langle d\downarrow\rangle + \langle\downarrow h\rangle + \langle\downarrow d\rangle + \langle hh\rangle + \langle dd\rangle + \langle dh\rangle + \langle hd\rangle$

Table 5.1: This table lists all of the two-point correlators that can be observed with the spin-removal detection method. Here p refers to particle, h to hole, and d to doublon. The left column lists the correlators that can be directly observed. Due to parity imaging, we are unable to distinguish between holes and doublons, so the detection of either is denoted h. The expectation values $\langle\rangle_{NR}$, $\langle\rangle_{R\uparrow}$, and $\langle\rangle_{R\downarrow}$ denote correlators in images after no spin removal, removing $|\uparrow\rangle$, and removing $|\downarrow\rangle$ respectively. The right column shows the two-point spin correlators corresponding to each of the directly measured charge correlators.

spin-removal time. They are maximized around the chosen spin-removal time, and decrease away from that time because information about correlations is lost in the case of incomplete or off-resonant removal. The uncorrected correlators C' and C'_{alt} disagree significantly away from the chosen removal time, because of the systematic on the correlator described in an earlier section. When running the experiment, we measure the exponential decay time of the removal pulse regularly and find that it never varies by more than 20%. From the measured systematic variation in C with spin-removal duration, we estimate that the fluctuations in our reported correlations due to variation in the spin-removal timescale are at most 0.2%, well within statistical uncertainties. We also find that the two correlators agree for our chosen spin-removal pulse duration.

In areas of high filling, atoms which hop to neighboring sites during an imaging sequence may create correlated losses. To examine possible systematic errors on the spin correlator due to imperfect

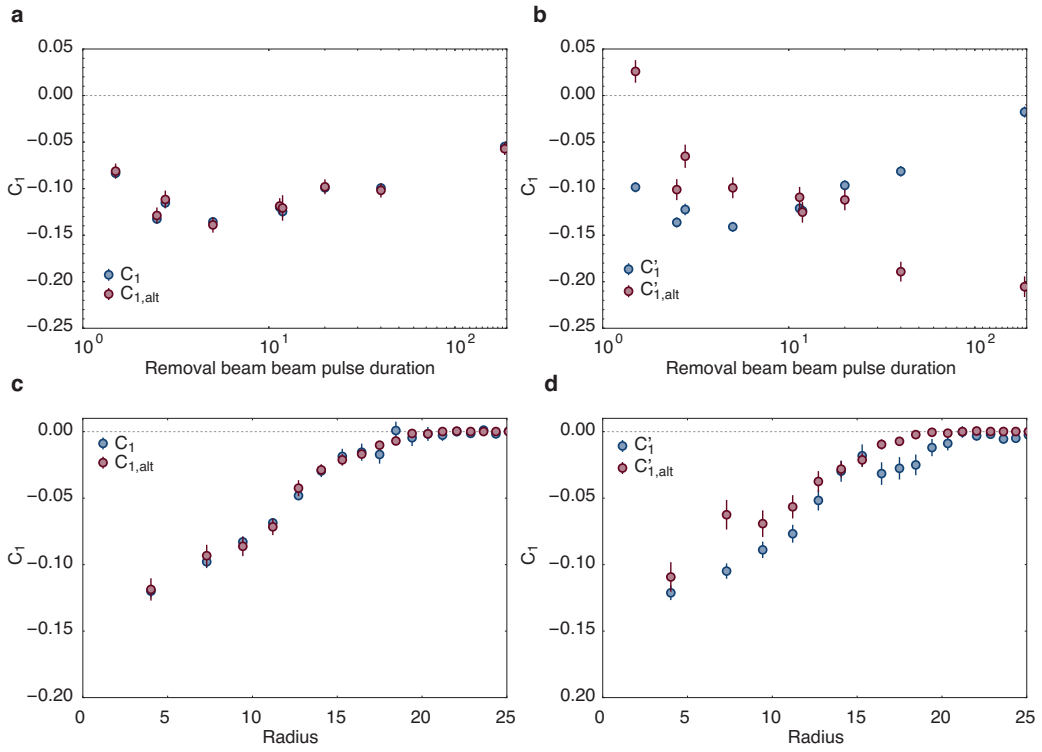

Figure 5.7: a, The correlator resulting from varying removal pulse duration is plotted for both corrected methods used to measure the spin correlator. The two methods agree for all durations. The reduction in correlations away from the chosen removal time is due to the loss of information caused by incomplete or off-resonant removal. **b,** Analogous plot for the uncorrected spin correlators. Without the correction, the correlators agree at our chosen removal time but diverge strongly away from that point. **c, d,** Exemplar profiles of the correlator with and without correction, respectively. While the corrected correlators demonstrate agreement across the entire sample, the uncorrected correlators do not. Based on typical fluctuations in spin removal efficiency, for the corrected spin correlator we estimate the systematic error due to spin removal to be $3(1) \times 10^{-4}$.

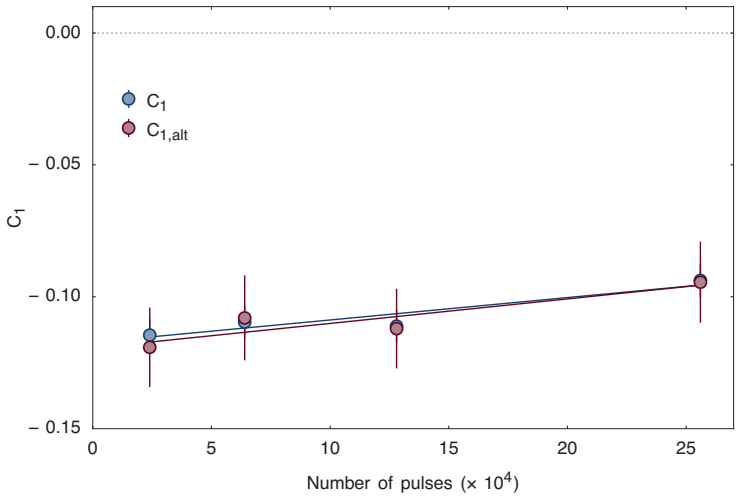

Figure 5.8: For both corrected methods used to measure the correlator, the correlator resulting from a varying number of imaging pulses is plotted. Across the entire range investigated, the two methods agree. Based on fluctuations in imaging efficiency, we estimate the systematic error due to imaging to be $4(2) \times 10^{-5}$.

imaging fidelity, we vary the number of imaging pulses in our Raman imaging sequence (see chapter three) and observe the resulting systematic shifts in C and C_{alt} in the center of the cloud (see figure 5.8). The number of pulses is varied between 2.4×10^4 and 2.56×10^5, compared to the typical value of 3.2×10^4 pulses. For these pulse numbers, the imaging fidelity to varies linearly between 99.3% and 92.0%, respectively. We find a small systematic shift in both correlators of $8.6(4.1) \times 10^{-}8$ per pulse. Given a typical imaging fidelity of 98% the fluctuations in the correlator due to imaging are at most 0.04%, which is negligible compared to our statistical uncertainties.

5.5 Comparison with numerical simulations

5.5.1 Azimuthal averaging

After obtaining the site-resolved population for a set of images with a given spin-removal sequence, we calculate spatial maps of each two-point charge correlation function and the detected on-site

density. We average between 20 and 125 spatial maps to calculate spatial maps of average the quantities $\langle pp \rangle$, $\langle ph \rangle$, $\langle hp \rangle$, $\langle hh \rangle$, and the average single-particle density $\langle p \rangle$. We then combine these quantities, as described above, to determine $C(\boldsymbol{r})$. To compute radial profiles of these quantities, we simultaneously average across images and across approximately-equal-area ellipsoidal annuli of similar chemical potential. We use annuli containing 35-46 lattice sites for density calculations, and 82-92 sites for spin correlator calculations. During analysis, we scale the coordinate system by the square root of the ratio of the cloud widths along each lattice axis. Reported radii and harmonic trap frequencies are measured in this rotationally-symmetric coordinate system.

The singles densities are well-described by the mean value of repeated Bernoulli trials, so we use an Agresti-Coull interval to estimate their confidence intervals. Errors for measured densities away from zero and one asymptotically approach the normal approximation to the standard error of the mean. For the number of samples we use, their disagreement is less than 4% for mean values between 0.01 and 0.99, validating our use of the χ^2_{red} test statistic to describe goodness-of-fit. For site densities close to zero and one, the error distribution is no longer normal. For this reason, our calculations of χ^2_{red} exclude values of the density at radii larger than 18 lattice sites, ensuring that for all datasets the density remains larger than 1%.

The individual components of the spin correlator are well-described by the mean value of repeated Bernoulli trials. Since each point in the radial profiles is an average of more than 1000 data points, we use the central limit theorem to model the error on each component as normally distributed and use standard error propagation techniques to calculate the error on the correlator. For correlator values close to zero, the assumptions of the central limit theorem no longer hold. We show the normal standard error for these points in plots, but apply the same radial cutoff used in the density distributions to calculate the χ^2_{red} of our fits.

5.5.2 Fits to the NLCE data

The system is governed by the Hubbard Hamiltonian, a single band model that includes nearest-neighbor tunneling parameterized by the tunneling energy t, and an on-site interaction parametrized by the interaction energy U:

$$\begin{aligned}\hat{H} = &- t \sum_{\langle ij \rangle, \sigma} (\hat{c}^{\dagger}_{i\sigma} \hat{c}_{j\sigma} + h.c.) + U \sum_{i} \hat{n}_{i\uparrow} \hat{n}_{i\downarrow} \\ &+ \sum_{i,\sigma} (V_i - \mu) \hat{n}_{i\sigma}.\end{aligned} \tag{5.8}$$

Here, $\hat{c}^{\dagger}_{i\sigma}$ and $\hat{c}_{i\sigma}$ are the fermionic creation and annihilation operators for a particle on site i with spin $\sigma \in \{\uparrow, \downarrow\}$, $\hat{n}_{i\sigma} = \hat{c}^{\dagger}_{i\sigma} \hat{c}_{i\sigma}$ is the density operator, V_i denotes the trap energy offset, and μ is the chemical potential.

To compare our measurements to theory we model our data within a local density approximation (LDA), which states that the entire atomic cloud can be considered as a locally homogeneous system with a spatially varying chemical potential $\mu_{\mathrm{LDA}}(r)$ as a function of distance r to the cloud center normalized in units of the lattice spacing l:

$$\mu_{\mathrm{LDA}}(r) = \mu - \frac{1}{2} m \overline{\omega}^2 l^2 r^2. \tag{5.9}$$

Here μ is the chemical potential in the center of the trap, m is the atomic mass of ^{6}Li and $\overline{\omega} = \sqrt{\omega_x \omega_y}$ is the geometric mean of the trap frequencies along the x and y directions. The confinement of the atomic cloud originates from the underlying Gaussian beam profile of the laser beams forming the optical lattice. As the beam waists in our experiment correspond to approximately 190 sites and typical cloud radii are about 20 sites, a harmonic confinement with a quadratic dependence with distance is an excellent approximation. We have verified that including the next order quartic

term (which can be estimated from the respective beam waists) does not change any obtained fit parameter throughout the manuscript by more than its individual error bar.

We compare the measured radial profiles of the site occupation $\overline{n}_{\text{det}}(r)$ and nearest-neighbor spin correlator $C_1(r)$ to theoretical predictions of the single-band two-dimensional Hubbard model on a square lattice in the grand-canonical ensemble. The theoretical calculation is based on a NLCE, which includes terms up to ninth order that are resummed with Wynn and Euler resummation techniques [149]. The data is given on a dense grid of $(\mu/t, k_B T/t, U/t)$ values and we use a linear interpolation between points. For low temperatures and away from half-filling ($\mu = U/2$) deviations in the theoretical predictions are observed between the different resummation techniques (mostly visible as oscillations in the data versus μ). For all fits and theory profiles shown in the manuscript we omit theory points with an absolute deviation larger than 0.02 in the occupation and spin correlator value. For $U/t = 8$ this typically restricts reliable fitting to temperatures $k_B T/t > 0.5$.

We perform a simultaneous fit of the measured profiles $\overline{n}_{\text{det}}(r)$ and $C_1(r)$ to theoretically calculated profiles $\overline{n}_{\text{det}}^{\text{theory}}(r)$ and $C_1^{\text{theory}}(r)$, with the temperature T and chemical potential μ in the center of the harmonic trap as free parameters. The fitting algorithm minimizes the reduced chi-squared value

$$\chi^2_{\text{red}}(T,\mu) = \frac{1}{L}\left[\sum_i \left[\frac{\overline{n}_{\text{det}}(r_i) - \overline{n}_{\text{det}}^{\text{theory}}(r_i)}{\sigma_{\overline{n}_{\text{det}}(r_i)}}\right]^2 + \sum_j \left[\frac{C_1(r_j) - C_1^{\text{theory}}(r_j)}{\sigma_{C_1(r_j)}}\right]^2\right]. \tag{5.10}$$

Here L is the number of degrees of freedom for the simultaneous fit and r_i, r_j denote the radial distances of the individual experimental data points for the site occupation and spin correlation with normal standard errors $\sigma_{\overline{n}_{\text{det}}(r_i)}$ and $\sigma_{C_1(r_j)}$. If an experimental data point coincides with a point where the theoretical prediction becomes unreliable (which occurs for $< 10\%$ of the data points in all fits), the reduced chi-squared value is rescaled accordingly. In the main text we quantify the quality of the fit by the reduced chi-squared value at the optimal fit values for parameters T and μ.

5.6 System Calibrations

We calibrate the lattice depth by performing lattice modulation spectroscopy with a non-interacting sample, as described in section 1.5.1. In brief, we determine inter-band resonance frequencies from the spatial widths of the atomic cloud after modulation and subsequent holding time. These resonance frequencies are then compared to band structure calculations to determine the lattice depths along the x and y directions. The nearest-neighbor tunneling matrix elements are calculated from Wannier function overlaps in the single-band approximation. This method is also used to calibrate the lattice depth along the z direction used for creating a single 2D layer.

A calibration of the underlying harmonic trap frequency can be obtained from breathing-mode oscillations, just as in 1.5.2. After loading a non-interacting gas into the potential of a single-beam lattice, we rapidly decrease the lattice depth and measure the spatial width of the atomic cloud after variable oscillation times. We have verified that additional quartic terms originating from the underlying Gaussian beam profile of the laser beams have a negligible effect on the breathing frequency by varying the excitation amplitude. We repeat this measurement for different lattice depths to obtain a trap frequency calibration. For the lattice depth used in this work we find a geometric mean trap frequency of $\overline{\omega}/2\pi = 0.420(30)$ kHz, where the error bar is determined from the calibration uncertainty. As explained below, a more precise method based on minimizing the residual error from a theory comparison gives $\overline{\omega}/2\pi = 0.439(5)$ kHz, which is well within error bars of the calibration. We use the latter value for all fits shown in the main manuscript.

For deep lattices the on-site interaction energy U can be directly calculated from Wannier functions in the lowest band, as the energy gap to the first excited band is much larger than all other Hubbard energy scales. For the lattice depths used in this work of $7.7(5)\ E_{\mathrm{R}}$ ($7.2(4)\ E_{\mathrm{R}}$ for the data in figure 5.6), higher band contributions can play a role and change the value of the on-site interaction energy as compared to the simple lowest-band calculation, which gives $U_0/h = 6.79$ kHz for the standard

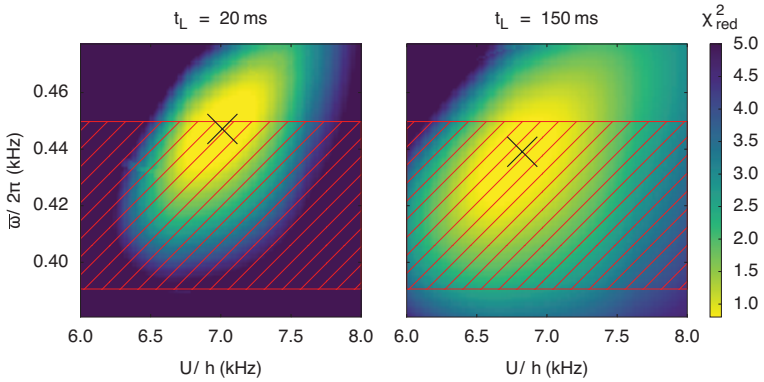

Figure 5.9: We show the reduced chi-squared value obtained from simultaneous fits to radial profiles of the density and spin correlator for different pair values of ν and U. We use data shown in figure 5.5 with two different lattice loading times that are expected to result in samples consistent with thermal equilibrium. Crosses mark the minimum and the red grid denotes the uncertainty region for the trap frequency calibration obtained from breathing oscillations. Using the data for the longest lattice loading time $t_{\mathrm{L}} = 150\,\mathrm{ms}$ we determine $\omega/2\pi = 0.439(5)\,\mathrm{kHz}$ and $U/h = 6.82(10)\,\mathrm{kHz}$.

parameters [152]. When comparing our data to theory we find the best agreement (i.e. the smallest χ^2_{red} values) for slightly different values of U and $\overline{\omega}$ as compared to the calculated and calibrated values. In figure 5.9 we show for different (fixed) values of U and $\overline{\omega}$ the χ^2_{red} obtained from a simultaneous fit to the measured density and spin correlator profiles of figure 5.5, with T and μ as free parameters (see previous section). For an equilibrated gas that can be accurately modeled with a local-density approximation, the exact location of the minimum in χ^2_{red} allows an accurate determination of U and $\overline{\omega}$ for sufficiently precise experimental data with small error bars. For the fits shown in the manuscript we use $U/h = 6.82(10)\,\mathrm{kHz}$ and $\omega/2\pi = 0.439(5)\,\mathrm{kHz}$, which are the parameters with minimal χ^2_{red} for the data with the longest lattice loading time of $\tau_{\mathrm{L}} = 150\,\mathrm{ms}$. We find similar values within 5% for the other lattice loading times $\tau_{\mathrm{L}} > 20\,\mathrm{ms}$.

6

Looking forward

This thesis has detailed a controlled, tunable, and well-understood platform for accessing Hubbard model physics with ultracold atoms. The technique of site-resolved imaging provides access to new observables for fermions in a lattice — site-resolved occupation statistics, as well as local spin and charge correlators. We can create a lattice of fermions both in the atomic limit of large repulsive interactions, where we see Mott and band insulators, and in a regime where the interaction energy becomes comparable to the bandwidth, giving rise to compressible states with magnetic correlations. In both of these regimes a comparison of our observables to available theory for the Hubbard model in thermal equilibrium yields excellent quantitative agreement. The lowest temperatures reported in Chapter 5, of $T/t < 0.45$, represent the current state of the art for fermions in optical lattices.

These initial experiments at relatively high temperatures were useful for benchmarking as theoretical

methods and numerical data were readily available for comparison. With a good understanding of the experiment — with independent calibrations of how the Hubbard parameters and harmonic confinement relate to experimental knobs of lattice powers and magnetic fields — we can now move forward into less well-explored regimes. Restricting the discussion to many-body physics, I can identify three broad paths for moving forward.

One possibility is to continue to study equilibrium physics of the Hubbard model — to try to map out phase diagrams in lower temperature regimes where computational methods become costly due to the sign problem [155]. In my opinion, it is unlikely that cold atom experiments in the near future will beat the state-of-the-art in temperature for Quantum Monte Carlo simulations. Gull et al. [36] are able to simulate temperatures of $T/t = 1/60$. This is more than a factor of twenty colder than the lowest temperatures that experiments with fermionic atoms can achieve at present. Furthermore, Gull et al. are able to access sufficiently large cluster sizes to convincingly report that the onset of superconductivity and the pseudogap at higher temperatures are not artifacts of small clusters. I do believe, however, that site-resolved imaging experiments can provide a complementary approach because they have straightforward access to real-space observables and correlations, and may also be able to explore parameters regimes with larger samples more efficiently than current numerical simulations. With the combination of a better understanding of heating mechanisms in optical lattices and the use of entropy redistribution schemes that I will describe below, it seems likely that in the next couple of years we will be able to achieve temperatures that are lower by a factor of a few. These lower temperatures may bring us to a regime where the antiferromagnetic correlation length is comparable to the sample size and also may provide access to pseudogap physics away from half-filling. For experiments to be useful as a comparison to numerical methods, we will need an independent way to measure the chemical potential and temperature. Fortunately, as pointed out in [48], the contour of half-filling ($\mu = U/2$) in a trap can be determined because this is where the density of singly-occupied sites is maximized. It may be possible to determine

the temperature by fitting the density in the low-density wings of the cloud to a non-interacting or weakly-interacting theory, but further exploration is necessary.

An area that remains almost completely unexplored by experiments with fermions in optical lattices is non-equilibrium dynamics. Site-resolved imaging experiments are especially well-suited for these studies because of the ability to detect correlations and to make local measurements in the trap. For the bosonic microscopes, these abilities enabled a host of experiments. The lattice could suddenly be quenched to a different depth and then the dynamics of correlations could be observed [65, 62]. Alternatively, atoms with a different spin could suddenly be introduced to the system by a local rf-transfer and the resulting spin-correlation dynamics could be studied [68, 67, 69, 70]. There are also a number of open questions regarding thermal equilibration in cold atom experiments, which are isolated from any thermal bath. Trapped atoms are constantly being heated by technical noise on optical traps, three-body collisions, etc. One might worry that if these heating rates are sufficiently large the trapped atoms may never be in thermal equilibrium. This would call into question theory comparisons for experiments measuring trap-averaged quantities and rely on an assumption of thermal equilibrium [44]. We could study this problem with our microscope by increasing the heating rate of the system and using the same χ^2 analysis presented in chapter 5 to evaluate quantitative comparisons with theory. We could also easily extend the studies of the optical lattice loading dynamics presented in chapter 5. We observed that the growth of magnetic correlations for longer lattice loading times was dominated by the effects of density redistribution in the trap. It would be interesting to see if, for larger interaction energies where superexchange dynamics are slower, the timescale of formation for magnetic correlations is set by superexchange processes. Finally, with the addition of some new hardware, we can also observe the propagation of holes in a Mott insulator. Combining temporally incoherent light in a single spatial mode with a digital mirror device in the image plane of our high-resolution imaging system will allow us to create arbitrary potentials on top of the lattice with single-site resolution. We could, for example,

apply a repulsive potential to a single lattice site, or an array of sites during lattice loading to raise the chemical potential, pinning holes to those sites. With a quench of the hole-pinning potential the holes could be released and the subsequent dynamics observed. This would be a realization of the recent proposal by Carlström, et al. [156]. Combining this with lower temperatures would also enable the observation of hole propagation within an antiferromagnetic state [157].

The third path forward is to explore many-body Hamiltonians other than the Hubbard Hamiltonian. An active area in cold atoms along these lines is the generation of artificial gauge fields and topological matter with cold atoms [158]. Many of the proposed techniques for generating artificial gauge fields require Raman coupling between internal states of the atom or spin-dependent optical potentials. ^{6}Li is poorly-suited to these techniques because the $2P$ electronic state has unresolved hyperfine structure and a small fine-structure splitting. In contrast, the large absolute energy scales arising from the light mass of ^{6}Li make it comparably well-suited to schemes that require adiabatically preparing a topological state, such as the trap-deformation and rotation scheme realized in [159]. Other approaches that are potentially suitable include Raman-assisted tunneling in an optical superlattice [160] and the generation of topological band structures by modulating a hexagonal lattice [53]. All of these approaches would require substantial changes to the way the lattice is generated in the current setup.

Entropy redistribution to achieve lower temperatures

Many future possibilities for the experiment require or would benefit from lower temperatures. Several methods have been proposed to lower the entropy in trapped atomic fermi gases by redistributing it to some other thermal reservoir. Ho, et al. [145] propose using a Bose-Einstein condensate as a thermal reservoir. This proposal would be difficult to implement in our single-species experiment, but may be practical in the ^{40}K experiments which utilize mixtures with ^{87}Rb to enhance the efficiency of evaporative cooling [80, 82]. Another proposal, by Bernier et al. [144], suggests shaping the

harmonic confinement in order to divide the system into entropy-rich and -poor regions, which could then be separated. Here I will describe two schemes, along the same lines could allow us to achieve longer-range antiferromagnetic correlations.

Both of these schemes rely on the same idea as the proposal by Bernier, et al. In idealized ultracold atom experiments, which are well isolated from any thermal environment, the total entropy of the cloud is fixed. Furthermore, systems are generally inhomogeneous due to an external trapping potential. If one can create a scenario where that inhomogeneity causes one region to take up most of the entropy, then another region will have comparatively low entropy, and may exhibit strong correlations under the correct circumstances. Take, for example, the Mott insulator surrounded by a metalic ring that was presented in chapter 4. The Mott insulating region has low charge entropy because most of the entropy in the system is contained in the metallic ring surrounding it which exhibits large charge fluctuations. This happens because the outer region, in the local density approximation, has a lower local chemical potential.

The first scheme I propose has a similar idea. We could use an attractive dimple potential to raise the chemical potential in the center of the cloud. As was described in chapter 5, in the compressible regime of the Hubbard model where the interaction energy and bandwidth are comparable, the largest spin correlations occur at half-filling. If the dimple were set up such that the chemical potential in the center of the cloud were tuned to half-filling, the outer regions at lower chemical potentials would take up most of the spin and charge entropy. At the moment, the gaussian waists of our lattice beams are too small to have a sufficiently flat outer region for this to work, but larger beams could easily be implemented.

Another scheme involves creating two planes of atoms in the 3D lattice which have different tunneling energies. In the plane where the tunneling energy is suppressed, the spin entropy will be large due to the correspondingly smaller superexchange energy scale. For fixed entropy, this will enhance spin-correlations in the plane with larger tunneling energy. Loading two coupled planes

at different tunneling energies should be possible with the composite vertical lattice described in section 1.3.3. The major experimental challenge will be to find a way to image only one of the two planes (potentially by removing the atoms in the plane with smaller tunneling) before imaging.

At the moment we are unable to estimate the enhancement in magnetic correlations that could be achieved in either of these proposals due to a lack of theory data. We are primarily interested in the interaction range $U/t = 8$ to $U/t = 16$ with temperatures of $T/t < 0.4$ and chemical potentials from half-filling to low densities. The published NLCE data [149] that is available for the 2D Hubbard model is noisy away from half-filling at these low temperatures, and the available DCA data [161] is too sparse in the parameter regime of interest. We are currently working with theorists to obtain numerical simulations for the parameters of interest to estimate the reduction in temperature that could be achieved with the above proposals.

A

^{6}Li Atomic Properties

A.1 Zeeman Shifts

To model optical and radio-frequency transitions, the force applied to an atom by a magnetic field gradient, and two-particle scattering it is important to calculate the spectrum and eigenstates of an atom in a magnetic field. In this appendix, I primarily wanted to provide a quick reference for the magnetic moments of the $2S_{1/2}$ electronic manifold, as this quantity comes up frequently in discussion.

The thesis of Michael Gehm [162] provides a clear discussion of how to compute the energy spectrum of ^{6}Li in the presence of a magnetic field, and I have followed that procedure to generate the plots in this section. Briefly, in the subspace of an electronic fine-structure manifold, one must

diagonalize the combined Zeeman and hyperfine interaction hamiltonians, $\hat{H}_B$ and $\hat{H}_{HF}$, respectively. The hyperfine Hamiltonian is given by:

$$\hat{H}_{HF} = -\hat{\boldsymbol{\mu}} \cdot \hat{\boldsymbol{B}}(\mathbf{0}) + \frac{1}{6} e \sum_{\alpha\beta} \hat{Q}_{\alpha\beta} \frac{\partial^2 \phi(0)}{\partial x_\alpha \partial x_\beta}, \tag{A.1}$$

where $\hat{\boldsymbol{\mu}}$ and $\hat{Q}$ are the nuclear magnetic dipole and quadrupole operators, respectively. The nucleus is located at $\boldsymbol{x} = 0$, e is the electron charge, $\hat{\boldsymbol{B}}$ is the magnetic field operator, and ϕ is the electric potential. The energy shifts from the hyperfine interaction are given by

$$\Delta E_{HF} = \frac{1}{2} AC + \frac{3}{8} B \frac{C(C+1)}{I(2I-1)J(2J-1)}, \tag{A.2}$$

where $C = F(F+1) - J(J+1) - I(I+1)$, with F, J, and I quantum numbers for the total atomic angular momentum, the total electronic angular momentum and the nuclear spin, respectively. A and B are the magnetic dipole hyperfine constant and the electric quadrupole hyperfine constant respectively, whose values for the $2S$ and $2P$ electronic states of ^{6}Li are given in table A.1.

The Zeeman interaction Hamiltonian is given by

$$\hat{H}_B = -\frac{\mu_B}{\hbar} \sum_x g_x \hat{\boldsymbol{X}}_z \cdot \hat{\boldsymbol{B}}, \tag{A.3}$$

where the sum is over good angular momentum quantum numbers, μ_B is the Bohr magneton, g_x and $\hat{\boldsymbol{X}}_z$ are the g-factor and angular momentum projection operator corresponding to the good quantum numbers. Using the completely uncoupled basis as an example, the Zeeman energy shift is

$$\Delta E_B = g_e \mu_B m_S + \mu_B m_L + \mu_N m_I, \tag{A.4}$$

where g_e is the electron g-factor, μ_N is the nuclear magneton, and m_S, m_L, and m_I are the electron

$A_{2S_{1/2}}$	152.1368407 MHz	[163]
$A_{2P_{1/2}}$	17.386 MHz	[164]
$A_{2P_{3/2}}$	−1.155 MHz	[163]
$B_{2P_{3/2}}$	0.1 MHz	[163]

Table A.1: The magnetic dipole (A) and electric quadrupole (B) hyperfine constants for the $2S$ and $2P$ states of ^{6}Li, taken from compilation in [162].

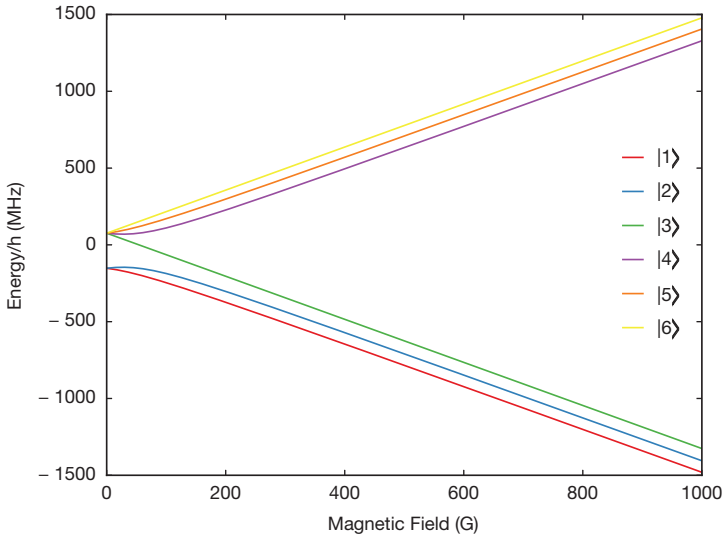

Figure A.1: Magnetic field dependence of the energy levels for the $2S_{1/2}$ ground electronic manifold.

spin, electron orbital angular momentum, and nuclear spin projections. To calculate the energy spectra, I use equations A.2 and A.4 to construct representations of the respective Hamiltonians, combine them after transforming them into the same basis, and diagonalize the combined Hamiltonian. The resulting energy spectrum for the $2S_{1/2}$ state is shown in figure A.1, with the derived field-dependent magnetic moments in figure A.2. When computing the spectrum for the $2P$ states for Zeeman splittings that approach the fine-structure splitting, one must combine the two fine-structure manifolds and add an additional term to the interaction Hamiltonian corresponding to the spin-orbit coupling.

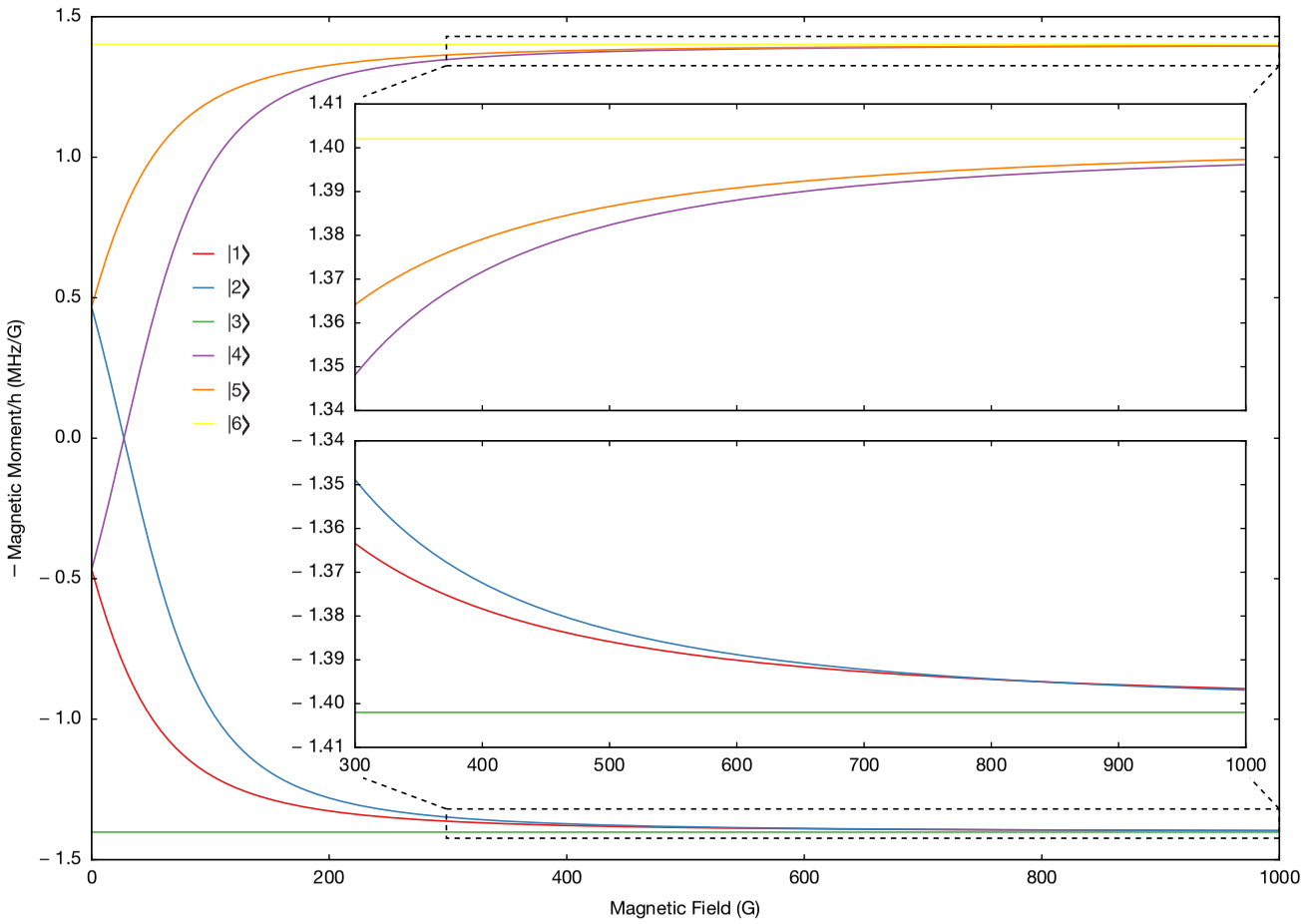

Figure A.2: Derivatives of the eigenstate energies with respect to magnetic field for the $2S_{1/2}$ ground electronic manifold.

A.2 Optical transitions

A.2.1 "Closed" optical transitions

Closed optical transitions are a useful feature of alkali atoms, as they allow many photons to be scattered without the need for extra repumping lasers. Cycling transitions are used in laser cooling, absorption and fluorescence imaging, and in our blowout scheme for spin-detection discussed in chapter 5. In the limit of large magnetic fields, where the Zeeman splitting is much larger than the hyperfine interaction and the nuclear spin is completely decoupled from the electronic angular momentum, ^{6}Li has closed optical transitions from every state in the $2S_{1/2}$ electronic manifold to the $2P_{3/2}$ manifold, as shown in figure A.3. However, at fields of several hundred Gauss, which are typical imaging fields for experiments using ^{6}Li, the residual hyperfine interaction mixes states in the $2S_{1/2}$ manifold and allows for multiple decay paths from the $2P_{3/2}$ manifold, meaning that the transitions depicted are not quite closed.

It is easy to see this effect using the analytic expressions for the eigenstates of the $2S_{1/2}$ manifold in the $|m_S, m_I\rangle$ basis, given in [162, 165]:

$$\begin{aligned}
|1\rangle &= \sin\theta_+|1/2, 0\rangle - \cos\theta_+|-1/2, 1\rangle \\
|2\rangle &= \sin\theta_-|1/2, -1\rangle - \cos\theta_-|-1/2, 0\rangle \\
|3\rangle &= |-1/2, -1\rangle \\
|4\rangle &= \cos\theta_-|1/2, -1\rangle + \sin\theta_-|-1/2, 0\rangle \\
|5\rangle &= \cos\theta_+|1/2, 0\rangle + \sin\theta_+|-1/2, 1\rangle \\
|6\rangle &= |1/2, 1\rangle,
\end{aligned} \tag{A.5}$$

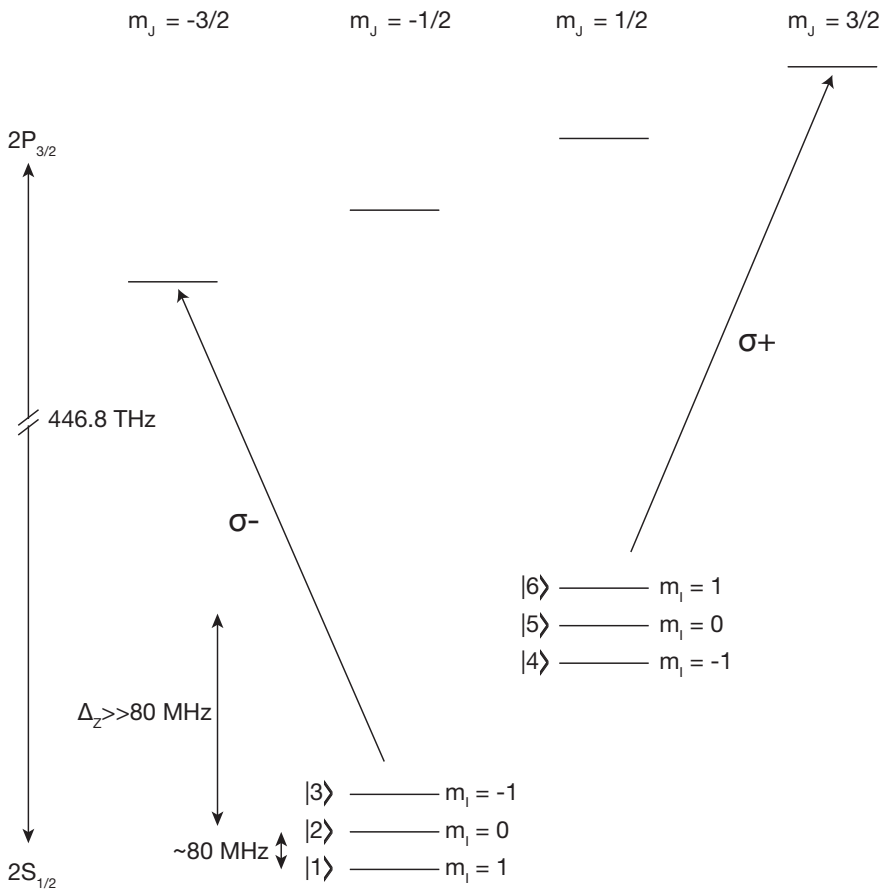

Figure A.3: Here I show an idealized picture of closed optical transitions in $^6\mathrm{Li}$ at magnetic fields sufficiently large that the Zeeman splitting in the ground electronic state, Δ_Z is significantly larger than the hyperfine splitting between states with different nuclear spin. In this regime, the so-called "Paschen-Back" limit, the nuclear spin, I, becomes completely decoupled from the total electronic angular momentum, J. Each m_J sublevel of the $2P_{3/2}$ state also contains three nuclear spin sublevels but the splitting between these states is $1\,\mathrm{MHz}$, much smaller than the excited state lifetime. In this Paschen-Back limit, the optical transitions shown above are completely closed. Because the light field does not interact with the nuclear spin, m_I is preserved for all optical transitions, and optical transitions from $|1\rangle, |2\rangle$, or $|3\rangle$ to the respective excited electronic state with $m_J = -3/2$ and matching nuclear spin as well as optical transitions from $|4\rangle, |5\rangle$, or $|6\rangle$ to the respective excited electronic state with $m_J = 3/2$ and matching nuclear spin shown above are completely closed. However, at the magnetic bias fields of several hundred Gauss where these transitions are typically driven in cold atom experiments, the nuclear spin is not completely decoupled, and these transitions are not quite closed.

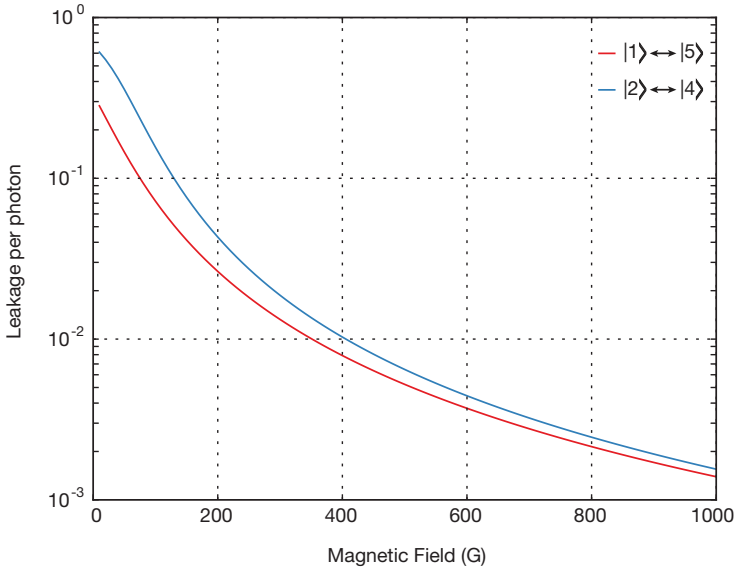

Figure A.4: Leakage out of the cycling transitions for each photon scattered at different magnetic fields. As discussed in the text, a cycling transition on $|1\rangle$ leaks into $|5\rangle$ and vice versa, and a cycling transition on $|2\rangle$ leaks into $|4\rangle$ and vice versa.

where ,

$$\begin{aligned} \sin\theta_{\pm} &= \frac{1}{\sqrt{1+\frac{1}{2}(Z^{\pm}+R^{\pm})^2}} \\ \cos\theta_{\pm} &= \sqrt{1-\sin\theta_{\pm}} \\ Z^{\pm} &= \frac{(\mu_n+2\mu_e)B}{A_{2S_{1/2}}} \pm \frac{1}{2} \\ R^{\pm} &= \sqrt{(Z^{\pm})^2+2}. \end{aligned} \quad . \tag{A.6}$$

Here, μ_n and μ_e are the nuclear and electron magnetic moments, and $A_{2S_{1/2}}$ is the magnetic dipole constant for the $2S_{1/2}$ electronic state given in table A.1. We note that the Paschen-Back limit, where the nuclear spin is completely decoupled from the electronic angular momentum, corresponds in the above equations to $B \to \infty$, $\cos\theta_{\pm} \to 1$, and $\sin\theta_{\pm} \to 0$.

To illustrate how the residual hyperfine coupling leads to decay back into multiple ground states

on a nearly closed transition, let's consider driving a "closed" optical transition for the $|1\rangle$ state, as shown in figure A.3. It is important to note that since the hyperfine splitting in the $2P_{3/2}$ manifold is small ($\sim$ 1 MHz), in the magnetic field range of several hundred Gauss that we are considering the $2P_{3/2}$ is well in the Paschen-Back regime and the eigenstates have only a single component in the $|m_J, m_I\rangle$ basis. The best we can do for closed transitions from $|1\rangle$, which is predominantly $|2S_{1/2}, -1/2, 1\rangle$ is to use $\sigma-$ polarized light to drive a transition to the $|2P_{3/2}, -3/2, 1\rangle$ state. In fact, even for light with mixed polarization, $|2P_{3/2}, -3/2, 1\rangle$ is the only state in the nearly-degenerate $|2P_{3/2}, m_J = -3/2\rangle$ nuclear spin multiplet that couples to $|1\rangle$. Now, consider the states that $|2P_{3/2}, -3/2, 1\rangle$ can decay to – any ground state with a $|-1/2, 1\rangle$ component – which includes both $|1\rangle$ and $|5\rangle$. The branching ratio for decay into $|5\rangle$ in this case will be given by $\sin^2\theta_+$. Repeating this set of arguments for each of the ground states we can see that driving the cycling transition for $|2\rangle$ leads to leakage into $|4\rangle$ with a branching ratio of $\sin^2\theta_-$, driving the cycling transition for $|4\rangle$ leads to leakage into $|2\rangle$ with a branching ratio of $\sin^2\theta_-$, driving the cycling transition for $|5\rangle$ leads to leakage into $|1\rangle$ with a branching ratio of $\sin^2\theta_+$, while the cycling transitions for $|3\rangle$ and $|6\rangle$ are truly closed. Figure A.4 shows values of $\sin^2\theta_\pm$ as a function of magnetic field.

A.2.2 Reduced matrix elements for optical transitions

D1-line reduced matrix element	$\langle J' = 1/2 \|\| \hat{\mu} \|\| J = 1/2\rangle$	1.148×10^{-29} C · m
D2-line reduced matrix element	$\langle J' = 3/2 \|\| \hat{\mu} \|\| J = 1/2\rangle$	3.977×10^{-29} C · m

Table A.2: Reduced matrix elements for optical transitions on the D1- and D2-lines [162].

B

Super-polished Substrate Coating Data

No.	Thickness (nm)	Material
1	118.306	SiO2
2	148.821	Nb2O5
3	207.216	SiO2
4	139.329	Nb2O5
5	213.045	SiO2
6	143.436	Nb2O5
7	226.057	SiO2
8	146.652	Nb2O5
9	223.506	SiO2
10	142.498	Nb2O5
11	219.253	SiO2
12	144.023	Nb2O5
13	223.665	SiO2
14	141.688	Nb2O5
15	213.147	SiO2
16	140.081	Nb2O5
17	221.323	SiO2
18	146.949	Nb2O5
19	227.642	SiO2
20	143.732	Nb2O5
21	222.387	SiO2
22	145.405	Nb2O5
23	218.924	SiO2
24	132.788	Nb2O5
25	193.771	SiO2

No.	Thickness (nm)	Material
26	120.602	Nb2O5
27	187.597	SiO2
28	115.753	Nb2O5
29	184.738	SiO2
30	114.788	Nb2O5
31	182.839	SiO2
32	114.693	Nb2O5
33	183.276	SiO2
34	115.699	Nb2O5
35	184.182	SiO2
36	120.47	Nb2O5
37	191.112	SiO2
38	132.553	Nb2O5
39	219.487	SiO2
40	139.328	Nb2O5
41	204.244	SiO2
42	123.182	Nb2O5
43	189.232	SiO2
44	118.009	Nb2O5
45	183.945	SiO2
46	118.073	Nb2O5
47	187.403	SiO2
48	112.64	Nb2O5
49	93.883	SiO2

Table B.1: Coating stack design for the super-polished substrate. The coating was manufactured by Advanced Thin Films using ion beam sputtering. The design incorporates the wavelength dependent indices of refraction of SiO2 and Nb2O5 as supplied by Advanced Thin Films. The layers are indexed such that layer 1 is the closest to the super-polished substrate, which is itself made of fused silica.

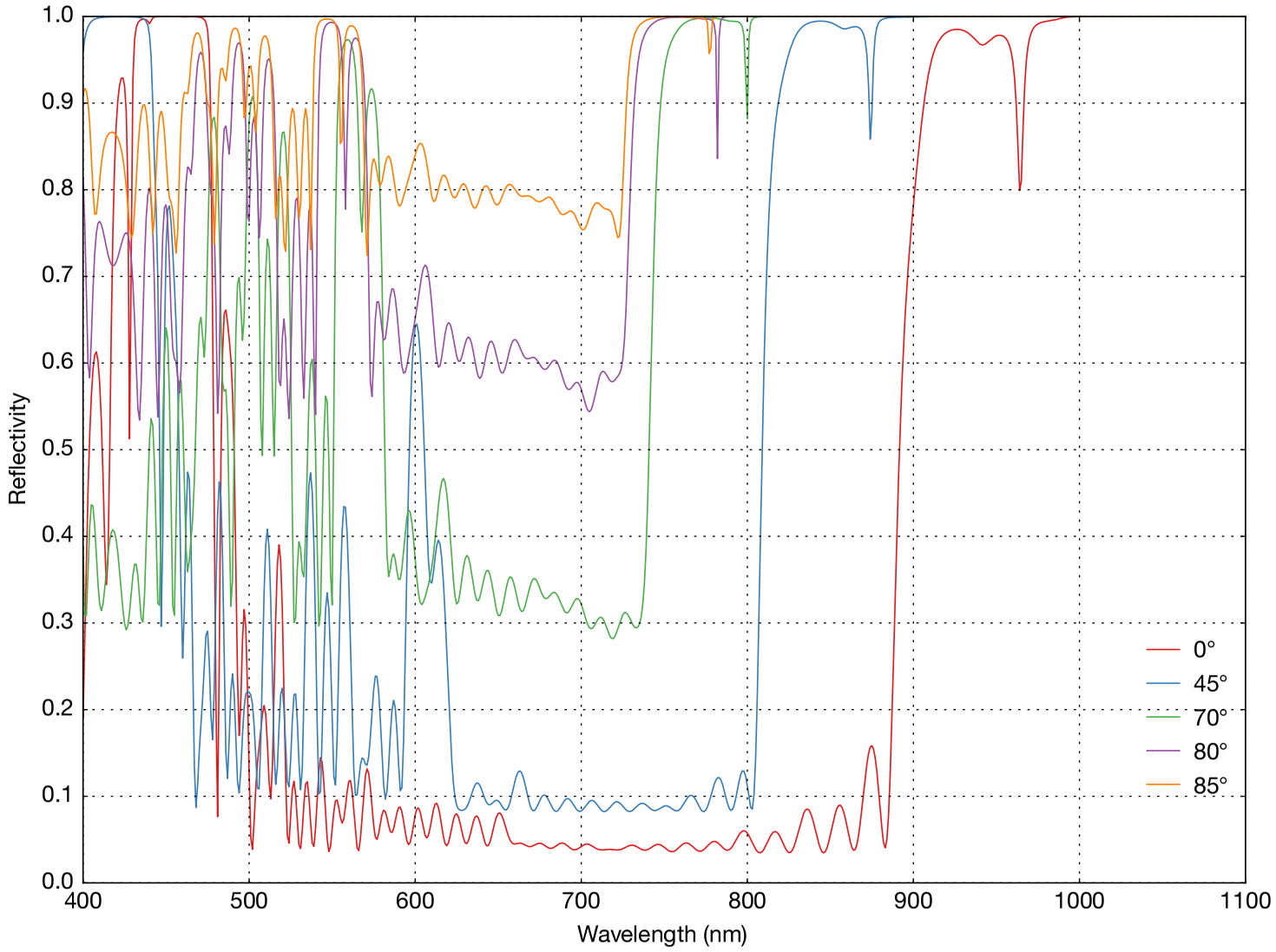

Figure B.1: Calculated super-polished substrate reflectivity for s-polarized light.

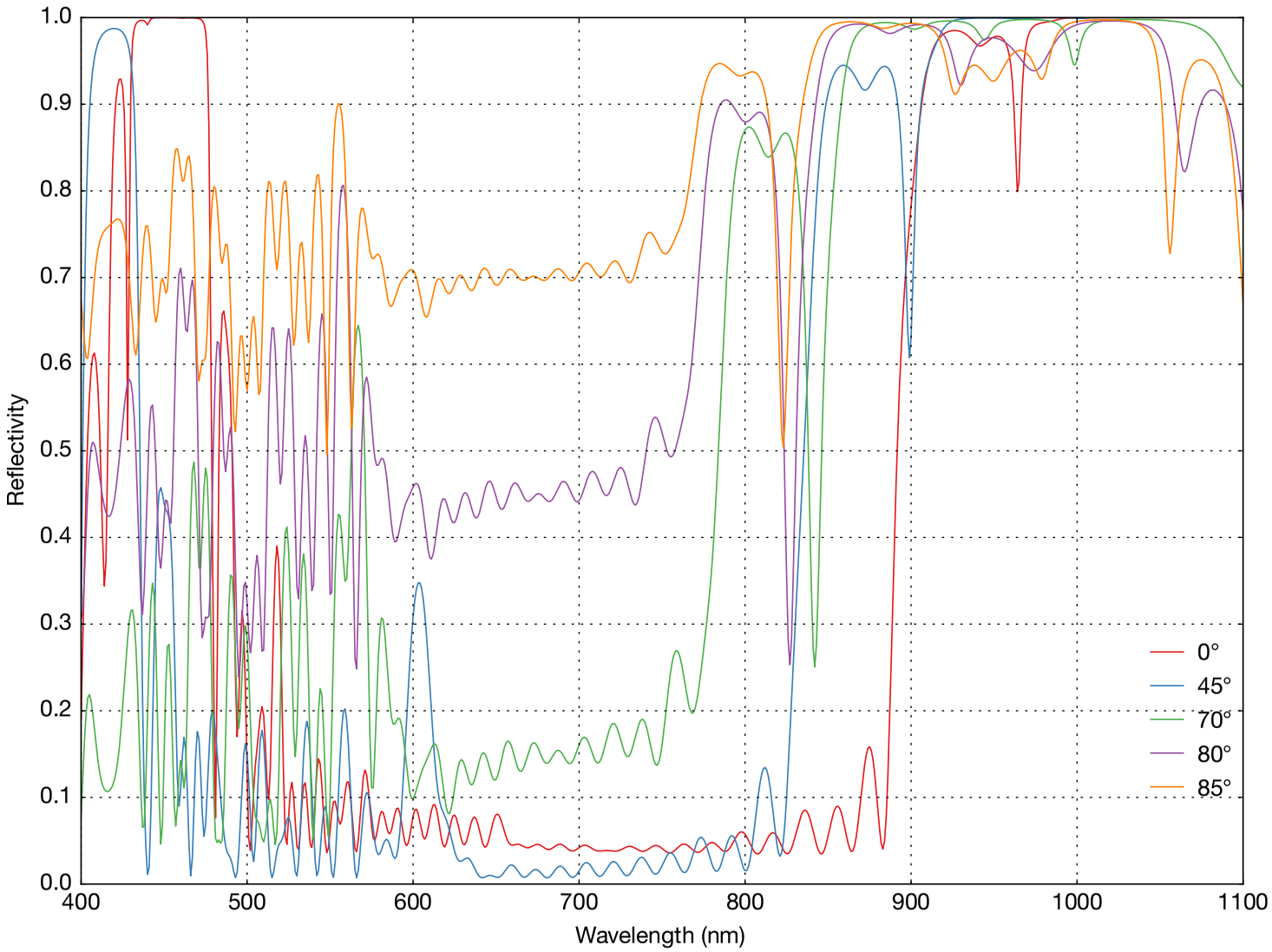

Figure B.2: Calculated super-polished substrate reflectivity for p-polarized light.

References

[1] Anderson, P. W. More is different. *Science* 177, 393–396 (1972).

[2] Dagotto, E. Complexity in strongly correlated electronic systems. *Science* 309, 257–262 (2005).

[3] Goldenfeld, N. Simple Lessons from Complexity. *Science* 284, 87–89 (1999).

[4] Sachdev, S. *Quantum Phase Transitions* (Cambridge University Press, 2011), 2nd edn.

[5] Bednorz, J. G. & Müller, K. A. Possible High T c Superconductivity in the Ba — La — Cu — O System. *Zeitschrift für Phys. B* 64, 189 (1986).

[6] Lee, P., Nagaosa, N. & Wen, X.-G. Doping a Mott insulator: Physics of high-temperature superconductivity. *Rev. Mod. Phys.* 78, 17–85 (2006).

[7] Dagotto, E. *Nanoscale Phase Separation and Colossal Magnetoresistance* (Springer-Verlag, 2003).

[8] Metcalf, H. J. & van der Straten, P. *Laser Cooling and Trapping*. Graduate Texts in Contemporary Physics (Springer New York, New York, NY, 1999).

[9] Hess, H. F. Evaporative cooling of magnetically trapped and compressed spin-polarized hydrogen. *Phys. Rev. B* 34, 3476–3479 (1986).

[10] Masuhara, N. *et al.* Evaporative cooling of spin-polarized atomic hydrogen. *Phys. Rev. Lett.* 61, 935–938 (1988).

[11] Davis, K. *et al.* Bose-Einstein Condensation in a Gas of Sodium Atoms. *Phys. Rev. Lett.* 75, 3969–3973 (1995).

[12] Anderson, M. H., Ensher, J. R., Matthews, M. R., Wieman, C. E. & Cornell, E. A. Observation of Bose-Einstein Condensation in a Dilute Atomic Vapor. *Science* 269, 198–201 (1995).

[13] Ketterle, W., Durfee, D. S. & Stamper-Kurn, D. M. Making, probing and understanding Bose-Einstein condensates. arXiv:9904034.

[14] Pitaevskii, L. & Stringari, S. *Bose-Einstein Condensation* (Clarendon Press, 2003).

[15] Pethick, C. J. & Smith, H. *Bose–Einstein Condensation in Dilute Gases* (Cambridge University Press, Cambridge, 2008).

[16] Jaksch, D., Bruder, C., Cirac, J. I., Gardiner, C. W. & Zoller, P. Cold Bosonic Atoms in Optical Lattices. *Phys. Rev. Lett.* 81, 3108–3111 (1998).

[17] Greiner, M., Mandel, O., Esslinger, T., Hänsch, T. W. & Bloch, I. Quantum phase transition from a superfluid to a Mott insulator in a gas of ultracold atoms. *Nature* 415, 39–44 (2002).

[18] DeMarco, B. Onset of Fermi Degeneracy in a Trapped Atomic Gas. *Science* 285, 1703–1706 (1999).

[19] Inouye, S. *et al.* Observation of Feshbach resonances in a Bose-Einstein condensate. *Nature* 392, 151–154 (1998).

[20] Courteille, P., Freeland, R. S., Heinzen, D. J., van Abeelen, F. A. & Verhaar, B. J. Observation of a Feshbach resonance in cold atom scattering. *Phys. Rev. Lett.* 81, 69–72 (1998).

[21] Loftus, T., Regal, C. A., Ticknor, C., Bohn, J. L. & Jin, D. S. Resonant Control of Elastic Collisions in an Optically Trapped Fermi Gas of Atoms. *Phys. Rev. Lett.* 88, 173201 (2002).

[22] Dieckmann, K. *et al.* Decay of an ultracold fermionic lithium gas near a Feshbach resonance. *Phys. Rev. Lett.* 89, 203201 (2002).

[23] Chin, C., Julienne, P. & Tiesinga, E. Feshbach resonances in ultracold gases. *Rev. Mod. Phys.* 82, 1225–1286 (2010).

[24] O'Hara, K. M., Hemmer, S. L., Gehm, M. E., Granade, S. R. & Thomas, J. E. Observation of a strongly interacting degenerate Fermi gas of atoms. *Science* 298, 2179–2182 (2002).

[25] Regal, C. A., Greiner, M. & Jin, D. S. Observation of resonance condensation of fermionic atom pairs. *Phys. Rev. Lett.* 92, 40403 (2004).

[26] Zwierlein, M. W. *et al.* Observation of Bose-Einstein condensation of molecules. *Phys. Rev. Lett.* 91, 250401 (2003).

[27] Zwierlein, M. W. *et al.* Condensation of pairs of fermionic atoms near a Feshbach resonance. *Phys. Rev. Lett.* 92, 120403–1 (2004).

[28] Bartenstein, M. *et al.* Collective Excitations of a Degenerate Gas at the BEC-BCS Crossover. *Phys. Rev. Lett.* 92, 203201 (2004).

[29] Greiner, M., Regal, C. a. & Jin, D. S. Emergence of a molecular Bose–Einstein condensate from a Fermi gas. *Nature* 426, 537–540 (2003).

[30] Bourdel, T. *et al.* Experimental Study of the BEC-BCS Crossover Region in Lithium 6. *Phys. Rev. Lett.* 93, 050401 (2004).

[31] Giorgini, S., Pitaevskii, L. P. & Stringari, S. Theory of ultracold atomic Fermi gases. *Rev. Mod. Phys.* 80, 1215–1274 (2008).

[32] Ketterle, W. & Zwierlein, M. W. Making, probing and understanding ultracold Fermi gases. arXiv:0801.2500.

[33] Esslinger, T. Fermi-Hubbard Physics with Atoms in an Optical Lattice. *Annu. Rev. Condens. Matter Phys.* 1, 129–152 (2010).

[34] Hubbard, J. Electron Correlations in Narrow Energy Bands. *Proc. R. Soc. A Math. Phys. Eng. Sci.* 276, 238–257 (1963).

[35] Maier, T. a., Jarrell, M., Schulthess, T. C., Kent, P. R. C. & White, J. B. Systematic Study of d -Wave Superconductivity in the 2D Repulsive Hubbard Model. *Phys. Rev. Lett.* 95, 237001 (2005).

[36] Gull, E., Parcollet, O. & Millis, A. J. Superconductivity and the pseudogap in the two-dimensional hubbard model. *Phys. Rev. Lett.* 110, 1–5 (2013).

[37] Rom, T. *et al.* Free fermion antibunching in a degenerate atomic Fermi gas released from an optical lattice. *Nature* 444, 733–736 (2006).

[38] Jördens, R., Strohmaier, N., Günter, K., Moritz, H. & Esslinger, T. A Mott insulator of fermionic atoms in an optical lattice. *Nature* 455, 204–207 (2008).

[39] Schneider, U. *et al.* Metallic and insulating phases of repulsively interacting fermions in a 3D optical lattice. *Science* 322, 1520–5 (2008).

[40] Duarte, P. M. *et al.* Compressibility of a Fermionic Mott Insulator of Ultracold Atoms. *Phys. Rev. Lett.* 114, 1–5 (2015).

[41] Greif, D., Tarruell, L., Uehlinger, T., Jördens, R. & Esslinger, T. Probing nearest-neighbor correlations of ultracold fermions in an optical lattice 1–5 (2010).

[42] Strohmaier, N. *et al.* Observation of Elastic Doublon Decay in the Fermi-Hubbard Model. *Phys. Rev. Lett.* 104, 1–4 (2010).

[43] Greif, D., Uehlinger, T., Jotzu, G., Tarruell, L. & Esslinger, T. Short-range quantum magnetism of ultracold fermions in an optical lattice. *Science* 340, 1307–1310 (2013).

[44] Hart, R. A. *et al.* Observation of antiferromagnetic correlations in the Hubbard model with ultracold atoms. *Nature* 519, 211–214 (2015).

[45] Greif, D., Jotzu, G., Messer, M., Desbuquois, R. & Esslinger, T. Formation and Dynamics of Antiferromagnetic Correlations in Tunable Optical Lattices. *Phys. Rev. Lett.* 115, 260401 (2015).

[46] Taie, S., Yamazaki, R., Sugawa, S. & Takahashi, Y. An SU(6) Mott insulator of an atomic Fermi gas realized by large-spin Pomeranchuk cooling. *Nat. Phys.* 8, 825–830 (2012).

[47] Hofrichter, C. *et al.* Direct probing of the Mott crossover in the SU(N) Fermi-Hubbard model. arXiv:1511.07287.

[48] Cocchi, E. *et al.* Equation of state of the two-dimensional hubbard model. *Phys. Rev. Lett.* 116, 175301 (2016).

[49] Greif, D. G. *Quantum magnetism with ultracold fermions in an optical lattice*. Ph.D. thesis, ETH Zurich (2013).

[50] Tarruell, L., Greif, D., Uehlinger, T., Jotzu, G. & Esslinger, T. Creating, moving and merging Dirac points with a Fermi gas in a tunable honeycomb lattice. *Nature* 483, 302–305 (2012).

[51] Uehlinger, T. *et al.* Artificial Graphene with Tunable Interactions. *Phys. Rev. Lett.* 111, 185307 (2013).

[52] Messer, M. *et al.* Exploring Competing Density Order in the Ionic Hubbard Model with Ultracold Fermions. *Phys. Rev. Lett.* 115, 115303 (2015).

[53] Jotzu, G. *et al.* Experimental realization of the topological Haldane model with ultracold fermions. *Nature* 515, 237–240 (2014).

[54] Hackermüller, L. *et al.* Anomalous expansion of attractively interacting fermionic atoms in an optical lattice. *Science* 327, 1621–4 (2010).

[55] Schneider, U. *et al.* Fermionic transport and out-of-equilibrium dynamics in a homogeneous Hubbard model with ultracold atoms. *Nat. Phys.* 8, 213–218 (2012).

[56] Nelson, K. D., Li, X. & Weiss, D. S. Imaging single atoms in a three-dimensional array. *Nat. Phys.* 3, 556–560 (2007).

[57] Gemelke, N., Zhang, X., Hung, C.-L. & Chin, C. In situ observation of incompressible Mott-insulating domains in ultracold atomic gases. *Nature* 460, 995–998 (2009).

[58] Bakr, W. S., Gillen, J. I., Peng, A., Fölling, S. & Greiner, M. A quantum gas microscope for detecting single atoms in a Hubbard-regime optical lattice. *Nature* 462, 74–77 (2009).

[59] Sherson, J. F. *et al.* Single-atom-resolved fluorescence imaging of an atomic Mott insulator. *Nature* 467, 68–72 (2010).

[60] Miranda, M., Inoue, R., Okuyama, Y., Nakamoto, A. & Kozuma, M. Site-resolved imaging of ytterbium atoms in a two-dimensional optical lattice. *Phys. Rev. A* 91, 063414 (2015).

[61] Bakr, W. S. *et al.* Probing the Superfluid to Mott Insulator Transition at the Single Atom Level. *Science* 329, 547–550 (2010).

[62] Endres, M. *et al.* Single-site- and single-atom-resolved measurement of correlation functions. *Appl. Phys. B* 113, 27–39 (2013).

[63] Simon, J. *et al.* Quantum simulation of antiferromagnetic spin chains in an optical lattice. *Nature* 472, 307–312 (2011).

[64] Bakr, W. S. *et al.* Orbital excitation blockade and algorithmic cooling in quantum gases. *Nature* 480, 500–503 (2011).

[65] Cheneau, M. *et al.* Light-cone-like spreading of correlations in a quantum many-body system. *Nature* 481, 484–487 (2012).

[66] Endres, M. *et al.* The 'Higgs' amplitude mode at the two-dimensional superfluid/Mott insulator transition. *Nature* 487, 454–458 (2012).

[67] Fukuhara, T. *et al.* Quantum dynamics of a mobile spin impurity. *Nat. Phys.* 9, 235–241 (2013).

[68] Fukuhara, T. *et al.* Microscopic observation of magnon bound states and their dynamics. *Nature* 502, 76–79 (2013).

[69] Hild, S. *et al.* Far-from-Equilibrium Spin Transport in Heisenberg Quantum Magnets. *Phys. Rev. Lett.* 113, 147205 (2014).

[70] Fukuhara, T. *et al.* Spatially Resolved Detection of a Spin-Entanglement Wave in a Bose-Hubbard Chain. *Phys. Rev. Lett.* 115, 035302 (2015).

[71] Schauß, P. *et al.* Observation of spatially ordered structures in a two-dimensional Rydberg gas. *Nature* 491, 87–91 (2012).

[72] Schauss, P. *et al.* Crystallization in Ising quantum magnets. *Science* 347, 1455–1458 (2015).

[73] Zeiher, J. *et al.* Microscopic characterization of scalable coherent rydberg superatoms. *Phys. Rev. X* 5, 1–8 (2015).

[74] Choi, J.-y. *et al.* Exploring the many-body localization transition in two dimensions. arXiv:1604.04178.

[75] Zupancic, P. P. J. *Dynamic Holography and Beamshaping using Digital Micromirror Devices*. Master's thesis, Ludwig-Maximilians-Universitat Munich (2013).

[76] Preiss, P. M. *et al.* Strongly correlated quantum walks in optical lattices. *Science* 347, 1229–1233 (2015).

[77] Islam, R. *et al.* Measuring entanglement entropy in a quantum many-body system. *Nature* 528, 77–83 (2015).

[78] Kaufman, A. M. *et al.* Quantum thermalization through entanglement in an isolated many-body system. arXiv:1603.04409.

[79] Haller, E. *et al.* Single-atom imaging of fermions in a quantum-gas microscope. *Nat. Phys.* 11, 738–742 (2015).

[80] Cheuk, L. W. *et al.* Quantum-Gas Microscope for Fermionic Atoms. *Phys. Rev. Lett.* 114, 193001 (2015).

[81] Parsons, M. F. *et al.* Site-Resolved Imaging of Fermionic ^{6}Li in an Optical Lattice. *Phys. Rev. Lett.* 114, 213002 (2015).

[82] Edge, G. J. A. *et al.* Imaging and addressing of individual fermionic atoms in an optical lattice. *Phys. Rev. A* 92, 063406 (2015).

[83] Omran, A. *et al.* Microscopic Observation of Pauli Blocking in Degenerate Fermionic Lattice Gases. *Phys. Rev. Lett.* 115, 263001 (2015).

[84] Huber, F. G. *Site-Resolved Imaging with the Fermi Gas Microscope*. Ph.D. thesis, Harvard University (2014).

[85] Greif, D. *et al.* Site-resolved imaging of a fermionic Mott insulator. *Science* 351, 953–957 (2016).

[86] Setiawan, W. *Fermi Gas Microscope*. Ph.D. thesis, Harvard University (2012).

[87] Strecker, K. E., Partridge, G. B. & Hulet, R. G. Conversion of an atomic Fermi gas to a long-lived molecular Bose gas. *Phys. Rev. Lett.* 91, 080406 (2003).

[88] Grimm, R., Weidemüller, M. & Ovchinnikov, Y. B. Optical dipole traps for neutral atoms. *At. Mol. Opt.* 39 (1999).

[89] Ketterle, W. & Pritchard, D. E. Trapping and focusing ground state atoms with static fields. *Appl. Phys. B Photophysics Laser Chem.* 54, 403–406 (1992).

[90] Gaunt, A. L., Schmidutz, T. F., Gotlibovych, I., Smith, R. P. & Hadzibabic, Z. Bose-Einstein Condensation of Atoms in a Uniform Potential. *Phys. Rev. Lett.* 110, 200406 (2013).

[91] Ramanathan, A. *et al.* Superflow in a Toroidal Bose-Einstein Condensate: An Atom Circuit with a Tunable Weak Link. *Phys. Rev. Lett.* 106, 130401 (2011).

[92] Brantut, J.-P., Meineke, J., Stadler, D., Krinner, S. & Esslinger, T. Conduction of ultracold fermions through a mesoscopic channel. *Science* 337, 1069–71 (2012).

[93] Husmann, D. *et al.* Connecting strongly correlated superfluids by a quantum point contact. *Science* 350, 1498–1501 (2015).

[94] Gillen, J. *The Quantum Gas Microscope*. Ph.D. thesis, Harvard University (2009).

[95] Ma, R. *Engineered potentials and dynamics of ultracold quantum gases under the microscope*. Ph.D. thesis, Harvard (2014).

[96] Blatt, S. *et al.* Low-noise optical lattices for ultracold Lithium-6. *Phys. Rev. A* 92, 021402 (2015).

[97] Stan, C. A. & Ketterle, W. Multiple species atom source for laser-cooling experiments. *Rev. Sci. Instrum.* 76, 24–29 (2005).

[98] Landau, L. & Lifshitz, E. *Quantum Mechanics (Non-Relativistic Theory)* (Elsevier Science Ltd., 1977).

[99] Georges, A. Condensed Matter Physics With Light And Atoms: Strongly Correlated Cold Fermions in Optical Lattices. arXiv:0702122.

[100] Moerdijk, a. J., Verhaar, B. J. & Axelsson, A. Resonances in ultracold collisions of ^{6}Li. *Phys. Rev. A* 51, 4852–4861 (1995).

[101] Petrov, D. S., Salomon, C. & Shlyapnikov, G. V. Weakly Bound Dimers of Fermionic Atoms. *Phys. Rev. Lett.* 93, 090404 (2004).

[102] Jochim, S. *et al.* Bose-Einstein condensation of molecules. *Science* 302, 2101–3 (2003).

[103] Zürn, G. *et al.* Precise Characterization of ^{6}Li Feshbach Resonances Using Trap-Sideband-Resolved RF Spectroscopy of Weakly Bound Molecules. *Phys. Rev. Lett.* 110, 135301 (2013).

[104] http://ultracold.physi.uni-heidelberg.de/files/scatteringlengths.txt (accessed March 25, 2015).

[105] Zhang, J. *et al.* P-wave Feshbach resonances of ultracold ^{6}Li. *Phys. Rev. A* 70, 030702 (2004).

[106] Schunck, C. H. *et al.* Feshbach resonances in fermionic ^{6}Li. *Phys. Rev. A* 71, 045601 (2005).

[107] Jördens, R. *Metallic and Mott-insulating phases in fermionic quantum gases*. Ph.D. thesis, ETH Zürich (2010).

[108] Strohmaier, N. *Exploring the Hubbard model with ultracold fermionic atoms in an optical lattice*. Ph.D. thesis, ETH Zürich (2010).

[109] Schneider, U. *Interacting Fermionic Atoms in Optical Lattices—A Quantum Simulator for Condensed Matter Physics*. Ph.D. thesis, Johannes Gutenberg-Universität Mainz (2010).

[110] Will, S. *Interacting bosons and fermions in three-dimensional optical lattice potentials: From atom optics to quantum simulation*. Ph.D. thesis, Johannes Gutenberg-Universität Mainz (2011).

[111] Ashcroft, N. W. & Mermin, N. D. *Solid State Physics* (Saunders, 1976).

[112] Greiner, M. *Ultracold quantum gases in three-dimensional optical lattice potentials*. Ph.D. thesis, Ludwig-Maximilians-Universität München (2003).

[113] Wannier, G. H. The Structure of Electronic Excitation Levels in Insulating Crystals. *Phys. Rev.* 52, 191–197 (1937).

[114] Slater, J. C. A Soluble Problem in Energy Bands. *Phys. Rev.* 87, 807–835 (1952).

[115] Preiss, P. M. *Atomic Bose-Hubbard Systems with Single-Particle Control*. Ph.D. thesis, Harvard University (2015).

[116] Oitmaa, J., Hamer, C. & Zhen, W. *Series expansion methods for strongly interacting lattice models* (Cambridge University Press, 2006).

[117] Ten Haaf, D. F. B. & Van Leeuwen, J. M. J. High-temperature series expansions for the Hubbard model. *Phys. Rev. B* 46, 6313–6327 (1992).

[118] Henderson, J., Oitmaa, J. & Ashley, M. High-temperature expansion for the single-band Hubbard model. *Phys. Rev. B* 46, 6328–6337 (1992).

[119] Wessel, S., Alet, F., Troyer, M. & Batrouni, G. G. Quantum Monte Carlo simulations of confined bosonic atoms in optical lattices. *Phys. Rev. A* 70, 053615 (2004).

[120] Pollet, L., Prokof'ev, N. V. & Svistunov, B. V. Criticality in Trapped Atomic Systems. *Phys. Rev. Lett.* 104, 245705 (2010).

[121] Helmes, R. W., Costi, T. A. & Rosch, A. Mott Transition of Fermionic Atoms in a Three-Dimensional Optical Trap. *Phys. Rev. Lett.* 100, 056403 (2008).

[122] Duarte, P. M. *et al.* All-optical production of a lithium quantum gas using narrow-line laser cooling. *Phys. Rev. A* 84, 061406(R) (2011).

[123] Hamilton, P. *et al.* Sisyphus cooling of lithium. *Phys. Rev. A* 89, 023409 (2014).

[124] Burchianti, A. *et al.* Efficient all-optical production of large Li6 quantum gases using D1 gray-molasses cooling. *Phys. Rev. A* 90, 043408 (2014).

[125] Hamann, S. E. *et al.* Resolved-Sideband Raman Cooling to the Ground State of an Optical Lattice. *Phys. Rev. Lett.* 80, 4149–4152 (1998).

[126] Kerman, A. J., Vuletic, V., Chin, C. & Chu, S. Beyond optical molasses: 3D raman sideband cooling of atomic cesium to high phase-space density. *Phys. Rev. Lett.* 84, 439–42 (2000).

[127] Thompson, J. D., Tiecke, T. G., Zibrov, A. S., Vuletić, V. & Lukin, M. D. Coherence and Raman Sideband Cooling of a Single Atom in an Optical Tweezer. *Phys. Rev. Lett.* 110, 133001 (2013).

[128] Kaufman, A. M., Lester, B. J. & Regal, C. A. Cooling a Single Atom in an Optical Tweezer to Its Quantum Ground State. *Phys. Rev. X* 2, 041014 (2012).

[129] Monroe, C. *et al.* Resolved-Sideband Raman Cooling of a Bound Atom to the 3D Zero-Point Energy. *Phys. Rev. Lett.* 75, 4011–4014 (1995).

[130] Lester, B. J., Kaufman, A. M. & Regal, C. A. Raman cooling imaging: Detecting single atoms near their ground state of motion. *Phys. Rev. A* 90, 011804(R) (2014).

[131] Patil, Y. S., Aycock, L. M., Chakram, S. & Vengalattore, M. Nondestructive imaging of an ultracold lattice gas. *Phys. Rev. A* 90, 033422 (2014).

[132] Bateman, J., Xuereb, A. & Freegarde, T. Stimulated Raman transitions via multiple atomic levels. *Phys. Rev. A* 81, 043808 (2010).

[133] Sakurai, J. J. *Modern Quantum Mechanics (Revised Edition)* (Addison-Wesley Publishing Company, Inc., 1994).

[134] Bransden, B. & Joachain, C. *Physics of Atoms and Molecules* (Pearson Education Limited, 2003).

[135] Meekhof, D. M., Monroe, C., King, B. E., Itano, W. M. & Wineland, D. J. Generation of Nonclassical Motional States of a Trapped Atom. *Phys. Rev. Lett.* 76, 1796–1799 (1996).

[136] Safronova, M. S., Safronova, U. I. & Clark, C. W. Magic wavelengths for optical cooling and trapping of lithium. *Phys. Rev. A* 86, 042505 (2012).

[137] van der Walt, S. *et al.* scikit-image: image processing in Python. *PeerJ* 2, e453 (2014).

[138] Weitenberg, C. *Single-Atom resolved imaging and manipulation of an atomic Mott insulator*. Ph.D. thesis, Ludwig-Maximilians-Universitaet (2011).

[139] Campbell, G. K. *et al.* Imaging the Mott insulator shells by using atomic clock shifts. *Science* 313, 649–652 (2006).

[140] Fölling, S., Widera, A., Müller, T., Gerbier, F. & Bloch, I. Formation of spatial shell structure in the superfluid to mott insulator transition. *Phys. Rev. Lett.* 97, 1–4 (2006).

[141] Bloch, I., Dalibard, J. & Zwerger, W. Many-body physics with ultracold gases. *Rev. Mod. Phys.* 80, 885–964 (2008).

[142] Endres, M. *et al.* Observation of correlated particle-hole pairs and string order in low-dimensional Mott insulators. *Science* 334, 200–203 (2011).

[143] Scarola, V. W., Pollet, L., Oitmaa, J. & Troyer, M. Discerning Incompressible and Compressible Phases of Cold Atoms in Optical Lattices. *Phys. Rev. Lett.* 102, 135302 (2009).

[144] Bernier, J.-S. *et al.* Cooling fermionic atoms in optical lattices by shaping the confinement. *Phys. Rev. A* 79, 061601(R) (2009).

[145] Ho, T.-L. & Zhou, Q. Squeezing out the entropy of fermions in optical lattices. *Proc. Natl. Acad. Sci.* 106, 6916–6920 (2009).

[146] Lubasch, M., Murg, V., Schneider, U., Cirac, J. I. & Bañuls, M. C. Adiabatic preparation of a Heisenberg antiferromagnet using an optical superlattice. *Phys. Rev. Lett.* 107, 165301 (2011).

[147] Anderson, P. W. The Resonating Valence Bond State in La2CuO4 and Superconductivity. *Science* 235, 1196–8 (1987).

[148] Mermin, N. D. & Wagner, H. Absence of Ferromagnetism or Antiferromagnetism in One- or Two-Dimensional Isotropic Heisenberg Models. *Phys. Rev. Lett.* 17, 1133–1136 (1966).

[149] Khatami, E. & Rigol, M. Thermodynamics of strongly interacting fermions in two-dimensional optical lattices. *Phys. Rev. A* 84, 053611 (2011).

[150] Chiesa, S., Varney, C. N., Rigol, M. & Scalettar, R. T. Magnetism and Pairing of Two-Dimensional Trapped Fermions. *Phys. Rev. Lett.* 106, 035301 (2011).

[151] Paiva, T., Scalettar, R., Randeria, M. & Trivedi, N. Fermions in 2D Optical Lattices: Temperature and Entropy Scales for Observing Antiferromagnetism and Superfluidity. *Phys. Rev. Lett.* 104, 066406 (2010).

[152] Büchler, H. P. Microscopic Derivation of Hubbard Parameters for Cold Atomic Gases. *Phys. Rev. Lett.* 104, 090402 (2010).

[153] Zupancic, P. *et al.* Ultra-precise holographic beam shaping for microscopic quantum control. arXiv:1604.07653.

[154] Eisert, J., Friesdorf, M. & Gogolin, C. Quantum many-body systems out of equilibrium. *Nat. Phys.* 11, 124–130 (2015).

[155] Troyer, M. & Wiese, U.-J. Computational complexity and fundamental limitations to fermionic quantum Monte Carlo simulations. *Phys. Rev. Lett.* 94, 170201 (2005).

[156] Carlström, J., Prokof'ev, N. & Svistunov, B. Quantum Walk in Degenerate Spin Environments. arXiv:1602.05366.

[157] Sensarma, R., Pekker, D., Lukin, M. D. & Demler, E. Modulation Spectroscopy and Dynamics of Double Occupancies in a Fermionic Mott Insulator. *Phys. Rev. Lett.* 103, 035303 (2009).

[158] Dalibard, J., Gerbier, F., Juzeliūnas, G. & Öhberg, P. Colloquium: Artificial gauge potentials for neutral atoms. *Rev. Mod. Phys.* 83, 1523–1543 (2011).

[159] Gemelke, N., Sarajlic, E. & Chu, S. Rotating Few-body Atomic Systems in the Fractional Quantum Hall Regime. arXiv:1007.2677.

[160] Aidelsburger, M. *et al.* Experimental Realization of Strong Effective Magnetic Fields in an Optical Lattice. *Phys. Rev. Lett.* 107, 1–5 (2011).

[161] LeBlanc, J. P. F. & Gull, E. Equation of state of the fermionic two-dimensional Hubbard model. *Phys. Rev. B* 88, 155108 (2013).

[162] Gehm, M. E. *Preparation of an Optically-Trapped Degenerate Fermi Gas of ˆ{6}Li: Finding the Route to Degeneracy*. Ph.D. thesis, Duke University (2003).

[163] Arimondo, E., Inguscio, M. & Violino, P. Experimental determinations of the hyperfine structure in the alkali atoms. *Rev. Mod. Phys.* 49, 31–75 (1977).

[164] Walls, J., Ashby, R., Clarke, J., Lu, B. & van Wijngaarden, W. Measurement of isotope shifts, fine and hyperfine structure splittings of the lithium D lines. *Eur. Phys. J. D* 22, 159–162 (2003).

[165] Houbiers, M., Stoof, H. T. C., McAlexander, W. I. & Hulet, R. G. Elastic and inelastic collisions of ^{6}Li atoms in magnetic and optical traps. *Phys. Rev. A* 57, R1497–R1500 (1998).